

PATIENT SPECIFIC PIXEL-BASED WEIGHTING FACTOR DUAL-ENERGY  
X-RAY IMAGING SYSTEM

By

Michael C. Reno

Submitted in partial fulfilment of the requirements  
for the degree of Master of Science

At

Dalhousie University  
Halifax, Nova Scotia  
August 2018

## **Dedication Page**

I dedicate this thesis to all of the wonderful people who have encouraged and assisted me in the completion of this work, but most importantly my parents Jane and Chris. You both assured me that I was capable of finishing this work and supported me 100% of the way through these last two years. I would also like to extend my dedication to my dog Roxy for always putting me in an uplifted mood.

## Table of Contents

|   |            |
|---|------------|
| <b>List of Tables</b> .....   | <b>vi</b>  |
| <b>List of Figures</b> .....  | <b>vii</b> |
| <b>Abstract</b> .....   | <b>x</b>   |
| <b>List of Abbreviations Used</b> .....                             | <b>xi</b>  |
| <b>Acknowledgements</b> .....                                       | <b>xii</b> |
| <b>Chapter 1: Introduction</b> .....                                | <b>1</b>   |
| 1.1: X-ray Imaging System .....                                     | 2          |
| 1.1.1: X-ray Tube .....   | 2          |
| 1.1.2: Bremsstrahlung Radiation .....                               | 4          |
| 1.1.3: Simulation of Spectra .....                                  | 4          |
| 1.1.4: Half Value Layer .....                                       | 8          |
| 1.1.5: X-ray Detector .....   | 10         |
| 1.2: X-ray Interactions with Matter .....                           | 12         |
| 1.3: Components of Image Quality .....                              | 15         |
| 1.3.1: Noise.....   | 15         |
| 1.3.2: Contrast .....   | 16         |
| 1.3.3: Scattered Radiation.....                                     | 17         |
| 1.3.4: Detective Quantum Efficiency Vs. Absorption Efficiency ..... | 18         |
| 1.3.5: Detector Modelling.....                                      | 19         |
| 1.3.6: Flat Field Correction Algorithm.....                         | 23         |
| 1.4: Dual-energy X-ray Imaging .....                                | 25         |
| 1.4.1: Simple Logarithmic Subtraction .....                         | 26         |
| 1.4.2: Decomposition of Basis Materials .....                       | 27         |
| 1.4.3: Single Exposure DE .....                                     | 29         |
| 1.4.4: Double Exposure DE.....                                      | 31         |
| 1.4.5: Single Source DE .....                                       | 31         |
| 1.4.6: Dual Source DE.....  | 32         |
| 1.4.7: Noise Reduction Algorithms .....                             | 34         |
| 1.5: Radiotherapy .....   | 37         |
| 1.5.1: Digitally Reconstructed Radiograph .....                     | 38         |
| 1.6: Applications of Dual-energy Imaging in Radiotherapy .....      | 42         |
| 1.7: Thesis Outline .....   | 44         |

|  |            |
|--|------------|
| <b>Chapter 2: Patient specific pixel-based weighting factor dual-energy x-ray imaging system</b> ..... | <b>46</b>  |
| 2.1: Abstract .....  | 46         |
| 2.2: Introduction .....  | 48         |
| 2.3: Materials and Methods.....  | 52         |
| 2.3.A: Theoretical Simulations.....  | 52         |
| 2.3.A1: Monoenergetic Case.....  | 52         |
| 2.3.A2: Beam Hardening Effects .....   | 53         |
| 2.3.A3: Scatter Effects .....  | 54         |
| 2.3.A4: Detector Effects .....   | 54         |
| 2.3.A5: Combination of Effects .....   | 56         |
| 2.3.B: Experimental Phantom Studies.....   | 56         |
| 2.3.B1: Weighting Factor Calibration Using Step Phantom.....   | 56         |
| 2.3.B2: Scatter Removal Experiment.....  | 59         |
| 2.3.B3: Rando Phantom Experiments.....   | 60         |
| 2.3.B4: PP-DE Algorithm Development .....  | 61         |
| 2.4: Results .....   | 64         |
| 2.4.A: PP-DE Algorithm .....   | 64         |
| 2.4.B: Parameters Affecting Weighting Factor .....   | 70         |
| 2.5: Discussion .....  | 74         |
| 2.6: Conclusion.....   | 78         |
| <b>Chapter 3: Conclusion</b> .....   | <b>79</b>  |
| 3.1: Modification of Step Phantom .....  | 80         |
| 3.2: Scatter Removal on ExacTrac .....   | 82         |
| 3.3: PP-DE Contrast Improvement.....   | 85         |
| 3.4: Weighting Factor Image Alignment.....   | 91         |
| 3.5: Density Scaling of Different Tissues .....  | 93         |
| 3.6: Bone-only PP-DE Algorithm .....   | 96         |
| 3.7: PP-DE with Bone Replaced by Soft-tissue .....   | 98         |
| 3.8: Final Remarks .....   | 100        |
| <b>Bibliography</b> .....  | <b>102</b> |
| <b>Appendix A</b> .....  | <b>111</b> |
| A.1: Monoenergetic Case .....  | 111        |

|                                    |     |
|------------------------------------|-----|
| A.2: Beam Hardening Effects .....  | 114 |
| A.3: Scatter Effects .....         | 115 |
| A.4: Detector Effects .....        | 117 |
| A.5: Tube mAs Effects .....        | 119 |
| A.6: Effect of Detector Gain ..... | 120 |
| A.7: Combination of Effects .....  | 121 |

## List of Tables

|   |    |
|---|----|
| <b>Table 1.1:</b> X-ray interaction schematics and interaction probabilities for photoelectric effect and Compton scatter. <sup>1</sup> .....   | 14 |
| <b>Table 1.2:</b> Effective atomic number, density, and Hounsfield Units for different tissue types.....  | 42 |
| <b>Table 2.1:</b> Measured ((a) and (b)) and theoretical ((c) to (e)) weighting factors demonstrating the effects of different imaging parameters. In (a) and (b) values are mean $\pm$ standard deviation..... | 73 |

## List of Figures

|   |    |
|---|----|
| <b>Figure 1.1:</b> Schematic of a general x-ray tube.....   | 3  |
| <b>Figure 1.2:</b> X-ray spectra from Spektr3.0 using both the TASMIC and TASMIP method for calculation.....  | 6  |
| <b>Figure 1.3:</b> Comparison of Spektr simulated HVLs with measured HVLs (without couch) from ExacTrac for the energy range 60 to 135 kVp.....   | 10 |
| <b>Figure 1.4:</b> Indirect TFT detection via a scintillator (a). Direct TFT detection using a semiconductor (b). <sup>1</sup> .....  | 12 |
| <b>Figure 1.5:</b> Detective quantum efficiency and average energy absorbed within the pixel per interaction for CsI. The product of both terms is also displayed in magenta.....   | 21 |
| <b>Figure 1.6:</b> A comparison between the value read by the detector using the approximation and integral forms for an energy range up to 140 keV.....  | 23 |
| <b>Figure 1.7:</b> An x-ray image acquired at 60 kVp before corrections (a). A dark image acquired at 40 kVp with the x-rays blocked with lead (b). A flood image acquired at 60 kVp (c). A corrected image (d) after flood and dark corrections.....   | 25 |
| <b>Figure 1.8:</b> A single exposure DE acquires both LE and HE images via a copper filter.....   | 30 |
| <b>Figure 1.9:</b> A double source DE system in CT acquires LE and HE images that are orthogonal to each other.....   | 33 |
| <b>Figure 1.10:</b> Flowchart for the ACNR algorithm.....   | 35 |
| <b>Figure 1.11:</b> A DE image without any noise reduction applied (a). The same DE image after an ACNR algorithm has been applied (b).....   | 36 |
| <b>Figure 2.1:</b> Step phantom with varying solid water and bone slabs placed on plastic stand (a). The phantom is placed on the treatment couch with the indicated geometries (b). The addition of a thin plastic plate with steel pins to the step phantom for scatter correction (c).....       | 57 |
| <b>Figure 2.2:</b> X-ray image of the step phantom at 60 kVp. ROIs are indicated by the red rectangles (a). Small circular ROIs in blue were made to estimate scatter under steel pins (b). ROI of only one region is illustrated for simplicity while similar ROIs utilized for other regions..... | 58 |

|   |    |
|---|----|
| <b>Figure 2.3:</b> Rando phantom with a cylindrical solid water plug (red arrow) to simulate a lung tumor.....  | 61 |
| <b>Figure 2.4:</b> Flowchart illustrating the steps of PP-DE algorithm.....   | 62 |
| <b>Figure 2.5:</b> CNR graphs (a) with the corresponding DE images for 20 cm soft-tissue when overlapped with either 2 cm or 6 cm bone overlap (b, c respectively). The optimal weighting factor is 0.780 for the 2 cm bone (e.g. representing rib) and 0.927 for the 6 cm bone (e.g. representing spine).....  | 65 |
| <b>Figure 2.6:</b> Soft-tissue (a) and bone (b) DRRs created by ray tracing through CT data from the Rando phantom. The total radiological DRR (c) includes both soft-tissue and bone. Weighting factor image (d) produced by using the <i>a-priori</i> information from the DRRs.....  | 66 |
| <b>Figure 2.7:</b> Clinical single energy x-ray image (a). Conventional DE image with a constant weighting factor across the image to cancel either the ribs (b) or spine (c). The PP-DE image (d) provides both rib and spine cancellation. Note the higher tumor contrast in the DE images compared to the single energy (red arrow). The pixel passed DE image provides both better tumor contrast and lower noise compared to the conventional DE images..... | 68 |
| <b>Figure 2.8:</b> Signal-to-noise (SNR) comparison between the PP-DE algorithm and conventional DE techniques demonstrating improved SNR at lower weighting factors.....   | 69 |
| <b>Figure 2.9:</b> The LE x-ray image with the steel pins (a). The LE scatter interpolated image (b) where most of the absolute scatter signal appears at thinner areas. The scatter fraction image (c) demonstrates that the majority of signal in thicker regions is from scatter. The scatter corrected LE image (d).....  | 71 |
| <b>Figure 2.10:</b> Ratios of weighting factors (measured/ simulated) for various soft-tissue and bone thicknesses.....   | 74 |
| <b>Figure 3.1:</b> The proposed modification of the step phantom of soft-tissue and bone slabs to allow storing 36 pre-calculated weighting factors outlined in the red square.....   | 81 |
| <b>Figure 3.2:</b> Mean ROI intensity in a region with 30 cm soft-tissue and 6 cm bone overlap as a function of air gap for both LE (a) and HE (b).....   | 83 |
| <b>Figure 3.3:</b> X-rays interacting with soft-tissue and bone with the addition of a tumor with thickness $t_2$ .....   | 85 |
| <b>Figure 3.4:</b> The additional contrast term as a function of weighting factor. The range at which the additional contrast term is negative is from 0 to 0.56.....   | 88 |



|   |     |
|---|-----|
| <b>Figure 3.5:</b> The tumor plate with 12 cylindrical tumors (a) and the tumor plate added to the step phantom (b).....  | 89  |
| <b>Figure 3.6:</b> Conventional DE images with constant weighting factors to cancel either 2 cm rib (a) or 6 cm spine (b) both on 20 cm soft-tissue. The PP-DE image (c) uses optimal weighting factors unique for each pixel. The contrast between the tumor and the background are displayed for bone overlap regions where (d) to (f) correspond to (a) to (c) respectively..... | 90  |
| <b>Figure 3.7:</b> PP-DE images formed by a misaligned weighting factor image and x-ray image where (a) is a 0 mm, (b) is a 5 mm shift, and (c) is a 10 mm.....   | 92  |
| <b>Figure 3.8:</b> Non-density scaled bone DRR (a). Density scaled cortical bone (b) and density scaled trabecular bone (c) DRRs. Density corrected bone DRR (d). Weighting factor images corresponding to the non-density scaled bone DRR (e) and the density corrected bone DRR (f).....  | 94  |
| <b>Figure 3.9:</b> An HE image of the Rando phantom with the trabecular and cortical bone inserts (a). The PP-DE images created using the non-density scaled bone DRR (b) and the density scaled bone DRR (c).....  | 95  |
| <b>Figure 3.10:</b> Soft-tissue (a) and bone (b) DRRs. The new soft-tissue DRR (c) has added bone thickness to replace regions that had air. Weighting factor images for the old-soft tissue and bone DRR (d) and the new soft-tissue DRR (e).....  | 99  |
| <b>Figure 3.11:</b> Clinical single energy x-ray image (a). PP-DE image made from the old soft-tissue and bone DRR (b) and the PP-DE image made from the new soft-tissue DRR (c).....   | 100 |
| <b>Figure A.1:</b> LE and HE beams are detected after passing through soft-tissue and bone with thicknesses $t$ and $b$ respectively.....   | 112 |

## **Abstract**

This thesis investigates the development and implementation of a novel patient specific pixel-based weighting factor algorithm for dual-energy x-ray imaging. The first chapter of this thesis is an introduction on the components of an x-ray imaging system, generation of spectra, imaging components, dual-energy, and radiotherapy. The second chapter is a manuscript submitted to the Medical Physics journal outlining the development of the algorithm and the generation of its dual-energy images. This chapter presents and discusses the improvements of dual-energy images generated by the novel algorithm in comparison to the conventional technique. This chapter also derives and validates the theoretical underlying analytical expressions by which various imaging parameters such as polyenergetic spectra, scatter, and detector response affect the weighting factor. The third and final chapter summarizes the accomplishments of the thesis goals and discusses various future avenues for further research.

## List of Abbreviations Used

|       |   |
|-------|---|
| ACNR  | Anti-correlated noise reduction                           |
| BEV   | Beam's eye view   |
| CBCT  | Cone-beam CT  |
| CNR   | Contrast-to-noise ratio                                   |
| CT    | Computed tomography                                       |
| DE    | Dual-energy   |
| DECT  | Dual-energy CT  |
| DQE   | Detective quantum efficiency                              |
| DRR   | Digitally reconstructed radiograph                        |
| EAE   | Energy absorption efficiency                              |
| EM    | Electromagnetic radiation                                 |
| FOV   | Field of view   |
| HE    | High-energy   |
| HU    | Hounsfield unit   |
| HPF   | High-pass filter  |
| IGRT  | Image guided radiation therapy                            |
| LE    | Low-energy  |
| LPF   | Low-pass filter   |
| PP    | Patient specific pixel-based                              |
| PP-DE | Patient specific pixel-based weighting factor dual-energy |
| QDE   | Quantum detection efficiency                              |
| ROI   | Region of interest  |
| SE    | Single-energy   |
| SECT  | Single-energy CT  |
| SLS   | Simple log subtraction                                    |
| SNR   | Signal-to-noise ratio                                     |
| SSH   | Simple smoothing of the high-energy image                 |
| TFT   | Thin-film Transistor                                      |
| Z     | Atomic number   |

## Acknowledgements

I would like to give a giant thank you to all of the wonderful people who have encouraged and assisted me in the completion of this work. I would like to thank my fellow classmates John, Cody, Courtney, Lin, and Parisa for helping me through the course work. It has been an absolute pleasure working with each and every one of you, and I have no doubt that you will all go on to do tremendous things in the field. I'd like to emphasize my thanks to John and Cody for teaching me how to code in MatLab and being very patient with me. You both knew that I was very new to coding, so having both of you around for the laughs and lessons was VERY much appreciated.

I would like to thank my friends outside the field for helping me destress during difficult times. A massive thanks to my parents Chris and Jane as well as my sisters Katie, Allison, and Amy for assuring me that I am capable of completing this work and supporting me through all of the difficult times along the journey. Anytime I was feeling defeated with the workload, you guys always helped me catch my second wind to push through it.

A big thanks to our machinist Ian Porter for being exceptionally handy and crafting all the necessary tools and equipment needed to complete this work. Another thanks to the ACOA innovation fund for supporting our work.

A special thanks to my committee members Dr. James Robar and Dr. Alasdair Syme for keeping me on my toes during the committee meetings. Both of your suggestions to improve this work were considered and led to great results.

Lastly, I would like to extend an enormous thank you to my supervisor Dr. Mike Sattarivand and colleague Dr. Sahar Darvish-Molla for being the most helpful with this work. My research skills have improved tremendously because of you both, and without your dedication to both myself and this work, none of this would have been possible. I am looking forward to seeing where this dual-energy work goes and how it will improve patient care.

## Chapter 1: Introduction

Many medical diagnostic imaging systems are based off the production of different kinds of electromagnetic radiation (EM). Forms of EM radiation include radio waves, visible light, x-rays, and gamma rays. EM radiation exhibit characteristics similar to both a wave and a discrete particle. Different EM radiation have different wavelengths and frequencies, which are inversely proportional to one another since the speed of EM radiation is uniform in a medium. The particle-like behaviour comes from discrete packets (quanta) of energy called photons. The energy of a photon is given in eV, which is the energy of an electron as it accelerates through a potential difference of one volt in a vacuum.

X-rays are probably the most common form of EM radiation used in diagnostic imaging. It is classified as ionizing radiation, meaning that the photon's energy may be sufficient enough to remove electrons from an atom. Most x-rays are produced when an electron with high kinetic energy interacts with a material and transfers its energy into the form of EM radiation.

In this chapter, the components on an x-ray imaging system are described, followed by interactions of x-rays with matter. Next, imaging concepts, dual-energy (DE) imaging techniques and their role in radiotherapy applications are discussed. Lastly, the research goals of this thesis are outlined.

## **1.1. X-ray Imaging System**

X-ray imaging systems are comprised of both the x-ray tube which produces x-rays, and the detector which creates an image from the flux of photons incident on it after passing through the patient. Several parameters and phenomena affect the output of x-rays from the tube as well as the detection of photons when they reach the detector.

### **1.1.1. X-ray Tube**

The typical x-ray tube is comprised of a cathode, an anode, glass window, and a vacuum tube, in which a large electric potential difference is applied between the electrodes to accelerate the electrons as per **Figure 1.1**.

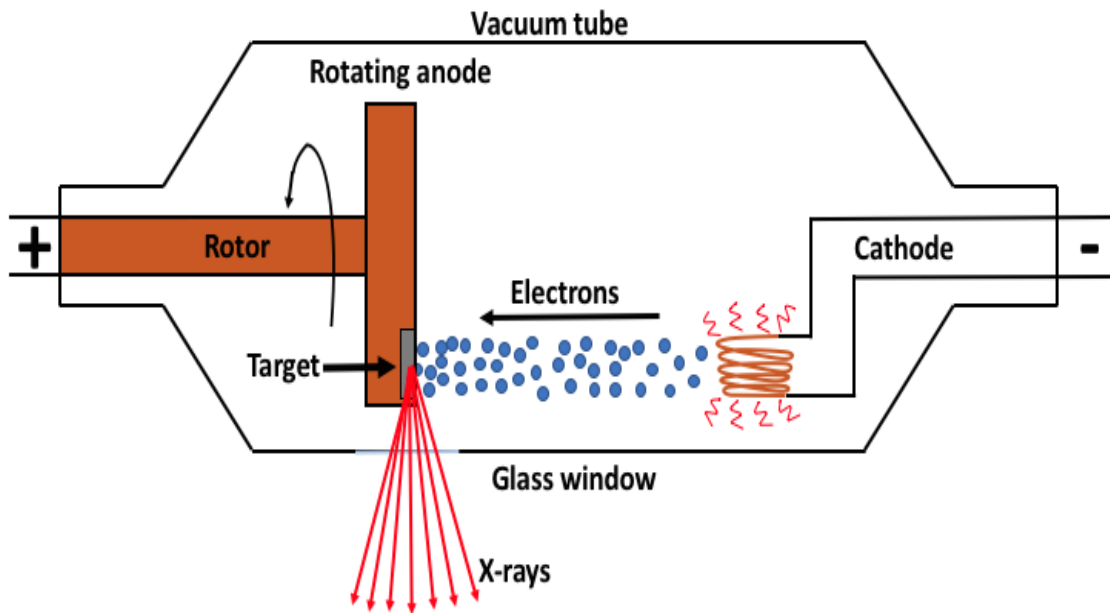


**Figure 1.1:** Schematic of a general x-ray tube.

An x-ray generator allows for the selection of various parameters such as tube current, tube voltage, and exposure time. The tube voltage governs the range of energies for the x-rays, where the peak kilovoltage (kVp) is the maximum voltage. Varying the tube current (mA) has an effect on the number of electrons that travel across the x-ray tube from the cathode to the anode. The exposure time controls how long the tube is producing electrons. The product of the tube current and exposure time is commonly used as a single quantity known as the mAs.

The cathode is a negatively charged electrode, which typically includes a tungsten filament. The cathode produces electrons through thermionic emission when a voltage is applied. The anode is positively charged, and therefore attracts the electrons from the cathode when a voltage is applied between them. Embedded inside the anode is usually a tungsten target, on to which the electrons impinge on. Upon collision, the majority of

kinetic energy from the electrons produces heat, but a small fraction (~1%) is converted to bremsstrahlung radiation.

### **1.1.2. Bremsstrahlung Radiation**

When accelerated electrons travel in close proximity to the positively charged nucleus of an atom, coulombic forces decelerate the electron. As the electron slows down, the kinetic energy is lost and converted into x-ray photons. The production of bremsstrahlung x-rays per atom is proportional to  $\frac{Z^2}{m^2}$ , where  $Z$  is the atomic number of the material and  $m$  is the mass of the incident particle.<sup>1</sup>

The bremsstrahlung spectrum is a plot of the relative x-ray intensity as a function of photon energy. An unfiltered bremsstrahlung spectrum demonstrates an inverse linear relation, where the relative intensity decreases as the photon energy increases. When the bremsstrahlung spectrum is filtered, there is an increase in relative intensity up to about one third of the maximum energy (the effective energy), and then a gradual decrease in relative intensity after.

### **1.1.3. Simulation of Spectra**

Simulations can be used to generate x-ray spectra. The Spektr toolkit was developed for research purposes in diagnostic imaging.<sup>2,3</sup> Early versions of this software could compute x-ray spectra based on a method called TASMIPS (tungsten anode spectral model using interpolating polynomials). TASMIPS simulates x-ray spectra



(photons/mm<sup>2</sup>/mAs at 100 cm from the source) in 1 keV energy bins in a diagnostic range of 30 to 140 kVp.<sup>3</sup> The spectra produced are based off measured constant potential x-ray spectra published by Fewell et al.<sup>4,5</sup> The software was developed to not only generate and plot x-ray spectra, but also calculate various characteristics of the x-ray beam such as exposure, half value layer (HVL defined below), mean energy, etc. Spektr is capable of producing x-ray spectra while varying different input parameters such as choice of tube voltage, total Aluminum (Al) filtration, and % kV ripple. Additionally, the software is able to take a generated spectrum and filter it further by a specific thickness of a compound or element. Information regarding the mass attenuation coefficients and densities of available compounds and elements are supplied from the National Institute of Standards and Technology (NIST) which are then bicubic-interpolated to 1 keV bins.<sup>6</sup>

Improvements in the Spektr toolkit were implemented by Punnoose et al.<sup>2</sup> They developed a newer method of producing x-ray spectra with a better energy resolution than TASMIPS. The newer version calculates x-ray spectra based on the tungsten anode spectral model using interpolating cubic splines (TASMICS). In addition to an improvement on energy resolution, TASMICS also avoids systematic measurement errors that could be caused from charge pile up and electronic noise.<sup>2</sup> The updated Spektr toolkit also allows for a greater range of beam energies from 20 to 150 kVp. The TASMICS model has a default inherent filtration of 1.6 mm Al, which matches the inherent filtration of TASMIP. A comparison between an x-ray spectrum at 140 kVp with 3.4 mm Al of total filtration is provided in **Figure 1.2**.

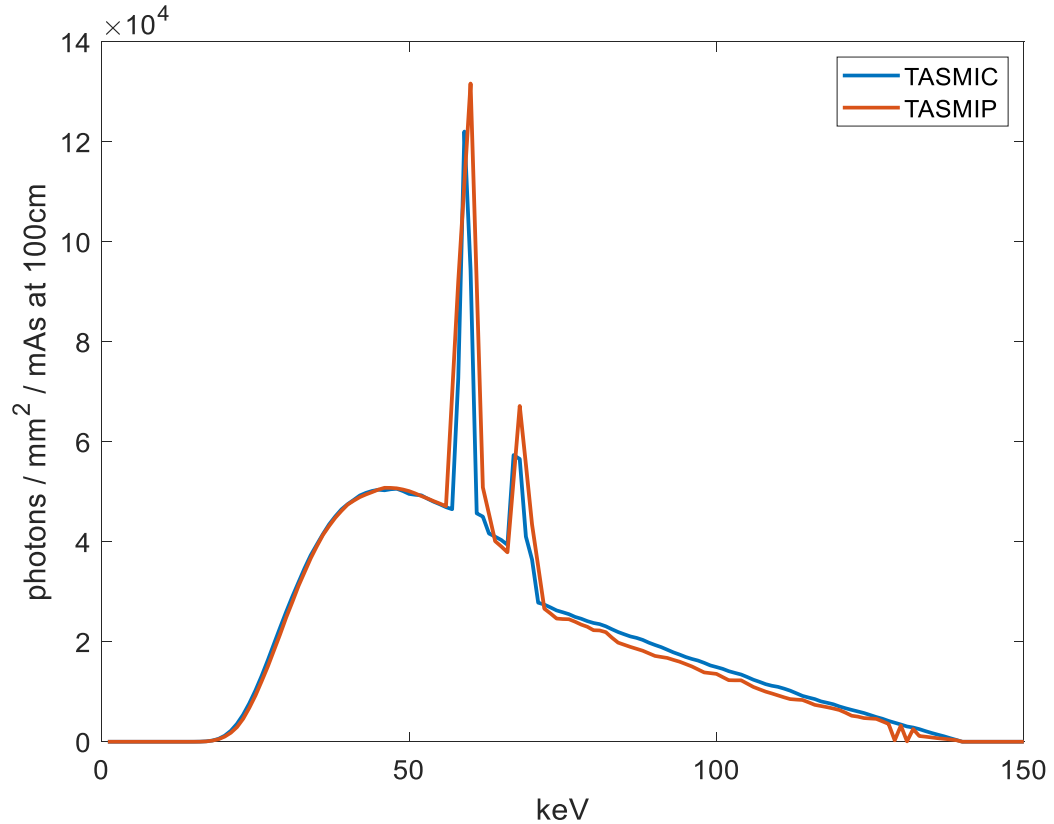


**Figure 1.2:** X-ray spectra from Spektr3.0 using both the TASMIC and TASMIP method for calculation.

The TASMIP spectrum is less smooth and fluctuates greatly in the higher energy range compared to the TASMIC spectrum. Additionally, the fluence of the characteristic peaks in the TASMIP spectrum are somewhat higher than the TASMIC peaks and slightly shifted to a higher energy.

There are some limitations to the Spektr software. Both TASMIP and TASMICS generate spectra using a tungsten anode, meaning that simulations for mammography may not be correct since those systems may have molybdenum or rhodium anodes. Moreover, simulations of realistic patient geometry and scatter cannot be generated in Spektr. This can be problematic because the realistic spectrum producing the image when

incident on the detector includes scatter from the various components on the beam path including the patient.

Monte Carlo (MC) software is another simulation technique which could be used to generate x-ray spectra. One of the most common MC codes used is EGSnrc (electron gamma shower).<sup>7</sup> EGSnrc is capable of modeling the exact source and detector geometry as well as patient anatomy, to give more realistic results. Part of this code includes the BEAMnrc package which allows modeling of the radiation source (e.g. the x-ray tube) and photon and electron transportation through matter. Additionally, BEAMnrc is able to estimate radiation delivered to a patient via the DOSXYZnrc component. EGSnrc is able to incorporate realistic imaging effects that Spektr is unable to model such as patient scatter. Although not trivial to implement, in principle MC could also be used to model the image formation by the x-ray detector.

Although MC is a powerful tool for simulation, it also has drawbacks. Results from MC simulation can be accurate, but the quality of its outputs depends heavily on the quality of its inputs. In order to produce the best results, the geometry and detailed material specifications of the x-ray imaging system need to be used as input. Due to proprietary reasons, information on the exact geometry of the x-ray tube, detector, and other parts of the system may not be available to the researcher. Another problem with MC simulation is that it can run very slowly depending on the task. For some research purposes, the MC simulation time can range from hours to days and sometime even more. Additionally, the efficiency of MC depends on the specifications of the available computation power. MC simulations may require a cluster of computers with substantial memory storing capabilities. The cost of implementing a cluster of computers can

become very high, whereas other simulation tools such as Spektr can be downloaded on a single computer with a quick simulation time.

#### 1.1.4. Half Value Layer

The output of an x-ray tube is not mono-energetic to quantify its energy with a single value. HVL is a simple practical method to quantify the *quality* of the beam in terms of its energy. The HVL is defined as the amount of filter material required (often measured in mm Al) to reduce the intensity of the beam to half of its initial amount. When x-ray spectra have higher energies, a thicker HVL is required to reduce the output by half.

For diagnostic imaging the HVL of a spectrum is measured under the conditions of narrow-beam geometry which means that scattered photons are excluded from measurement by collimating the beam. The HVL is related to material attenuation and thus can be expressed as:<sup>1</sup>

$$HVL = \frac{\ln(2)}{\mu} \quad (1.1)$$

where  $\mu$  is the linear attenuation coefficient of the filter material.

Spektr is capable of estimating the HVL of a given spectrum. The software takes input parameters such as the x-ray energy spectrum, number of HVLs to calculate, and the atomic number of the filter material. The spectrum is simulated, then quanta per exposure is calculated as follows:<sup>8</sup>

$$\frac{\Phi}{X}(E) = \frac{5.43 \times 10^5}{\left(\frac{\mu(E)}{\rho}\right)_{en}} \frac{\text{photons}}{E \text{ mm}^2 \text{ mR}} \quad (1.2)$$

where  $\Phi$  is the photon fluence  $\left(\frac{\text{photons}}{\text{mm}^2}\right)$ ,  $X$  is the exposure (mR),  $\left(\frac{\mu(E)}{\rho}\right)_{en}$  is the mass energy absorption coefficient for air, and  $E$  is the energy. To calculate the total exposure, Eq.(1.2) is inverted and integrated over the entire energy range:<sup>3</sup>

$$\text{Total exposure (mR)} = \int_0^{E_{max}} \frac{X}{\Phi}(E)\Phi(E)dE \quad (1.3)$$

Once the total exposure is calculated, the Spektr code calculates the HVL of the material needed to reduce the exposure by  $2^{-n}$  in mm. By matching the measured HVL vs Spektr calculated HVL from simulated spectra, x-ray tubes can be modeled in Spektr. A comparison of matching Spektr simulated HVLs to the measured values for an ExacTrac (Brainlab AG, Germany) x-ray tube is demonstrated in **Figure 1.3**. To obtain this match, the total Al filtration in Spektr was set to 3.3 mm.

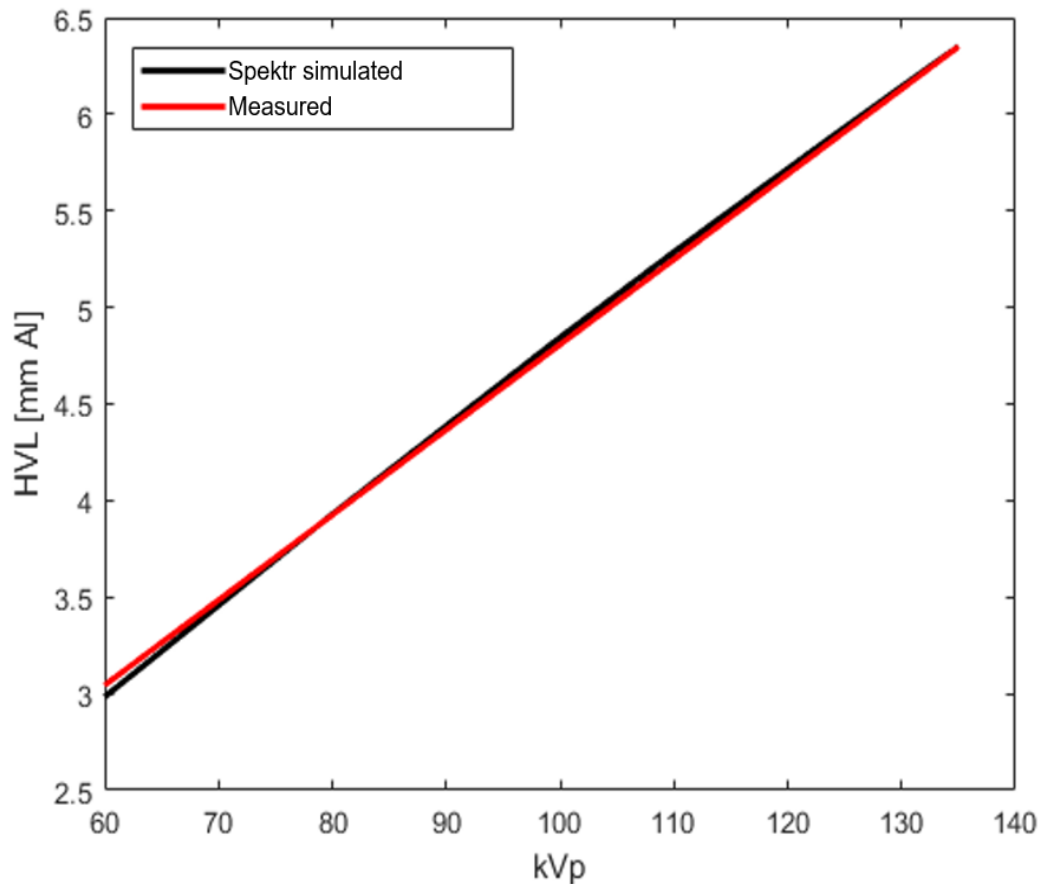


**Figure 1.3:** Comparison of Spektr simulated HVLs with measured HVLs (without couch) from ExacTrac for the energy range 60 to 135 kVp.

Results from **Figure 1.3** clearly show an excellent agreement in matching Spektr simulated HVLs to realistic HVLs measured with a real imaging system.

### 1.1.5. X-ray Detector

Aside from the x-ray tube, which is the main source of the x-ray photons, the other important component of the imaging system is the detector which creates an image after photons pass through a patient. Most former x-ray imaging systems used a screen-

film technique to create the radiographic images. Today, most commonly a digital approach to x-ray imaging has been developed and implemented, and a handful of the imaging detectors used are flat panel detectors with thin-film transistor (TFT) arrays. Flat panel TFT detectors consist of arrays of numerous individual detector elements called dexels.<sup>1</sup> Inside each dexel both a light sensitive (where signal is collected) and light insensitive (where electronic components exist) region exist. The TFT array has three different connections called the gate, source and drain. Also, within the electronics is a charge collecting electrode which stores the charge generated by the deposition of incident photon energies across the dexel. After the detector is exposed to radiation, the TFT is activated and one by one, each gate line to every dexel opens allowing charge to flow to the drain line which is followed by a charge amplifier. These amplifiers convert the charge to a voltage which is digitized to produce a gray scale value for each dexel.

The TFTs can be either of two kinds; direct or indirect as illustrated in **Figure 1.4**. An indirect TFT uses a scintillator (**Figure 1.4a**) to convert the x-rays to light. The scintillator is placed on the front surface of the flat panel array so that x-rays interact first with the scintillator. Common scintillator materials used in radiography are CsI and  $Gd_2O_2S$ . Some scintillating material can be grown in columns forming a light guide for the light photons to reduce the lateral spread. Once the x-ray photons interact with the scintillator, light photons are produced and interact with a photodiode. The photodiode (not shown in **Figure 1.4a**) converts the light photons into a charge which is stored in the charge collecting electrode. Although the crystal structure of the scintillator helps facilitate the flow of light photons, the lateral light spread causes a reduction in spatial resolution.

A direct TFT generally uses amorphous selenium (a-Se) as a semiconductor (**Figure 1.4b**) which when irradiated, produces electron ion pairs proportional to the exposure. The ion pairs follow electric field lines, thus minimizing the amount of lateral spread. This means that the electronic signal that is detected from one x-ray photon is almost fully collected in a single detector element. This focus of collection in one detector element results in an improved spatial resolution compared to the indirect TFT.

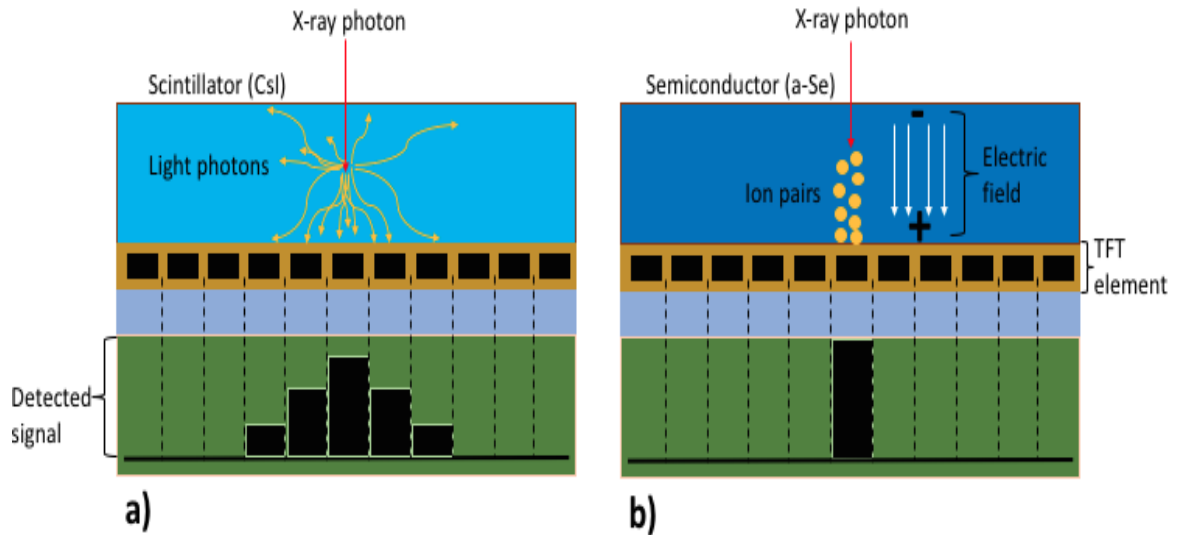


**Figure 1.4:** Indirect TFT detection via a scintillator (a). Direct TFT detection using a semiconductor (b).<sup>1</sup>

## 1.2. X-ray Interactions with Matter

After the x-rays in the tube are produced via bremsstrahlung in the target, most of them leave the tube and may interact with matter. There are three outcomes when a photon is going through matter: it may be absorbed, scattered, or penetrate without any



interaction. The most useful result in diagnostic imaging are absorption and transmission of x-rays, while scatter is undesirable.

The photon interaction process could be Rayleigh scattering, Compton scattering, photoelectric absorption, or pair production. Rayleigh scattering occurs for very low energy x-rays which are generally attenuated by the tube window and housing. Pair production interactions take place only when the x-rays have an energy greater than 1.02 MeV which is outside diagnostic range and thus not relevant for imaging. Therefore, the two most important photon interactions in diagnostic imaging is photoelectric absorption and Compton scattering. **Table 1.1** illustrates the schematics of these events.

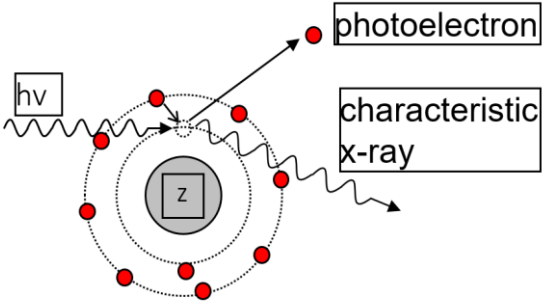
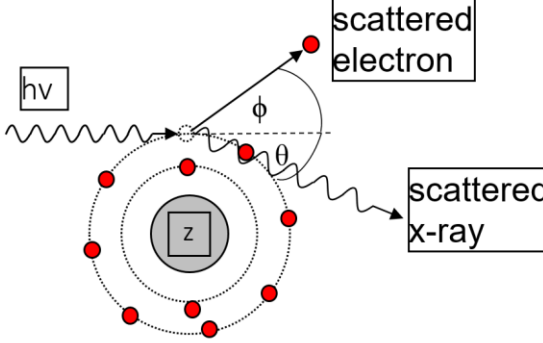
The photoelectric effect happens when an incident photon interacts directly with a bounded electron in an atom, transferring all of its energy to the electron and ejecting it from its orbital shell. This could only happen when the incident photon's energy is equal to or greater than the binding energy of the orbital electron. When the electron is ejected from its shell, the atom becomes unstable with a vacancy and an outer shell electron can drop down to fill the vacancy. During this process, a characteristic x-ray photon is produced with an energy equivalent to the difference between the two shells involved.

The photoelectric interaction highly depends on the atomic number of the material (varies with  $Z^3$ ) thus bones ( $Z_{\text{eff}} \sim 12.3$ ) have high contrast compared to soft-tissue ( $Z_{\text{eff}} \sim 7.5$ ).<sup>9</sup>

The Compton scattering interaction occurs between an incident photon and a free electron. Unlike the photoelectric effect, there is not an atomic number dependence. However, the probability of a Compton interaction depends on the electron density of the material, which is also proportional to the physical density. In soft-tissues, Compton scattering events take dominance over photoelectric interactions for energies greater than

~25 keV. However, due to the high atomic number of bone, Compton interactions in bone do not overtake photoelectric events until energies greater than ~40 keV.<sup>9</sup>

**Table 1.1:** x-ray interaction schematics and interaction probabilities for photoelectric effect and Compton scatter.<sup>1</sup>

| Interaction                    | Schematic  | Dependence  |
|--------------------------------|--|---|
| <p>a) Photoelectric effect</p> |  <p>The diagram shows an atom with a central nucleus labeled 'Z' and several concentric electron shells. An incident x-ray photon, represented by a wavy line and labeled 'hν', is shown entering from the left. An arrow points from the nucleus to an electron in an outer shell, which is labeled 'photoelectron'. Another arrow points from the nucleus to a wavy line labeled 'characteristic x-ray', representing the emission of a secondary photon.</p>  | $\frac{\tau}{\rho} \propto \frac{Z^3}{E^3}$         |
| <p>b) Compton scatter</p>      |  <p>The diagram shows an atom with a central nucleus labeled 'Z' and several concentric electron shells. An incident x-ray photon, represented by a wavy line and labeled 'hν', is shown entering from the left. It strikes an electron in an outer shell. An arrow points from the electron to another electron labeled 'scattered electron'. The scattered photon is shown as a wavy line labeled 'scattered x-ray' moving away at an angle θ. The angle φ is also indicated between the incident photon's path and the scattered electron's path.</p> | $\frac{\sigma_C}{\rho} \propto \rho_e \propto \rho$ |

## 1.3. Components of Image Quality

### 1.3.1. Noise

In diagnostic imaging, noise degrades the image quality limiting the ability to visualize anatomy. There are various kinds of noise which arise from different sources and are unwanted in the image. Fortunately, there have been algorithms and techniques developed to reduce the noise as much as possible in an image.

Quantum noise is directly related to the x-ray tube output of an imaging system. Finite number of photons interact in the detector, thus the severity of quantum noise in an image is dependent on the number of these photons that form the image. The distribution of quanta follows Poisson statistics where the number of incident x-rays per unit (or pixel) area can be reported. For  $N$  incident quanta on a pixel, the noise per pixel  $\sigma$  is given by:<sup>1</sup>

$$\sigma = \sqrt{N} \quad (1.4)$$

The amount of noise relative to the actual incident quanta is:

$$\text{Relative noise} = \frac{\sigma}{N} \quad (1.5)$$

Another important metric used to quantify the strength of the signal relative to the noise is the signal-to-noise ratio (SNR). The SNR is often used as an indicator of how much useful information is in an image. The SNR is also the reciprocal of the relative noise, and therefore can be calculated using the following:<sup>1</sup>

$$SNR = \frac{N}{\sigma} \quad (1.6)$$

The quantum noise in an image can be reduced by increasing the number of quanta, e.g. by higher mAs or kVp values .

Another form of noise stems from the actual patient anatomy, known as anatomical noise. This is the anatomy that is not of interest but is present in the image. For example, diagnosing a lung nodule which has overlaps of rib and other bony obscuring structures can be an example of anatomical noise.

### 1.3.2. Contrast

An important quantity used to measure the image quality of a radiograph is the contrast. The subject contrast is defined as the difference in x-ray intensity that passes through a lesion compared to the adjacent tissues. The subject contrast involves x-ray interactions with the patient, but not the detector. Due to the differential attenuation between different types of tissues in the human body, there will be more x-rays that penetrate through some tissues than others. The subject contrast is higher at lower energies. This is due to a dominance in the photoelectric effect at lower energies especially for tissues with a higher atomic number.

A common measure of image quality is contrast-to-noise ratio (CNR) which describes contrast in the presence of noise. CNR is calculated by taking the average signal in a region of interest (ROI)  $\bar{x}_s$  and comparing it to the average signal in an ROI in the background  $\bar{x}_{bg}$ . Additionally, the noise of the background is calculated  $\sigma_{bg}$  which is the standard deviation of the signal in the background ROI. The CNR is calculated as:<sup>1</sup>

$$CNR = \frac{|\bar{x}_s - \bar{x}_{bg}|}{\sigma_{bg}} \quad (1.7)$$

The CNR is used to make a relative comparison between the signal in an image and the noise, which is useful for tasks such as the optimization of tumor contrast for various imaging parameters.

### 1.3.3. Scattered Radiation

In diagnostic imaging, x-rays may interact and scatter in the patient. However, scattered radiation degrades the image quality by reducing the contrast in the radiographic image, thus is undesirable. The main contributor of scattered radiation is from Compton scatter interactions with soft-tissue. The amount of scattered radiation that reaches the image receptors depend on various parameters such as the field size and patient thickness.

The amount of scatter signal detected in an image can be quantified by comparing it to the amount of primary radiation. This is described by the scatter-to-primary ratio  $SPR$ :<sup>1</sup>

$$SPR = \frac{S}{P} \quad (1.8)$$

where  $S$  is the scatter signal and  $P$  is the primary signal. The scatter fraction  $F$  is defined by:<sup>1</sup>

$$F = \frac{S}{S+P} \quad (1.9)$$

which indicates how much scatter contributes to the total signal detected.

The inclusion of x-ray scatter is inevitable when imaging a patient. However, there have been techniques and equipment developed in order to reduce the amount of scatter contribution to the primary signal. Collimators may be used to reduce scatter from

an x-ray beam by reducing the area of exposure. Collimators are made of high atomic number materials such as lead to block x-rays outside the field of view (FOV). Another technique used is the implementation of a large air gap between the patient and the image receptor. Due to the divergence of the scattered photons, the detection of scattered radiation with the image receptor decreases due to photons missing the detector area.

The most common method for reducing scatter is the use of anti-scatter grids. An anti-scatter grid is an array of narrow parallel bars of a material that can readily attenuate x-rays such as lead. They are designed to allow the primary photons to pass through the slits and absorb scattered radiation that travel in a different direction from the primary beam.

#### **1.3.4. Detective Quantum Efficiency Vs. Absorption Efficiency**

The detective quantum efficiency ( $DQE(f)$ ) is another imaging metric which is used to describe the overall frequency-dependent SNR performance of the imaging system, where  $f$  is the frequency. At zero frequency, DQE is reduced to quantum detection efficiency (QDE), i.e.  $\alpha$ , which describes the efficiency of the detector in the detection of incident x-rays. For a monoenergetic beam:<sup>1</sup>

$$DQE(0) = \alpha = 1 - e^{-\mu_d t_d} \quad (1.10)$$

where  $\mu_d$  and  $t_d$  are the linear attenuation coefficient and the thickness of the detector material. In general,  $\alpha$  is a function of energy as it depends on the energy dependant  $\mu_d$ .

### 1.3.5. Detector Modeling

Using the concepts described above the pixel value read by the detector may be modeled. The average x-ray spectral distribution  $q(E)$  incident on the detector (units photons/mm<sup>2</sup>/mAs at 100 cm in Spektr) after passing through some material (e.g. a patient) is given as:<sup>10</sup>

$$q(E) = q_0(E)T(E)(1 + s(E)) \quad (1.11)$$

where,  $q_0(E)$  is the initial x-ray beam before attenuation,  $T(E)$  is the transmission of  $q_0(E)$  spectrum after interaction with the material, and  $s(E)$  is the scatter-to-primary ratio of the rays reaching the detector. In the case, where almost all scattered radiation is corrected, the scatter-to-primary can be  $\approx 0$ , thus the previous equation is simplified to:

$$q(E) = q_0(E)T(E) \quad (1.12)$$

When the spectrum interacts with an energy-integrating detector, the average binned-pixel value  $d$  read by the detector is recorded as:<sup>10</sup>

$$d = kA \int_0^{kV} q(E)\alpha(E)E_a(E)dE \quad (1.13)$$

where  $k$  is a proportionality constant,  $A$  is the area of the binned-pixel,  $\alpha(E)$  is the detector quantum efficiency, and  $E_a(E)$  is the average energy absorbed in the binned-pixel per interacting photon. The average energy absorbed is calculated based on the assumption that there is a partial reabsorption of characteristic photons which causes half of the energy to escape area  $A$  while the other half is reabsorbed. Therefore, the average energy absorbed in the binned-pixel per interacting photon is:<sup>10</sup>

$$E_a(E) = E_{ab}(E) + (E - E_{ab}(E))/2 = (E_{ab}(E) + E)/2 \quad (1.14)$$

where,  $E_{ab}(E)$  is the energy absorbed in the detector at the interaction site, and  $E$  is the incident photon energy. The energy absorbed  $E_{ab}(E)$  at the interaction site per incident photon with energy  $E$  can be described as:<sup>11</sup>

$$E_{ab}(E) = E \frac{\mu_{en}(E)}{\mu(E)} \quad (1.15)$$

where  $\mu_{en}(E)$  and  $\mu(E)$  are the energy absorption and linear attenuation coefficients respectively. The product of  $\alpha(E)$  and  $E_a(E)$  is given by:

$$\alpha(E) \times E_a(E) \quad (1.16)$$

The detector quantum efficiency  $\alpha(E)$ , and average absorbed energy per interacting photon  $E_a(E)$  for a CsI detector of thickness 0.021 cm, and their product are plotted in **Figure 1.5**.



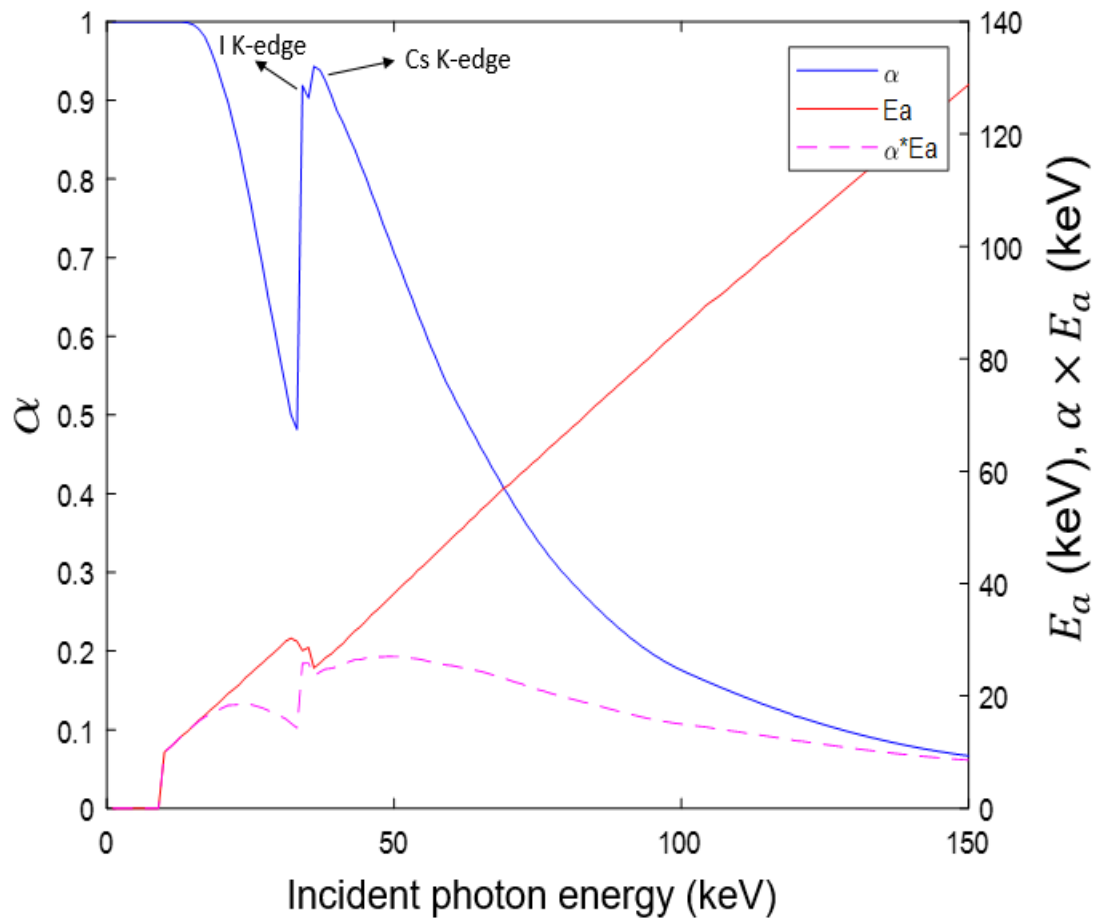


**Figure 1.5:** Detective quantum efficiency and average energy absorbed within the pixel per interaction for CsI. The product of both terms is also displayed in the magenta.

At low energies, the detector quantum efficiency is close to unity, indicating that essentially all lower energy photons interact with the detector and absorbed within the pixel. At higher energies photons are more likely to transmit through the detector. The large fluctuation is due to the Cs K-edge (at 36 keV) and I K-edge (at 33 keV), indicating that there is a large increase in photon interactions above the binding energy of Cs and I. The average energy absorbed per interaction is small for photons with lower energies, but increases with energy since higher energy photons will release more energetic electrons

depositing more energy. Except for the K-edge,  $\alpha(E)$  decreases while  $E_a(E)$  increases as the energy increases. The product of the two variables gives a curve that is relatively constant with energy. This described the coarse approximation that the majority of energy absorbed is around the average energy of the spectrum.

Modeling pixel value for an energy integrating detector requires a knowledge of polyenergetic x-ray spectra incident on the detector and the energy dependant  $\alpha$  and  $E_a$  terms. However, an approximation may be used in simple cases. This approximation involves finding a single energy averaged  $\alpha$  and  $E_a$ . Assuming the  $\alpha$  and  $E_a$  terms are constant over the energy range, the pixel value is:

$$d \approx kA\bar{\alpha}\bar{E}_a \int_0^{kV} q(E)dE \quad (1.17)$$

A comparison between the original integral equation and the approximated version is illustrated in **Figure 1.6**.

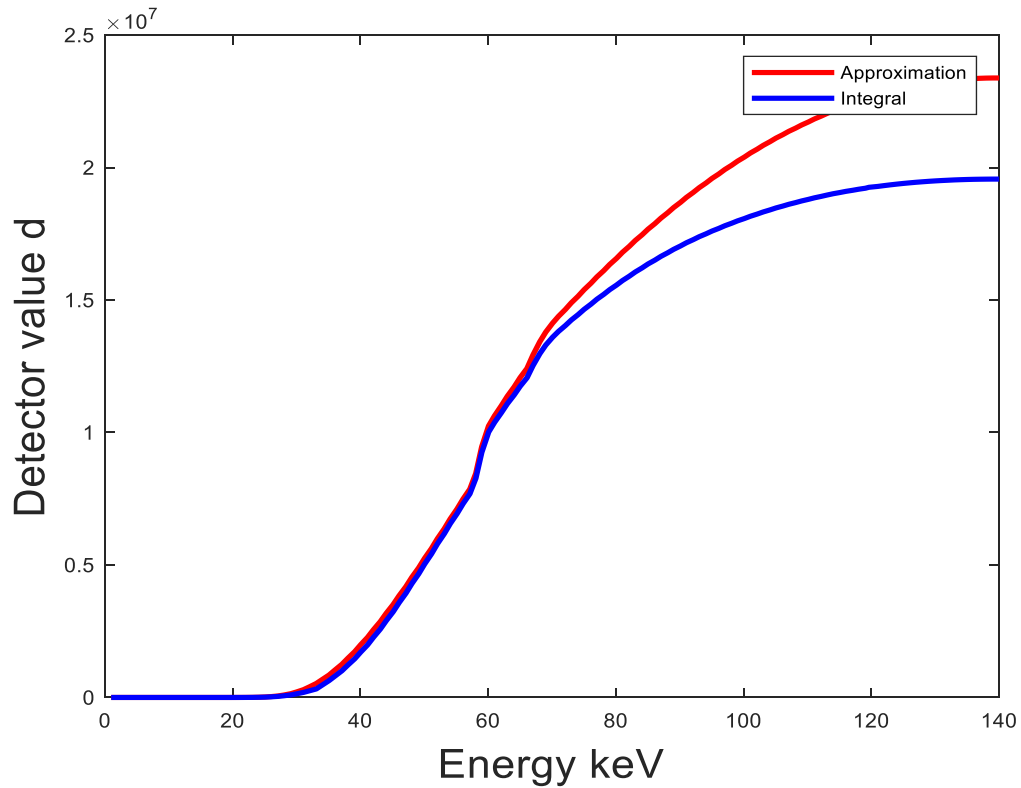


**Figure 1.6:** A comparison between the value read by the detector using the approximation and integral forms for an energy range up to 140 keV.

For the first half of energy values, below  $\sim 70$  keV the detector values for the approximation and integral are nearly identical. However, at the higher energies  $> 70$  keV, the approximation method overestimated the detector reading. This may be because the  $\alpha$  values become very small at higher energies which would make the detector reading lower for the integral.

### 1.3.6. Flat Field Correction Algorithm

In flat panel detectors, a number of parallel channels are used for reading out detector array elements. Each of these channels use amplifier circuits which may not be

perfectly tuned to neighbouring channels. These variations in channel amplifications can cause the detector elements to be read with a different offset noise and gain characteristic, causing detector dependant structure noise in the image. However, structure noise is spatially constant for a period of time, which allows for easy corrections in the images.

Detector correction is based on using flood and dark images. For example, a typical uncorrected 60 kVp image of a chest phantom is illustrated in **Figure 1.7a**. Dark images (also known as offset images) are acquired by acquiring an image with no x-rays (or by completely blocking all incident x-rays from reaching the detector with a thick lead block). **Figure 1.7b** displays a sample dark image. Flood images (also known as gain images) are acquired by ensuring that there is no object in the path of the x-ray beam (**Figure 1.7c**). The flat field correction algorithm uses dark and flood images to correct for detector structured noise. The corrected image  $I_{corrected}$  is calculated by:<sup>1</sup>

$$I_{corrected} = g \frac{I_{raw} - I_{offset}}{I_{gain} - I_{offset}} \quad (1.18)$$

where,  $I_{raw}$  is the uncorrected x-ray image,  $I_{offset}$  is the dark image,  $I_{gain}$  is the flood image, and  $g$  is the mean gray scale of the denominator. An example of the corrected image is in **Figure 1.7d**. Although it is difficult to realize the difference with the uncorrected image in this case, the impact of this correction is important for DE imaging. This is because DE logarithmic subtraction plays a large effect on the signal acquired from DE imaging, and can amplify the structure noise in the image further.

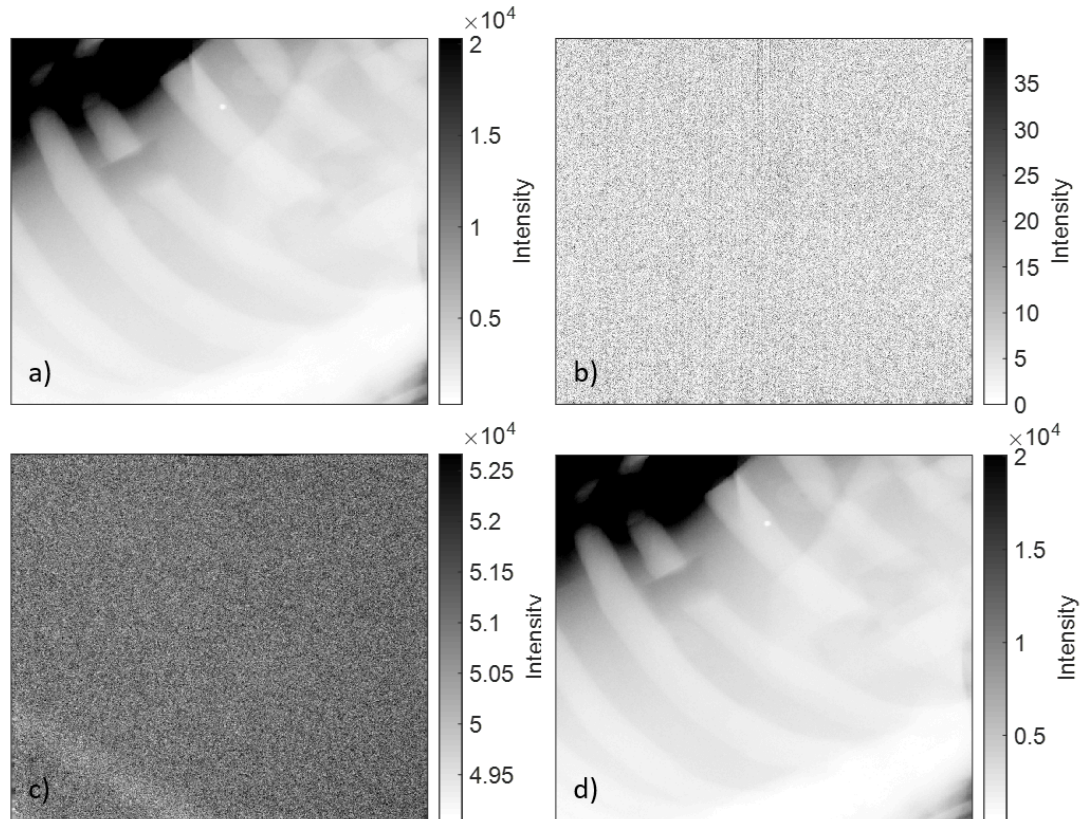


**Figure 1.7:** An x-ray image acquired at 60 kVp before corrections (a). A dark image acquired at 40 kVp with the x-rays blocked with lead (b). A flood image acquired at 60 kVp (c). A corrected image (d) after flood and dark corrections.

#### 1.4. Dual-energy X-ray Imaging

DE imaging techniques have been developed to improve diagnostic imaging by enhancing the image quality of radiographs. Its advantage over single energy (SE) radiography is the removal of anatomical noise thus enhancing tumor visualizations.<sup>12,13</sup> DE images are produced by acquiring a low energy (LE) and high energy (HE) image and combining the two in order to cancel a specific tissue type. A variety of different methodologies for DE imaging have been established such as simple logarithmic

subtraction, decomposition of basis materials, single exposure, double exposure, single source, and double source.

#### 1.4.1. Simple Logarithmic Subtraction

The simple logarithmic subtraction (SLS) technique is based on the x-ray attenuation passing through bone and soft-tissue using Beer's Law for both LE and HE beams as in **Figure A.1** in the Appendix. Given a patient with soft-tissue thickness ( $t$ ) and bone thickness ( $b$ ), the equation for Beer's Law with an initial x-ray intensity  $I_{L0}$  and  $I_{H0}$  for both LE and HE beams is given by Eq.(A.1) and Eq.(A.2). The Beer's Law equations are then manipulated by taking the logarithm of both sides. The last step in the technique is the subtraction of the LE and HE image while introducing a weighting factor  $\omega$  for tissue cancellation. A soft-tissue only DE image  $I_{DE}$  (with bone suppression) is created from Eq(A.24) in the Appendix. Similarly, if a bone only DE image is desired, the HE image is subtracted from the LE image, and a soft-tissue cancelling weighting factor  $\omega_b$  given by Eq(A.37) in the Appendix.

One of the most important parameters in the SLS method is the selection of weighting factor value. Theoretically, the weighting factor to cancel bone can be derived by setting the terms with bone to 0 as follows:

$$\ln(I_{DE}) = \ln(I_{H0}) - \mu_H^t t - \mu_H^b b - \omega(\ln(I_{L0}) - \mu_L^t t - \mu_L^b b) \quad (1.19)$$

$$0 = -\mu_H^b b + \omega \mu_L^b b \quad (1.20)$$

solving for  $\omega$  gives the same result as Eq(A.7) in the Appendix. Likewise, the same can be applied to calculate the theoretical weighting factor to cancel soft-tissue:

$$\ln(I_{DE}) = -\ln(I_{H0}) + \mu_H^t t + \mu_H^b b + \omega_b (\ln(I_{L0}) - \mu_L^t t - \mu_L^b b) \quad (1.21)$$

$$0 = \mu_H^t t - \omega_b \mu_L^t t \quad (1.22)$$

Which gives the same expression for  $\omega_b$  as Eq(A.40) in the Appendix.

Although this technique is very simple and straight-forward, there are some drawbacks. The weighting factors used in the subtraction are constant across the entire image. This may lead to an incomplete suppression of the specific tissue for different thicknesses across the image. This is largely caused by beam hardening effects, where the LE and HE beams experience different attenuation in regions of non-uniform tissue thicknesses. This means that one weighting factor value that can fully cancel the tissue of a specific thickness in one pixel, will not be able to cancel the tissue of a different thickness in another pixel. It is important to note that the derivation of weighting factor here is different than those in the Appendix.

#### 1.4.2. Decomposition of Basis Materials

The idea of image decomposition was first proposed by Alvarez *et al* in 1976, where attenuation coefficients were decomposed into Compton scatter and photoelectric constituents.<sup>14</sup> This technique has been used to identify the density and atomic make up of several different compounds. This is achieved via a basis material decomposition in the projection domain (before CT reconstruction) while also generating a linear combination of density maps of these materials in the image domain (after CT reconstruction). When decomposing into Compton scatter and photoelectric components, two basis materials are used where one has a low  $Z$  to approximate the Compton scatter,

and the other has a high  $Z$  for the photoelectric part. A study by Li *et al* used acrylic and aluminum as their low  $Z$  and high  $Z$  materials to replicate what would be a similar response from soft-tissue and bone.<sup>15</sup> Due to differences in attenuation between basis materials A and B, Beer's Law for LE and HE monoenergetic projections (as per **Figure A.1** from the Appendix) are manipulated and written as linear combinations:<sup>15</sup>

$$\ln\left(\frac{I_L}{I_{L0}}\right) = -\mu_L^A t_A - \mu_L^B t_B \quad (1.23)$$

$$\ln\left(\frac{I_H}{I_{H0}}\right) = -\mu_H^A t_A - \mu_H^B t_B \quad (1.24)$$

where the thicknesses  $t_A$  and  $t_B$  can be calculated via a matrix inversion:<sup>15</sup>

$$\begin{bmatrix} t_A \\ t_B \end{bmatrix} = \begin{bmatrix} \mu_L^A & \mu_L^B \\ \mu_H^A & \mu_H^B \end{bmatrix}^{-1} \begin{bmatrix} \ln\left(\frac{I_L}{I_{L0}}\right) \\ \ln\left(\frac{I_H}{I_{H0}}\right) \end{bmatrix} \quad (1.25)$$

However, x-ray measurements are acquired from polyenergetic spectra. For realistic LE and HE polyenergetic case  $S_L(E)$  and  $S_H(E)$ , Beer's Law is now written as:<sup>15</sup>

$$\ln\left(\frac{I_L}{I_{L0}}\right) = \int S_L(E) [-\mu_A t_A - \mu_B t_B] dE \quad (1.26)$$

$$\ln\left(\frac{I_H}{I_{H0}}\right) = \int S_H(E) [-\mu_A t_A - \mu_B t_B] dE \quad (1.27)$$

Unfortunately, this makes it more difficult to isolate and solve for  $t_A$  and  $t_B$  analytically.

An approximate solution was developed by Cardinal *et al* which involves a calibration of experimentally determined decomposition parameters.<sup>16</sup> Calibration is carried out using a

step phantom with known thicknesses of the two basis materials overlapped orthogonally.

Decomposition parameters are acquired on a pixel-by-pixel basis, therefore the

thicknesses  $t_A$  and  $t_B$  are calculated for each pixel, producing a pair of basis material

decomposed projections. Once the equivalent thickness of basis materials A and B are



calculated, they can be used as pixel-based weighting factors to generate virtual monoenergetic projections as follows:

$$\int \mu(E)ds = \mu_A t_A + \mu_B t_B \quad (1.28)$$

which represents the radiological path length for a monoenergetic energy E of a given pixel.

In principle, the benefits of applying the decomposition technique are the removal of beam hardening artifacts caused by metal implants, photon starvation, and other spectral effects.<sup>15,17</sup> A drawback of this technique is the need to determine numerous decomposition parameters for realistic polyenergetic LE and HE beams in order to calculate equivalent thicknesses.

### 1.4.3. Single Exposure DE

Single Exposure DE imaging is achieved by irradiating two detector plates at the same time with a single energy.<sup>12,18</sup> The x-ray beam interacts with the first detector plate, producing an LE image. Between the two phosphor plates is a copper filter, which hardens the beam by filtering low energy photons. Therefore, the hardened beam interacts with the second detector plate, producing the HE image as in **Figure 1.8**.

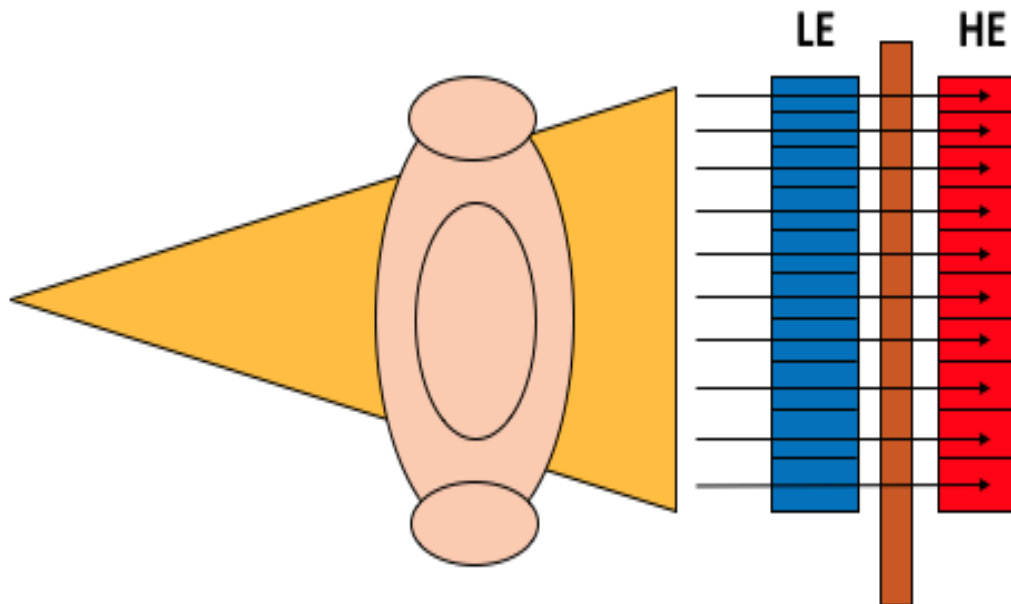


**Figure 1.8:** A single exposure DE acquires both LE and HE images via a copper filter.

This technique may then employ the SLS algorithm to generate the actual DE image. The advantage of the single exposure technique is the acquisition of both LE and HE images simultaneously thus effectively removing patient motion artifacts between two acquisitions. The major drawback of this technique is that the images generally have a low SNR.<sup>19</sup> The reduction in SNR is caused by the HE image, where the first phosphor plate and copper plate attenuated some of the photons, thus causing a reduction in signal and an increase in noise. Another drawback is the limited energy spectra separation. Unlike the double exposure technique (below), the spectral separation between LE and HE is achieved only by the copper filter and not by using two low and high kVps. Single exposure DE images may be improved via a noise reduction algorithm, or signal

amplification of the HE image. In general, single exposure DE images are used as complementary information with the SE images for diagnostic purposes.

#### **1.4.4. Double Exposure DE**

Double exposure techniques are those which involve the sequential acquisition of LE and HE images at low and high energies, e.g. 60 kVp and 120 kVp.<sup>19</sup> While, two separate kVps causes good spectral separation, filters for HE (and sometimes even for LE) may be used to further separate the energy spectra. Double exposure techniques have been reported to have an improved SNR compared to single exposure techniques. One of the main drawbacks to this technique is the possibility of misregistration artifacts in the DE images due to patient motion. Generally, there is a very short acquisition time between LE and HE images (~150 – 200 ms). However, in some cases such as cardiac motion, this is still enough time for variations in patient motion to cause misalignments.<sup>20</sup> These motion artifacts are commonly seen as black and white streaks caused by anatomical structure misalignment. The degree of patient motion can be crucial and may lead to an improper detection of calcified nodules.<sup>21</sup>

#### **1.4.5. Single Source DE**

The single source DE technique is used in DE applications of both radiography and computed tomography (CT). A single x-ray source quickly alternates kVps between a LE and HE setting. For DE-CT this is achieved during a single gantry rotation. However,

this means that the mAs has to remain constant throughout the scans.<sup>22</sup> Due to differences in exposure output between the LE and HE, more exposure time is given to the LE in order to enhance CNR. Single source DE imaging with CT has been reported to have good temporal registration between the LE and HE images. The limitation of this technique are potential spectral overlaps as well as the inability to modify the tube parameters of the LE and HE beams separately.<sup>22</sup> Compared to the double source DE method (below), the single source tends to have a reduced temporal coherence and lower dose efficiency.<sup>23</sup>

#### **1.4.6. Double Source DE**

Double source DE has been implemented in DE-CT imaging. The double source scanner has two detector arrays that interact with the two x-ray sources which are offset from each other by 90° as in **Figure 1.9**. These detectors acquire sets of LE and HE images at the same time. The benefit of having more than one x-ray source is more mAs and beam filtration optimization to achieve a better quality image.<sup>22</sup>

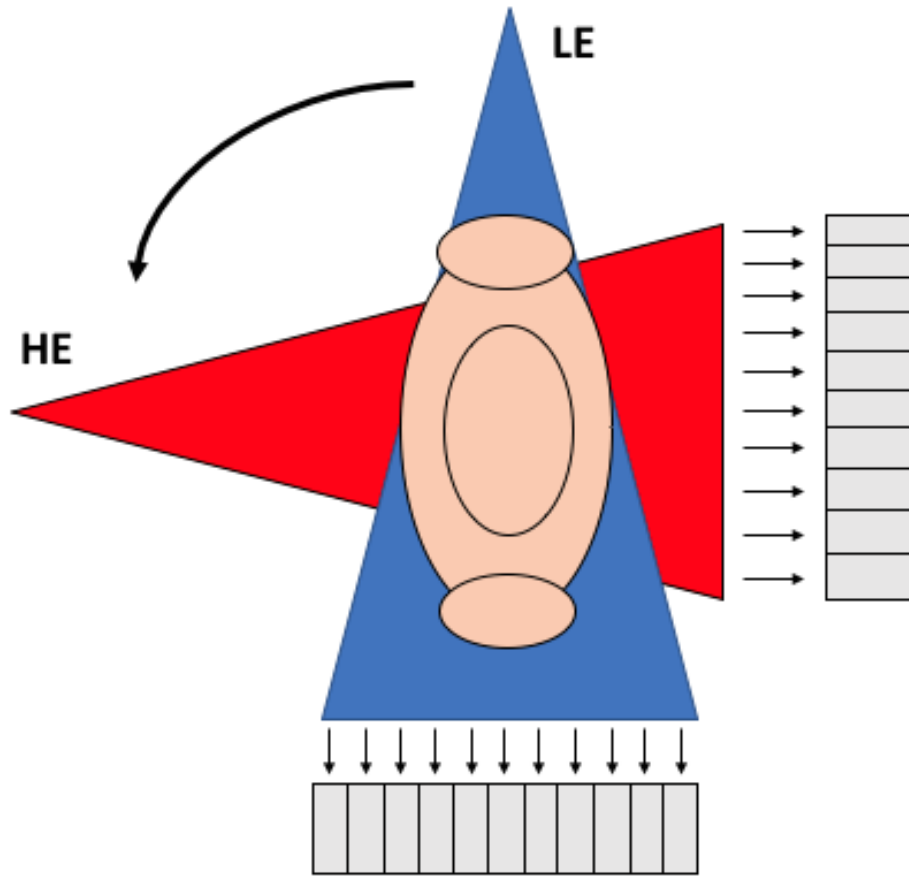


**Figure 1.9:** A double source DE system in CT acquires LE and HE images that are orthogonal to each other.

A limitation to this technique is that the projection data acquired is in a double-helix geometry, where the two source trajectories are out of phase by  $90^\circ$ . This means that the projections for the LE image and HE image do not coincide, thus causing difficulties in DE generation in the image domain.<sup>24</sup> Additionally there can be cross-scatter radiation between the two detectors which needs to be corrected for.<sup>25</sup>

### 1.4.7. Noise Reduction Algorithms

Although DE is an excellent technique in removing anatomical noise and improving lesion visualization, it has a drawback in terms of noise amplification. The common SLS technique tends to amplify quantum noise in the generated DE image.<sup>26</sup> This is caused by noise propagation in the logarithmic subtraction, which makes the noise more exaggerated. To reduce the noise in the resultant DE image, different noise reduction algorithms have been developed to improve image quality.

The simple smoothing of the high energy image (SSH) is a linear algorithm which applies a low-pass filter (LPF) to the HE image since it is the main contributor of quantum noise.<sup>27</sup> The HE image contributes more quantum noise because it requires fewer quanta to interact with the detector to produce a sufficient signal. Therefore, based on Poisson statistics for noise, there are less photons interacting in the HE image, and thus more noise. This is supported by **Figure 1.5**, where for higher energies, less x-rays interact with the detector, but a sufficient amount of energy is still able to be absorbed and converted into signal. The application of the LPF to the HE image modifies the SLS equation to:<sup>26</sup>

$$\ln(I_{SSH}) = h_{LPF} * \ln(I_H) - \omega_t \ln(I_L) \quad (1.29)$$

where  $h_{LPF}$  is the low-pass filter which is convolved with the logarithm of the HE image.

Another technique used to minimize the amount of noise in the DE image is the use of an anti-correlated noise reduction (ACNR) algorithm.<sup>28-30</sup> **Figure 1.10** is a flow chart of the ACNR algorithm.

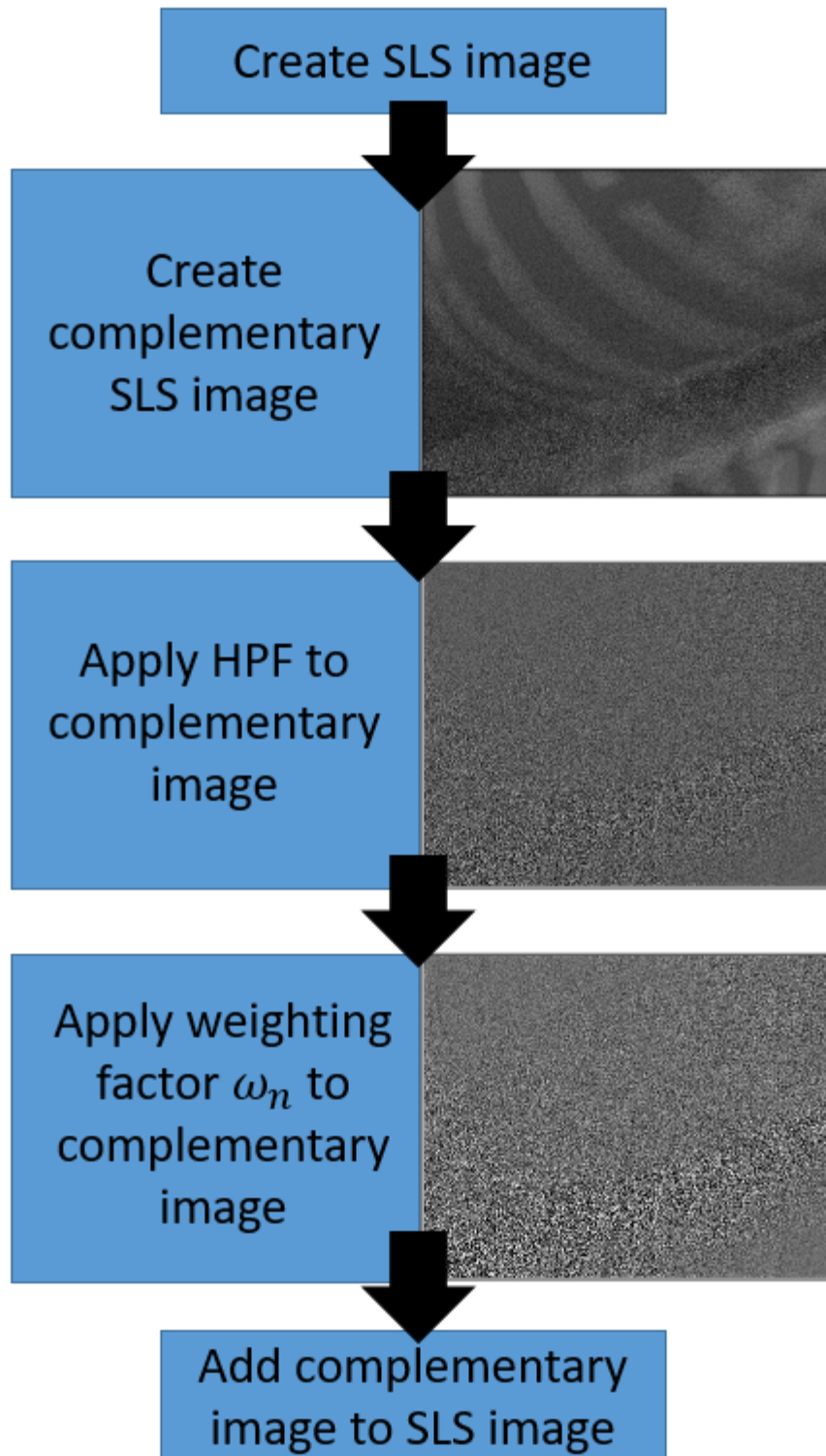


**Figure 1.10:** Flowchart for the ACNR algorithm.

This technique exploits the fact that the quantum noise in the soft-tissue-only and bone-only images are anti-correlated.<sup>26</sup> The ACNR algorithm applies a high-pass filter (HPF) to the complementary DE image. The complementary image to the soft-tissue-only image would be the bone-only image and vice versa. The HPF suppresses all of the low frequency information (i.e. anatomical structures) in the complementary image, leaving only quantum noise and some residual edge artifacts. This filtered complementary noise image is added to the DE image by applying a separate weighting factor  $\omega_n$ .<sup>26</sup>

$$I_{ACNR} = \omega_n [h_{HPF} * I_{DE}^C] + I_{DE} \quad (1.30)$$

where  $h_{HPF}$  is the high-pass filter, and  $I_{DE}^C$  is the complementary DE image. Adding noise of the complimentary image to the DE image effectively reduces noise since noise is anti-correlated. A comparison between a DE image without noise correction and with correction is illustrated in **Figure 1.11**.

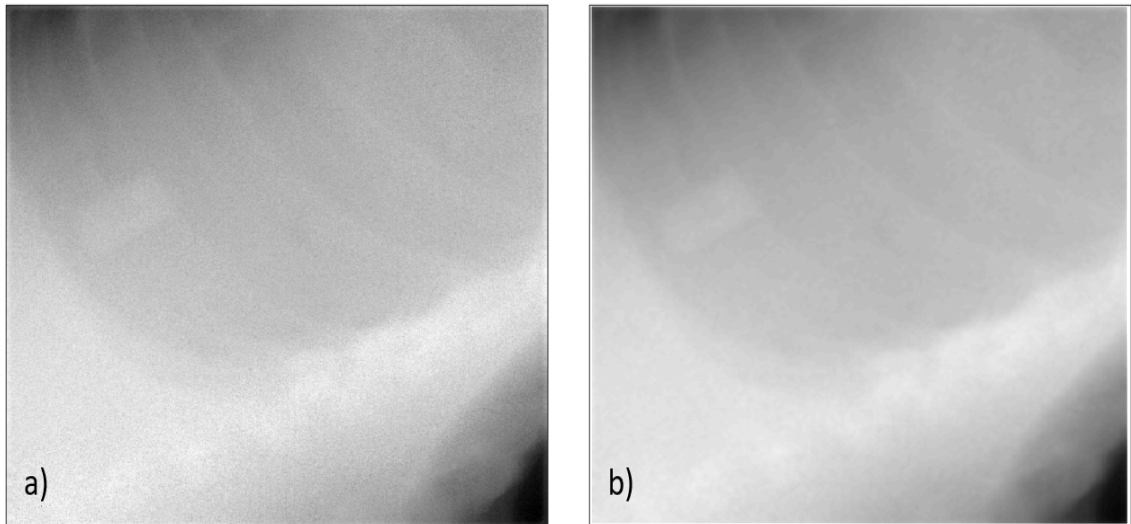


**Figure 1.11:** A DE image without any noise reduction applied (a). The same DE image after an ACNR algorithm has been applied (b).



## 1.5. Radiotherapy

Radiation therapy (RT) uses MV photons produced by a linear accelerator (linac) to treat malignancies by killing cancer cells. The goal when treating cancers with radiation is to achieve a uniform dose within the target volume, but minimize irradiating other healthy tissues. In particular, stereotactic body radiation therapy (SBRT) aims to deliver a hypofractionated high radiation dose precisely to the tumor volume while sparing adjacent organs at risk. A typical lung SBRT fractionation scheme is 12 Gy in 4 fractions, giving a total dose of 48 Gy. SBRT has shown to have good success in controlling metastatic lung and spinal tumors.<sup>31,32</sup> The success of SBRT critically depends on precise delivery by relying heavily on accurate image guided radiation therapy (IGRT). IGRT is essential to position the patient as accurately as possible such that radiation can be aimed exactly to the tumor. Using the in-room imaging systems, images are acquired and planning CT images are used as a reference for patient alignment. Cone-beam CT (CBCT) is often used as it provides volumetric images. However, projection x-ray images have the advantage of fast acquisition and lower imaging dose. Typical CBCT doses are around 20 mGy, whereas ExacTrac doses are closer to 0.52 mGy.<sup>33,34</sup> To align the patient, the projection images are aligned with digitally reconstructed radiographs (DRR) obtained from planning CT data sets. As DRR generation is an important part of this thesis, in the next section I describe the details of a DRR algorithm.

### 1.5.1 Digitally Reconstructed Radiograph

A CT data set is 3 dimensional (3D) with no fixed source position, while projection x-ray images are 2D with an imaging source at a fixed position in the space. A DRR algorithm takes the CT 3D data and synthetically calculates the beam's eye view (BEV) image which is a representation of the 2D radiograph. DRRs are generated via ray tracing techniques from a source to a position on the detector, while passing through the patient CT data. The ray tracing sums the attenuation coefficients along the ray lines to create the BEV images.<sup>35</sup> In this thesis, the DRR algorithm is slightly modified to calculate the amount of thickness of a specific tissue type in the CT volume based on Hounsfield units (HU). Each tissue has a different HU due to differences in attenuation in the material. In order to calculate the thickness of a material, the tissues of interest can be separated into different volumetric masks based on segmenting their HU range.

Siddon's method offers a fast DRR algorithm and takes into account the exact length of the ray line within each CT voxel.<sup>36</sup> Rays are calculated based on the intersection with a voxel location  $(i,j,k)$  in a volume. For the CT array of voxels in the x-direction equally spaced by  $d_x$ , the  $i$ th parallel plane can be expressed as:

$$X_{plane}(i) = X_{plane}(1) + (i - 1)d_x \quad (i = 1, \dots, N_x) \quad (1.31)$$

where  $N_x$  is the total number of voxels in the x-direction. Similar equations can be written for the y and z axes. The ray from the starting point (x-ray source) to the end point (detector) may be represented as:

$$X(\alpha_x) = X_1 + \alpha_x(X_2 - X_1) \quad (1.32)$$

where  $\alpha_x$  is a parametric variable which describes the position along the ray line, where  $\alpha_{min}$  is equal to 0 at the starting point and  $\alpha_{max}$  is 1 at the end point. The parametric intersection of the ray line between two adjacent planes can be calculated as:

$$\alpha_x(i) = \frac{X_{plane(i)} - X_1}{X_2 - X_1} \quad (1.33)$$

Once all  $\alpha_x$  (and y and z) are calculated, the  $\alpha_{min}$  and  $\alpha_{max}$  terms are given their parametric values with:

$$\alpha_{min} = \max\{0, \min[\alpha_x(1), \alpha_x(N_x)], \min[\alpha_y(1), \alpha_y(N_y)], \min[\alpha_z(1), \alpha_z(N_z)]\} \quad (1.34)$$

$$\alpha_{max} = \min\{0, \max[\alpha_x(1), \alpha_x(N_x)], \max[\alpha_y(1), \alpha_y(N_y)], \max[\alpha_z(1), \alpha_z(N_z)]\} \quad (1.35)$$

In the case where  $\alpha_{max}$  is less than  $\alpha_{min}$ , there is no intersection of the ray line with the CT volume. However, when  $\alpha_{min}$  is less than  $\alpha_{max}$ , the number of the first intersected plane after the ray has entered the pixel and the number of the last intersected plane is calculated. For the case when  $X_1 < X_2$ , the indices of the first and last intersected planes  $i_{min}$  and  $i_{max}$  are calculated under the following conditions:<sup>37</sup>

$$\alpha_{min} = \alpha_x(1) \rightarrow i_{min} = 1 \quad (1.36)$$

$$\alpha_{min} \neq \alpha_x(1) \rightarrow i_{min} = \left\lceil \frac{X(\alpha_{min}) - X_{plane(1)}}{d_x} \right\rceil \quad (1.37)$$

$$\alpha_{max} = \alpha_x(N_x) \rightarrow i_{max} = N_x - 1 \quad (1.38)$$

$$\alpha_{max} \neq \alpha_x(N_x) \rightarrow i_{max} = \left\lfloor \frac{X(\alpha_{max}) - X_{plane(N_x)}}{d_x} \right\rfloor \quad (1.39)$$

When  $X_1 > X_2$ , the following are used instead:<sup>37</sup>

$$\alpha_{min} = \alpha_x(1) \rightarrow i_{max} = N_x - 2 \quad (1.40)$$

$$\alpha_{min} \neq \alpha_x(1) \rightarrow i_{max} = \left\lfloor \frac{X(\alpha_{min}) - X_{plane(1)}}{d_x} \right\rfloor \quad (1.41)$$

$$\alpha_{max} = \alpha_x(N_x) \rightarrow i_{min} = 0 \quad (1.42)$$

$$\alpha_{max} \neq \alpha_x(N_x) \rightarrow i_{min} = \left\lceil \frac{X(\alpha_{max}) - X_{plane}(N_x)}{d_x} \right\rceil \quad (1.43)$$

For the range of indices ( $i_{min}, i_{max}$ ) the set of parametric values  $\{\alpha_x\}$  is calculated when  $X_1 < X_2$ :

$$\{\alpha_x\} = \{\alpha_x(i_{min}), \dots, \alpha_x(i_{max})\} \quad (1.44)$$

When  $X_1 > X_2$ , the following is used:

$$\{\alpha_x\} = \{\alpha_x(i_{max}), \dots, \alpha_x(i_{min})\} \quad (1.45)$$

Every term in this set of parametric values represents an intersection of the ray with a plane in the CT volume. The complete merged parametric sets for the x,y, and z planes is given as:

$$\{\alpha\} = \{\alpha_{min}, merge[\{\alpha_x\}, \{\alpha_y\}, \{\alpha_z\}], \alpha_{max}\} \quad (1.46)$$

Adjacent terms in  $\{\alpha\}$  indicate intersections in a voxel, denoted by  $m$  and  $m-1$ . Therefore, the entire length of the intersection through a given voxel is:

$$l(m) = d_{1,2}[\alpha(m) - \alpha(m-1)] \quad (m = 1, \dots, n) \quad (1.47)$$

where  $d_{1,2}$  is the Euclidian distance from the source to the detector. The CT voxel index  $[i(m), j(m), k(m)]$  which contains the midpoint of the intersections is found with:

$$i(m) = 1 + [X_1 + \alpha_{mid}(X_2 - X_1) - X_{plane}(1)]/d_x \quad (1.48)$$

$$j(m) = 1 + [Y_1 + \alpha_{mid}(Y_2 - Y_1) - Y_{plane}(1)]/d_y \quad (1.49)$$

$$k(m) = 1 + [Z_1 + \alpha_{mid}(Z_2 - Z_1) - Z_{plane}(1)]/d_z \quad (1.50)$$

where

$$\alpha_{mid} = [\alpha(m) + \alpha(m-1)]/2 \quad (1.51)$$

Therefore, the total radiological pathlength through the 3D CT volume is calculated as:

$$d = \sum_{m=1}^{m=n} l(m)\rho(i(m),j(m),k(m)) \quad (1.52)$$

where  $\rho(i(m),j(m),k(m))$  is the specific voxel value. The Siddon's method for DRRs is typically used to calculate the total radiological pathlength by summing up a CT volume that has been converted into linear attenuation values for  $\rho$ . However, in this thesis the actual thickness of the CT volume itself is calculated by dividing the pathlength by  $\rho$ . This is used to determine the total thickness of a specific tissue type along the ray line within the CT volume.

The CT pixels are in HU values which are different for different tissue types allowing HU based segmentation before calculating total thickness in the DRR. Some tissue types such as soft-tissue and lung have a similar atomic number and mass attenuation coefficient, thus density scaling can be used to convert total radiological thickness for those tissues. The linear attenuation coefficient for Compton interactions depends on density, while the photoelectric interaction depends on both density and atomic number. This means that density scaling can be used on tissues that only differ in density given that their effective atomic numbers are very similar. For different bones however, density scaling may not be sufficiently accurate to yield a particular equivalent bone thickness. **Table 1.2** lists some physical parameters for different tissue types in the body<sup>38,39</sup>

**Table 1.2:** Effective atomic number, density, and Hounsfield Units for different tissue types.

| Tissue          | Effective atomic number | Density (g/cm <sup>3</sup> ) | Hounsfield Unit (HU) |
|-----------------|-------------------------|------------------------------|----------------------|
| Cortical bone   | 13.63                   | 1.780                        | 1094.6               |
| Rib bone        | 12.32                   | 1.441                        | 610.6                |
| Trabecular bone | 10.23                   | 1.150                        | 207.6                |
| Lung (inhaled)  | 7.60                    | 0.258                        | -741.8               |
| Soft-tissue     | 7.40                    | 1.06                         | 100                  |
| Water           | 7.42                    | 1.00                         | 0                    |

### 1.6. Applications of Dual-energy Imaging in Radiotherapy

Dual energy has grown in popularity for diagnostic imaging purposes but have also recently applied to enhance imaging for IGRT applications. Dual-energy CT (DECT) is namely used to enhance the quality of images used for RT patients. This was performed by improving tumor delineation and characterization, normal tissue characterization, and improved target tracking.<sup>40</sup> For tumor delineation and characterization, virtually monoenergetic CT reconstructions can be created and used to improve the subjective image quality. Additionally, the use of monoenergetic CT

reconstructions can be used to create spectral Hounsfield Unit curves to show the differentiation between malignant and benign tumors.<sup>41,42</sup>

Normal tissue characterization is investigated by imaging the perfusion of lung parenchyma. The material decomposition imaging of a contrast agent such as iodine, administered to the lungs can provide information on the pathology. Additionally, other contrast media such as xenon and krypton may be used to investigate the ventilated regions of the lungs.<sup>43,44</sup> The benefits of using DECT for these purposes could allow for an improved quantitative evaluation of normal tissue for predictions on the treatment outcomes and tissue toxicity.<sup>45</sup> Improved target tracking can be made possible by acquiring sequential DE planar x-ray images to enhance tumor visualization.<sup>46</sup> Markerless tumor tracking via DE fluoroscopy has been investigated and demonstrated improved results in tracking compared to using SE imaging.<sup>47</sup>

Besides diagnostic improvements for RT patients, studies were performed on updating dose calculations using DECT for brachytherapy and photon therapy. Dose calculations for low energy brachytherapy require both Compton scatter and photoelectric information which can be used to estimate the electron density and atomic number of specific tissues. Monte Carlo simulations require photon attenuation coefficients which can be obtained using a decomposition technique.<sup>48</sup> Using DECT to extract electron densities and effective atomic numbers from attenuation coefficients has shown an improvement in tissue characterization compared to using single-energy CT (SECT). Monte Carlo dose calculations using virtual phantoms with DECT were within 4% of the ground truth for <sup>103</sup>Pd.<sup>49</sup> A study by Malusek *et al* was able to estimate accurate mass

attenuation and mass energy absorption coefficients by decomposing abdominal soft-tissue into lipid, protein, and water.<sup>50</sup>

DE applications involving photon therapies stem from improving the HU to electron density calibrations. Using a linear combination of LE and HE images gives a better estimate of the electron density since Compton scattering and photoelectric information is available. Using DECT over SECT improved electron density estimation for treatment planning, reducing the dose uncertainty from 11% to 1%.<sup>51</sup>

## **1.7. Thesis Outline**

DE imaging has shown to be a versatile technique in both diagnostic imaging and RT. The common method used is the SLS technique, however it often suffers from incomplete bone cancellation due to beam hardening effects. The decomposition method inherently calibrates for beam hardening effects but requires many calibration parameters to be calculated. In addition, the theoretical expressions for the tissue cancelling weighting factor has been explored for simplistic monoenergetic LE and HE beams. Other imaging factors such as scatter, polyenergetic spectra, and detector response have not been considered.

This thesis has two objectives. The first is to develop a novel DE algorithm which is able to overcome the limitations of the conventional DE method by determining pixel specific weighting factors based on soft-tissue and bone thickness. The second objective is to incorporate imaging parameters into the DE theory and theoretically derive



analytical expressions of the weighting factors describing the effects of various imaging parameters and validating these expressions by measurement.

The next chapter in this thesis is the manuscript submitted to the Medical Physics journal which describes the development of the novel algorithm and the experimental verification of the modified weighting factors. The third chapter concludes the achievements of the thesis and discusses multiple future research avenues which may be incorporated into improving the algorithm. The Appendix at the end of the thesis discusses step by step analytic derivations of the modified weighting factor incorporating various imaging parameters.

## **Chapter 2: “Patient specific pixel-based weighting factor dual-energy x-ray imaging system”**

*The content of this chapter is based on the following manuscript submitted to the journal of Medical Physics: “Patient specific pixel-based weighting factor dual-energy x-ray imaging system”, Michael C. Reno, Sahar Darvish-Molla, Mike Sattarivand.*

### **2.1. Abstract**

**Purpose:** To develop a novel patient specific pixel-based weighting factor dual-energy (PP-DE) algorithm to effectively suppress bone throughout the image and overcome the limitation of the conventional DE algorithm with constant weighting factor which is restricted to regions with uniform patient thickness. Additionally, to derive theoretical expressions to describe the dependence of the weighting factors on several imaging parameters and validate them with measurement.

**Methods:** A step phantom was constructed consisting of slabs of solid water and bone materials. Thicknesses of bone ranged [0-6] cm in one direction, and solid water [5-30] cm in the other direction. Projection images at 60 and 140 kVp were acquired using a clinical imaging system. Optimal weighting factors were found in the range [0.6-1.4], where bone and soft-tissue contrast-to-noise ratio (CNR) reached zero. Bone and soft-tissue digitally reconstructed radiographs (DRRs) were created using computed tomography images of a Rando phantom and ray tracing techniques. A weighting factor

image was calculated using DRRs and pre-calculated weighting factors from the step phantom. The weighting factor image was used to generate a PP-DE image. The PP-DE image was compared to the conventional DE image which uses a constant weighting factor throughout the image. The signal-to-noise ratios (SNR) were calculated in the step phantom for the PP-DE image and compared to that of conventional DE technique. Analytical expressions for theoretical weighting factors were derived which included various effects such as beam hardening, scatter, and detector response. The analytical expressions were simulated in Spektr3.0 for the same bone and solid water thicknesses as the step phantom. A tray of steel pins was constructed and used with the step phantom to remove the scattered radiation. The simulated theoretical weighting factors were compared to those from the step phantom measurement.

**Results:** Optimal weighting factor values for the step phantom varied from 0.633 to 1.355 depending on region thickness. Thicker regions required larger weighting factors for bone cancellation. The PP-DE image of the Rando phantom favorably cancelled both ribs and spine, whereas in the conventional DE image, only one could be cancelled at a time. The SNRs for the PP-DE image was larger than those of the conventional DE images for regions which required smaller weighting factors for bone suppression. Comparisons of measured and simulated weighting factors demonstrated a 3% agreement for all bone overlapped regions except for the thickest region with 30 cm of solid water overlapped with 6 cm bone where the signal was lost due to excess attenuation.

**Conclusions:** A novel PP-DE algorithm was developed which can create higher quality DE images with enhanced bone cancellation and improved noise characteristics compared to conventional DE technique. In addition, theoretical weighting factor expressions were derived and validated against measurement.

## 2.2. Introduction

The significance of medical x-ray imaging has surpassed diagnostic applications, and today is in widespread use in radiation therapy treatments. Image guided radiation therapy (IGRT) utilizes a linac mounted kV imaging system (to create planar or volumetric images) or in-room mounted x-ray imaging (to create planar images) which may be incorporated in proper patient alignment.<sup>52</sup> Cone-beam computed tomography (CBCT) is often used as it provides volumetric images.<sup>53-55</sup> Nevertheless, planar projection imaging may be more suitable in some applications due to its faster acquisition and processing time with lower imaging dose.<sup>56,57</sup> However, one major drawback of planar imaging is the presence of anatomical noise due to projection overlap. For instance, for lung stereotactic body radiation therapy (SBRT) patients, the overlap of bony anatomy such as ribs may obscure the detection of lung tumors, making the impact of tumor localization more complicated. Dual-energy (DE) imaging can overcome this limitation by producing soft-tissue-only (or bone-only) images. DE has been an established technique in diagnostic imaging.<sup>13,21,58,59</sup> However, its applications in IGRT has only recently been evaluated for different imaging systems.<sup>33,46,60,61</sup>

DE technique requires acquisition of low energy (LE) and high energy (HE) images. Two different conventional DE algorithms have been used in combining the LE and HE images to suppress a specific tissue type. The first algorithm category is the decomposition method, where the HE and LE are decomposed into equivalent thicknesses of two basic materials mimicking bone and soft-tissue (e.g. aluminum and Lucite).<sup>14,15,17,24</sup> The attenuation coefficient is presented as a weighted sum of non-linear basic functions, where weighting factors are pixel-based (i.e. vary across the image) and represent equivalent thickness of basic materials. This method requires calibration of the imaging system with the LE and HE beams using step phantoms with known thicknesses of both basic materials. Since clinical polyenergetic LE and HE beams are used for calibration, in principle the calibration process corrects for beam hardening effects on a pixel-by-pixel basis.<sup>15</sup>

The second DE algorithm category is the logarithmic subtraction method. In this technique, the LE and HE images are log-subtracted after applying a weighting factor across the LE image.<sup>47,62,63</sup> The soft-tissue-only image,  $I_{DE}$ , is created using:

$$\ln(I_{DE}) = \ln(I_{HE}) - \omega \ln(I_{LE}) \quad (2.1)$$

where  $I_{LE}$  and  $I_{HE}$  are the corresponding images of the LE and HE beams respectively. The weighting factor  $\omega$  is typically constant across the image for given LE and HE beams. However, using a uniform weighting factor does not lead to a complete bone cancellation in all regions of the image. This is caused mainly by beam hardening effects which varies in different regions with various patient thicknesses.<sup>63</sup> Due to the polyenergetic nature of the beams, beam hardening changes the effective attenuation

coefficient of a material depending on the thickness, where thicker materials have a lower attenuation, while the opposite is true for thinner materials.<sup>64</sup> A study by Ho *et al* reported that beam hardening effects influenced their DE images, but did not provide any means of quantification.<sup>65</sup>

The development of a DE algorithm that can incorporate the simplicity of the conventional subtraction technique while using calibration to correct for beam hardening effects as per the equivalent thickness method is desirable. This approach could generate soft-tissue selective images with enhanced bone suppression throughout the image by assigning patient specific pixel-based (PP) weighting factors depending on the thickness of bone and soft-tissue. Applying this hybrid technique may offer benefits in particular for radiation therapy applications, where the patient's previous computed tomography (CT) images are acquired for treatment planning purposes in the same patient geometry as the x-ray acquisitions. These CT images can be used as *a-priori* information to calculate patient's bone and soft-tissue thickness along the ray lines of each pixel in the projection image. The *a-priori* information may then be used to assign the optimal weighting factor to fully suppress bone or soft-tissue in that specific pixel location. In the case of a soft-tissue selective image, this would mean the full cancellation of both ribs and spine in a chest radiograph.

The weighting factor in the subtraction method plays a critical role in determining the success of DE imaging in terms of both tissue cancelation and noise propagation. Some previous studies used  $\omega = \mu_H^b / \mu_L^b$  to create soft-tissue-only image, where  $\mu_H^b$  and  $\mu_L^b$  are bone linear attenuation coefficients for HE and LE respectively.<sup>10,27,47,62</sup> However, this equation is only valid for monoenergetic beams and does not include polyenergetic

beam hardening effects and thus effective  $\mu$  values may be used as an approximation. Some other studies empirically determined the weighting factors which may only apply to a particular patient thickness for given LE and HE beams.<sup>26,33,46,60,61</sup> Deriving analytic expressions for weighting factors could be challenging when considering realistic parameters such as polyenergetic spectra, beam hardening, scatter, and detector response. Hoggarth *et al*<sup>60</sup> reported a linear trend weighting factor change with mAs but did not describe the underlying theory. Xu *et al*<sup>47</sup> discussed the practical need to use effective  $\mu$  values for polyenergetic beams and stated that it's nearly impossible to calculate the exact effective attenuation coefficient and weighting factor analytically, therefore no theoretical results were reported. Additionally, there have been no previous studies that have considered the effects of patient scatter, detector gain, and detector response. To our best knowledge, no previous study quantitatively evaluated various parameters that affect weighting factors nor established theoretical expressions describing these effects.

The objective of this study is twofold. The first aim is to develop a PP-DE algorithm that can effectively suppress a specific tissue type throughout the image with non-uniform patient thickness and overcome the limitation of the conventional DE algorithm with a constant weighting factor. Second, this work seeks to derive and validate theoretical expressions for weighting factors which include various imaging parameters such as beam hardening, scatter, and detector response.

## 2.3. Materials and Methods

### 2.3.A. Theoretical Simulations

Simulation was performed to investigate how weighting factor changes due to the inclusion of different imaging parameters based on the expressions derived in the Appendix. Spektr Ver 3.0 toolkit was used to generate the spectra and simulate its changes when passing through different materials used in the step phantom experiment (see section 2.3.B1).<sup>2</sup> Spektr has been reported to be in excellent agreement with measured spectra for tube potentials in the range 30 to 140 kVp.<sup>66</sup> The LE and HE tube potentials used in the simulation (*and* experiments) were 60 and 140 kVp respectively, which were based on previously published optimized values for the ExacTrac system (Brainlab AG, Germany).<sup>33</sup> All simulations were performed by developing in-house codes in Matlab (MathWorks, Natick, MA).

#### 2.3.A1. Monoenergetic Case

The theoretical weighting factor to cancel bone for a monoenergetic beam was calculated using Eq.(A.7) in the Appendix. Both LE and HE peak voltages (60, 140 kVp) were divided by 1.5 to get an effective monoenergetic energy of 40 and 93 keV respectively. For these energies, the corresponding bone linear attenuation coefficients are  $0.79 \text{ cm}^{-1}$  and  $0.29 \text{ cm}^{-1}$  respectively. These values are obtained by interpolating (to



bin sizes of 1 keV) the vendor provided linear attenuation values (CIRS Inc, Norfolk, VA) for the average bone.

### **2.3.A2. Beam Hardening Effects**

X-ray spectra for both the LE and HE tube voltages (60, 140 kVp) were simulated using the tungsten anode spectral model using interpolating cubic splines (TASMICS) algorithm. TASMICS has been reported to provide a better energy resolution than its previous algorithm based on spectral model using interpolating polynomials (TASMIPS).<sup>2</sup> The ExacTrac tube inherent and added aluminum (Al) filtrations and treatment couch were simulated. The Spektr added Al filter was adjusted such that the Spektr calculated first half value layers (HVL) matched the narrow beam geometry measured HVLs for the full range of 60-140 kVp.<sup>33</sup> The total added filtration was 3.3 mm Al.

Once the LE and HE spectra were generated, first they passed through the ExacTrac treatment couch with 1.033 mm of equivalent Al.<sup>33,67</sup> . The spectra then passed through various bone and solid water (soft-tissue) thicknesses in the ranges of [0-6 cm] and [0-30 cm] respectively to mimic different regions in the step phantom. This was implemented using the average bone linear attenuations for the spectrum from section 2.3.A1 and generating a solid water compound based on the material composition provided by the vendor (GAMMEX, Middleton, WI). Vendor provided densities of 1.6 and 1.055 cm<sup>3</sup>/g for the bone and solid water respectively, were used to calculate linear attenuations in the Spektr code. The simulated thickness ranges are wider than the actual

step phantom geometry as they also extend to zero bone and soft-tissue thickness (soft-tissue thickness is from [0-30 cm] and bone is from [0-6 cm]). This effectively simulates beam hardening by changing the spectra that are needed in Eq.(A.9) in the Appendix since the spectra pass through various bone and soft-tissue thickness pairs. The hardened LE and HE spectra simulate incident spectra on the detector and were used to calculate spectrum weighted bone linear attenuation coefficients and theoretical weighting factors as per Eq.(A.9) and Eq.(A.11) in the Appendix.

### **2.3.A3. Scatter Effects**

In principle, scatter effects can be simulated using Eq.(A.16) in the Appendix. This requires a knowledge of scatter to primary ratio terms which depend on phantom (or patient) geometry. Spektr outputs only primary and does not simulate scatter. Thus, scatter was not simulated and instead it was measured and subtracted from the signal in the step phantom (see section 2.3.B2) before comparing simulation results to experimental data.

### **2.3.A4. Detector Effects**

The detector response was simulated to determine its effect on theoretical weighting factor as per Eq.(A.22) in the Appendix. ExacTrac uses an 8-inch PerkinElmer XRD flat panel detector (PerkinElmer Inc, Waltham, MA) which has a CsI scintillator with the vendor stated detective quantum efficiency (DQE) of 75% at 0 cycles/mm for

RQA5 beam. RQA5 is an IEC standard for the radiation quality of an x-ray beam with an added Al filter.<sup>68</sup> The IEC standard for RQA5 requires a tube voltage of 70 kVp and an HVL of 7.1 mm Al.<sup>69</sup> To estimate the thickness of CsI, first the RQA5 spectrum was simulated in Spektr. The added filtration was adjusted in Spektr to produce a spectrum with 7.1 mm Al HVL for 70 kVp tube voltage. With the simulated RQA5 spectrum, the quantum efficiency was calculated using:

$$DQE(0) = \alpha(E) = 1 - e^{-\mu_d(E)t_d} \quad (2.2)$$

where  $\mu_d(E)$  and  $t_d$  are linear attenuation coefficient and thickness of CsI respectively. The parameter  $t_d$  varied between 0 and 1 mm to obtain  $\overline{\alpha(E)} = 0.75$  and thus the CsI thickness was estimated to be 0.21 mm.

Using this CsI thickness, Eq.(2.2) was used again to calculate  $\alpha(t, b)$  for a thickness  $t$  of soft-tissue and  $b$  of bone in Eq.(A.22) for both LE and HE (60, 140 kVp) but with hardened beams for different bone and soft-tissue thickness pairs as per section 2.3.A2 above. The spectrum weighted linear attenuations for CsI were used as per Eq.(A.11). Similarly, the  $E(t, b)$  terms were calculated for LE and HE hardened beams using values from previous studies and matching to the spectrum effective energies.<sup>10,70</sup> Both  $\alpha(t, b)$  and  $E(t, b)$  were inserted into Eq.(A.22), and similar to section 2.3.A2, a theoretical weighting factor was calculated for each bone and soft-tissue thickness pairs in the range [0-6 cm] and [0-30 cm] respectively.

### **2.3.A5. Combination of Effects**

The combined effects of beam hardening and detector response were simulated using Eq.(A.35) in the Appendix. The scatter to primary ratio terms in this equation were set to zero for simulation as per section 2.3.A3 above.

### **2.3.B. Experimental Phantom Studies**

#### **2.3.B1. Weighting Factor Calibration Using Step Phantom**

A step phantom (**Figure 2.1a**) was constructed consisting of slabs of solid water Model 557-450 (GAMMEX, Middleton, WI) and average bone Model BN30-20-AB (CIRS Inc, Norfolk, VA) materials. Thicknesses of bone ranged from 0 to 6 cm in one direction, and solid water from 5 to 30 cm in the other direction. The slabs were stacked perpendicular to each other, creating a step-like pattern. The phantom was also designed to match the ExacTrac field of view (FOV) of 13 cm at isocenter. The step phantom was placed on the treatment couch, which was rotated 45° to face one of the ExacTrac x-ray tubes. Additionally, the step phantom was placed on a plastic stand angled at 42°, such that the central axis of the x-ray beam was perpendicular to the phantom surface (**Figures 2.1a, 2.1b**).

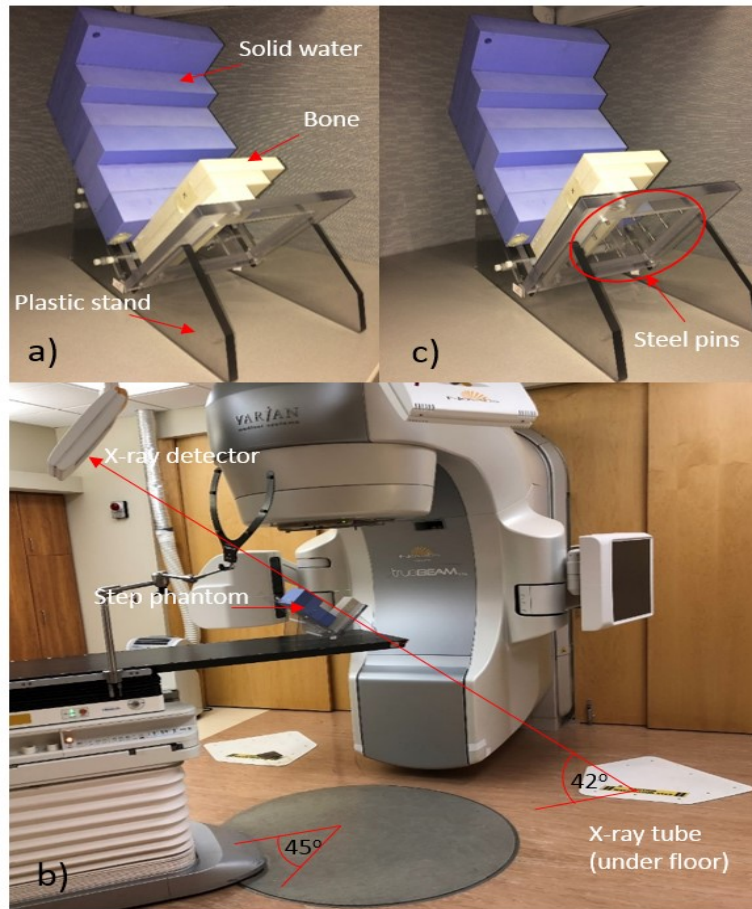


**Figure 2.1:** Step phantom with varying solid water and bone slabs placed on plastic stand (a). The phantom is placed on the treatment couch with the indicated geometries (b). The addition of a thin plastic plate with steel pins to the step phantom for scatter correction (c).

X-ray images were acquired for low and high tube voltages of 60 and 140 kVp. To avoid detector saturation, 4 low energy images (each with 9.9 mAs) and 12 high energy images (each with 0.99 mAs) were acquired and the images were summed up. The total mAs values (39.6 mAs for LE and 11.9 mAs for HE) were determined such that the surface dose from the dual energy image (combining LE and HE) does not exceed that of a clinical conventional single energy technique (525  $\mu$ Gy) acquired with a clinical

thorax protocol using 120 kVp and 25 mAs.<sup>33</sup> The dose allocation from the HE and LE x-ray images were 70% and 30% respectively.<sup>58,62</sup> Dark images were acquired by blocking the x-ray tube with lead and using a tube voltage of 40 kVp with 2.52 mAs. Flood images were also acquired by moving the treatment couch away from the beam path while using a tube voltage of 60 kVp with 12.68 mAs and 120 kVp with 0.63 mAs. The LE and HE images were corrected for dark and flood signals before calculating DE images.

The LE and HE images were exported from a clinical ExacTrac Ver. 6.0 workstation and read using an in-house Matlab program to create a DE image. X-ray images were analyzed by creating 16 regions of interests (ROIs) as per **Figure 2.2a**, to determine the best weighting factor for bone suppression.

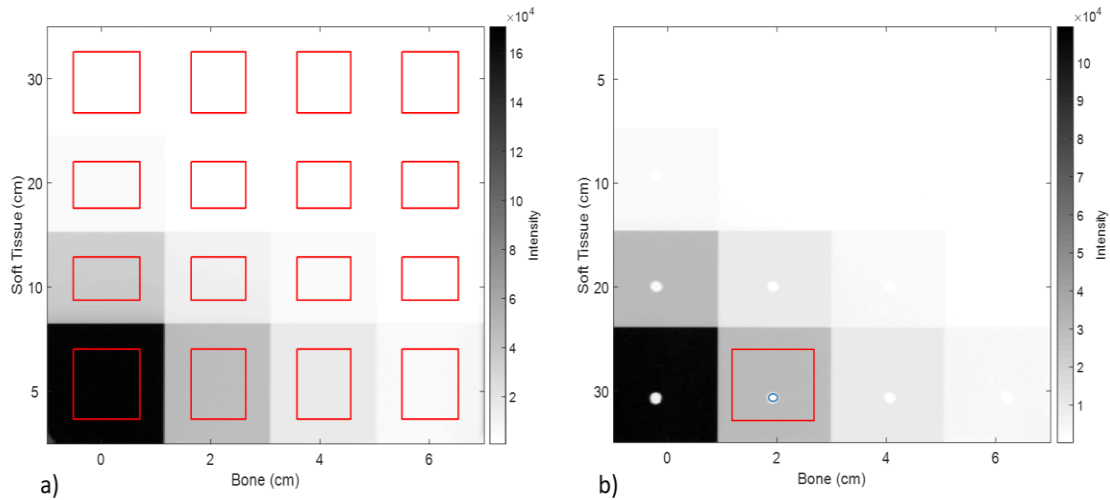


**Figure 2.2:** X-ray image of the step phantom at 60 kVp. ROIs are indicated by the red rectangles (a). Small circular ROIs in blue were made to estimate scatter under steel pins (b). ROI of only one region is illustrated for simplicity while similar ROIs utilized for other regions.

The optimal weighting factors for each ROI with bone overlap was determined by calculating the contrast-to-noise ratio (CNR) between a region with bone and soft-tissue and its corresponding soft-tissue only region. The CNR was calculated using:

$$CNR_{bst,st} = \frac{I_{bst} - I_{st}}{\sqrt{\frac{1}{2}(\sigma_{bst}^2 + \sigma_{st}^2)}} \quad (2.3)$$

where  $I_{bst}$  and  $I_{st}$  are the average intensities of the ROIs with bone and soft-tissue overlap and soft-tissue alone while  $\sigma_{bst}$  and  $\sigma_{st}$  are the corresponding standard deviations. DE subtraction was applied to the LE and HE images by iteratively varying the weighting factor values from 0.6 to 1.4 in steps of 0.001. The optimal weighting factor was determined for each bone overlapped ROI such that the CNR yielded a value as close to zero as possible. A value close to zero indicates that there is a very small difference in signal between the two ROIs, indicating bone cancellation. To reduce the noise in all DE images, an anti-correlated noise reduction (ACNR) algorithm was applied using parameters from Richard *et al.*<sup>26,28-30,60</sup> The experiment was repeated four times to calculate statistical uncertainties on measured weighting factors. The weighting factors for each bone overlapped ROI constitute pre-calibrated values for given bone and soft-tissue thickness pairs.

### 2.3.B2. Scatter Removal Experiment

A scatter removal technique was implemented similar to a previous study.<sup>15</sup> A thin plastic tray with steel pins was added to the step phantom (**Figure 2.1c**), with pins centered in each of the 16 ROIs. The length of each pin was 7 mm which is equivalent to

10 HVLs (at 140 keV) and is sufficient enough to effectively block all primary photons. ExacTrac images were acquired using the same parameters (kVp and mAs) as the previous experiment (section 2.3.B1). The images were analyzed to determine the scatter signal contribution to the overall signal for each 16 regions with a given bone and soft-tissue thickness pair. Small circular ROIs were created under each pin to calculate the average scatter signal as per **Figure 2.2b**. The 16 scatter values were then 2D interpolated via cubic spline into an image for both LE and HE images to calculate a scatter image across the phantom. To quantify the amount of scatter contribution to each ROI, scatter fractions (ratio of scatter to scatter plus primary) were calculated. This was performed by dividing the LE and HE scatter interpolated images by their corresponding x-ray images. The ROIs were then used to calculate the mean ratio of scatter to scatter plus primary in each region. To correct the x-ray images, the scatter image was then subtracted from the x-ray images to produce primary-only LE and HE images. Using primary-only LE and HE images, DE weighting factors were calculated for each bone overlap region similar to section 2.3.B1. Thus, the calculated weighting factors represent values for scatter corrected DE images. The experiment was repeated four times to obtain statistical uncertainty on measured weighting factors.

### **2.3.B3. Rando Phantom Experiments**

An adult female Rando ATOM phantom (CIRS Inc, Norfolk, VA) was used with a cylindrical solid-water plug (14 mm diameter, 25 mm long) inserted in her lung tissue to mimic a lung tumor (**Figure 2.3**). Plastic radiopaque markers (BB) were placed on the



phantom surface to indicate the location of the tumor and guide the alignment with the CT and ExacTrac in-room lasers. The phantom was imaged both with a clinical CT simulator scanner and the ExacTrac imaging system. The CT images of the Rando phantom were acquired using the clinical chest imaging protocol of 120 kVp and 250 mA. The ExacTrac images of the Rando were acquired using the same techniques (kVp and mAs) as per the step phantom experiment (section 2.3.B1).



**Figure 2.3:** Rando phantom with a cylindrical solid water plug (red arrow) to simulate a lung tumor.

#### **2.3.B4. PP-DE Algorithm Development**

The steps of the PP-DE algorithm are outlined in the flowchart in **Figure 2.4**. Note that the first part in finding the pre-calculated weighting factors is implemented as per section 2.3.B1.

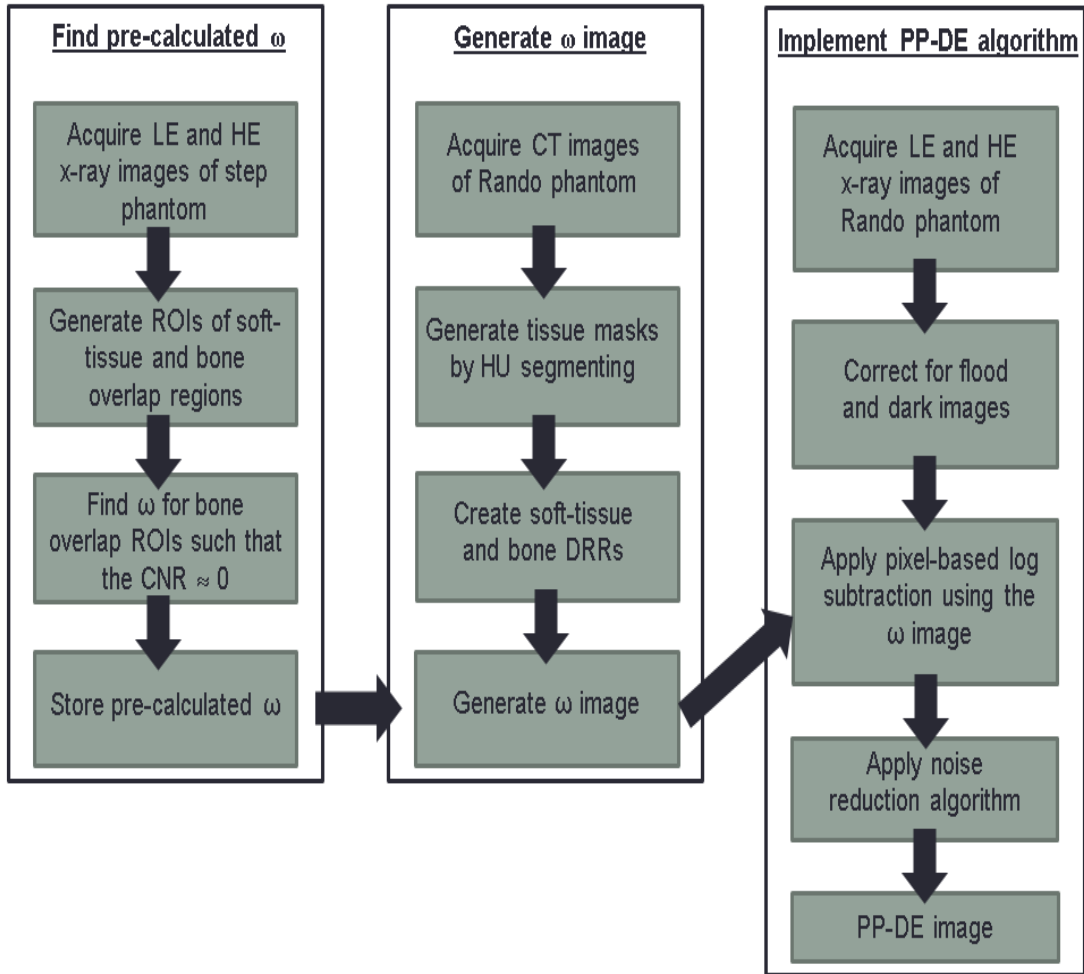


**Figure 2.4:** Flowchart illustrating the steps of PP-DE algorithm.

The pre-calculated weighting factors were used to generate a  $\omega$  image using a-priori CT data. The CT images of the Rando phantom were exported in Digital Imaging and Communications in Medicine (DICOM) format and read into an in-house Matlab program. The images were segmented into air, lung, soft-tissue, and bone using Hounsfield Unit (HU) values for each voxel. The segmentation threshold ranges were

pixels less than -840 HU for air, [-840 to -650] HU for lung, [-650 to 250] HU for soft-tissue, and pixels greater than 250 HU for bone. The segmented volumes were used to create separate mask images for each tissue type. For each tissue type, digitally reconstructed radiographs (DRRs) were calculated to create beam's eye view (BEV) images seen from each ExacTrac x-ray source. The ExacTrac x-ray source and flat panel detector geometry were modeled to account for the azimuth ( $45^\circ$ ) and elevation ( $42^\circ$ ) x-ray tube angles (**Figure 2.1b**). The source to isocenter distance ( $\approx 217$  cm) and source to detector distance ( $\approx 340$  cm) were modeled to ensure the correct FOV at isocenter ( $\approx 13$  cm) and at detector surface ( $\approx 20.3$  cm). Virtual rays were modeled as 3D vectors to connect the source point on the x-ray tube to each (512x512) pixel on the ExacTrac detector plane. DRRs were created by ray tracing through each tissue type volume using Siddon's method that accounts for ray length within each CT voxel<sup>36</sup>. The total length of each ray is the overall tissue thickness; thus the DRR image is a map of tissue thickness for a given tissue type. The lung thickness DRR was scaled by a density ratio between lung and soft-tissue to convert lung thickness to its equivalent soft-tissue thickness. Thus, two separate DRRs were generated, one for total soft-tissue thickness and one for total bone thickness. Additionally, a DRR for the overall radiological path was created by calculating the total attenuation through the ray for both bone and soft-tissue. Note that in this paper, the DRR's refer to BEV images of ExacTrac which indicate tissue thicknesses rather than the summation of attenuation coefficients to calculate radiological path length.

PP-DE algorithm was implemented that calculates an energy subtracted DE image but assigns a weighting factor value to each pixel-based on the pixel location on the bone and soft-tissue DRRs. Each pixel location has a known bone and soft-tissue thickness pair

owing to *a-priori* CT dataset for the given patient. The assigned DE weighting factor values are determined from the pre-calculated weighting factors from the step phantom experiment (section 2.3.B1). As the bone and soft-tissue thicknesses of the step phantom are discrete, the weighting factors for different pixel locations on the DRRs were generated by interpolation (or extrapolation if needed) to produce a weighting factor image. The weighting factor image was then applied to the DE subtraction Eq.(2.1) on a pixel-by-pixel basis to produce a new DE image. The signal-to-noise ratio (SNR) was calculated for each ROI in **Figure 2.2a** using the mean and standard deviation values for the PP-DE and two conventional DE images. The two conventional DE images used were those that required a constant weighting factor to remove 2cm bone (rib) and 6 cm bone (spine) separately. The PP-DE image uses the optimal weighting factor for each bone overlapped ROI and generates an image, therefore 12 weighting factors were used unlike the two conventional DE images.

## 2.4. Results

### 2.4.A. PP-DE Algorithm

**Figure 2.5a** illustrates the change of CNR as a function of weighting factor for the 2 cm and 6 cm bone region overlapped with 20 cm soft-tissue for the step phantom from one of the four experiments. Similar results were obtained for other regions (data not presented). The optimal weighting factor to eliminate 2 cm bone (via  $CNR \approx 0$ ) is 0.780. Likewise, the optimal weighting factor to eliminate 6 cm of bone is 0.927. **Figure**

**2.5b** demonstrates the conventional DE image when applying a constant weighting factor of 0.780 to the entire image. The intensity between the soft-tissue only region (0 cm bone) and the overlap region (2cm bone) is nearly identical indicating bone cancellation. However, the 6 cm bone region presents with a distinct positive contrast indicating incomplete bone suppression; i.e. positive CNR in **Figure 2.5a** and brighter intensity in **Figure 2.5b**. Increasing the weighting factor to 0.927 in **Figure 2.5c** eliminates the contrast between the 6 cm bone overlap and the 20 cm soft-tissue. However, the 2 cm bone has now over-suppressed presenting with a negative contrast; i.e. negative CNR in **Figure 2.5a** and darker intensity in **Figure 2.5c**. In addition, **Figure 2.5c** (with  $\omega = 0.927$ ) appears noisier than **Figure 2.5b** (with  $\omega = 0.780$ ) in all corresponding regions.

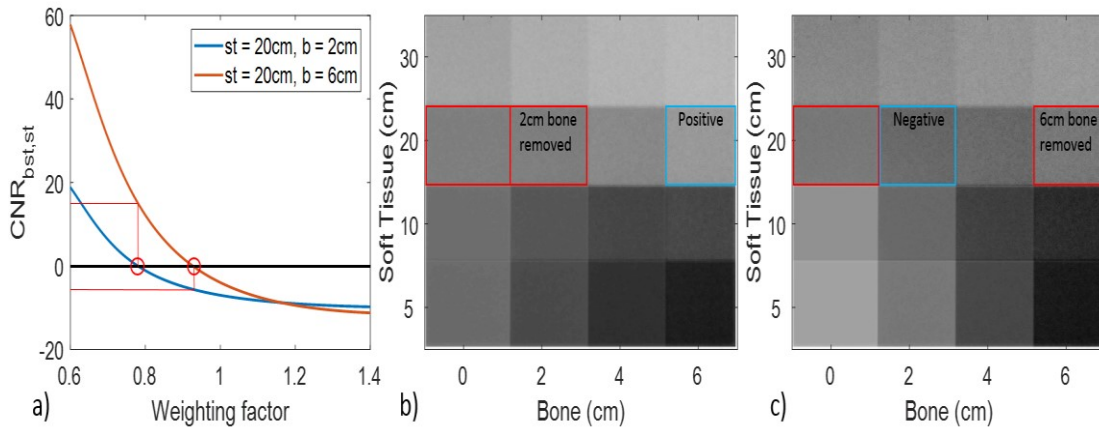


**Figure 2.5:** CNR graphs (a) with the corresponding DE images for 20 cm soft-tissue when overlapped with either 2 cm or 6 cm bone overlap (b, c respectively). The optimal weighting factor is 0.780 for the 2 cm bone (e.g. representing rib) and 0.927 for the 6 cm bone (e.g. representing spine).

**Figures 2.6a, 2.6b, and 2.6c** depict the DRR images of the Rando phantom for soft-tissue, bone and total radiological pathlength respectively. Due to ExacTrac geometry with oblique beam angles, these images are not simple anterior-posterior or

lateral views. However, the spine and ribs can be readily identified. The range of soft-tissue and bone thicknesses were [5 - 26 cm] and [0 - 7 cm] respectively which was similar to the step phantom thickness ranges. In general, the soft-tissue thicknesses were relatively uniform spanning largely over [20 - 25 cm] range. Regarding the bones, the ribs varied in thickness between [1 - 2 cm], whereas the spine was much thicker with a [4 - 7 cm] range.

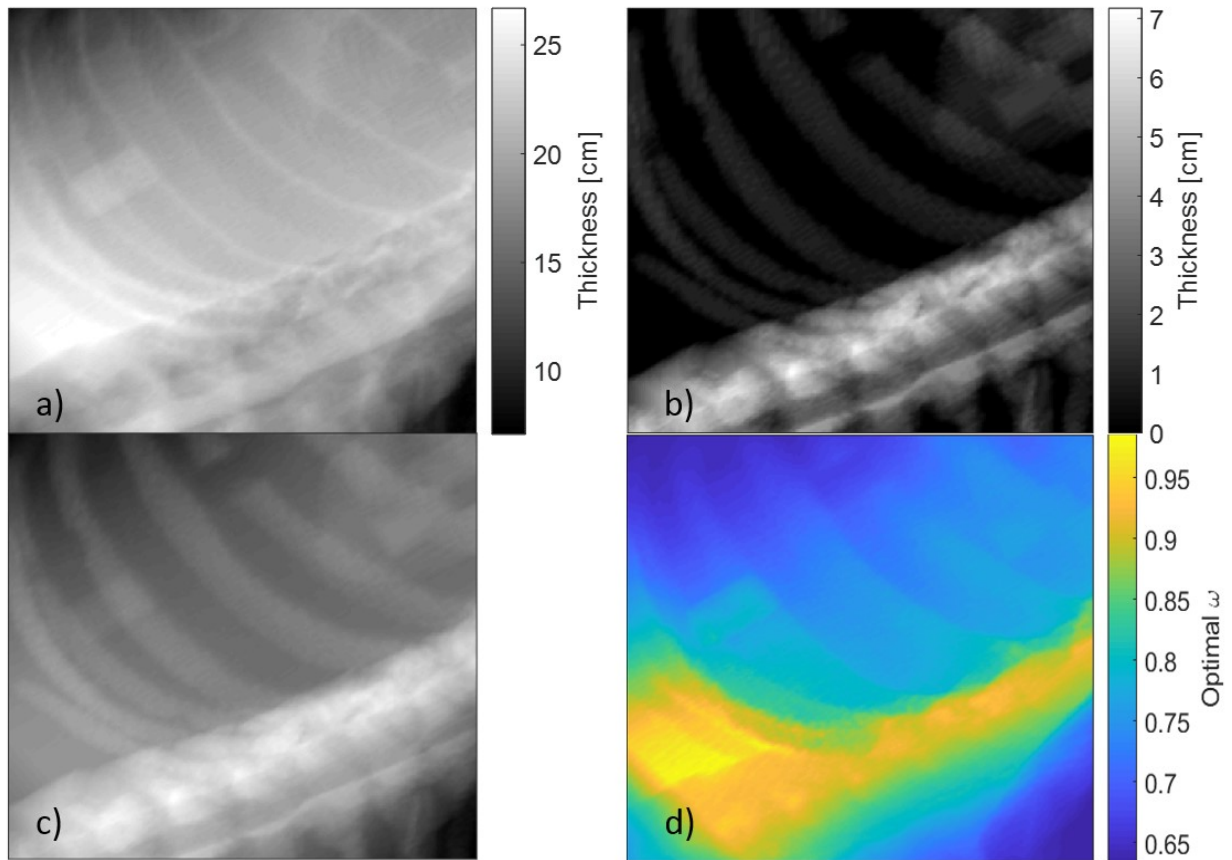


**Figure 2.6:** Soft-tissue (a) and bone (b) DRRs created by ray tracing through CT data from the Rando phantom. The total radiological DRR (c) includes both soft-tissue and bone. Weighting factor image (d) produced by using the *a-priori* information from the DRRs.

**Figure 2.6d** illustrates the weighting factor image for the Rando phantom generated using the PP-DE algorithm. As the Rando phantom thickness ranges were

comparable to those of the step phantom, most weighting factors only needed interpolation. However, occasional extrapolations were used especially for those pixels with exceeding 6 cm bone thickness.

The range of weighting factors in **Figure 2.6d** was [0.632 – 0.986] and the general trend was that regions with thicker bone or soft-tissue required greater weighting factors to cancel bone. The bright yellow regions with large weighting factors indicate the spine with [4 - 7 cm] and/or >25 cm soft-tissue.

**Figure 2.7a** is the clinical single energy image of the Rando phantom at 120 kVp, illustrating the presence of bone and soft-tissue overlap. The visibility of the solid water tumor insert is reduced due to the presence of rib overlap. **Figures 2.7b** and **2.7c** demonstrate the conventional DE image of the Rando phantom which uses a constant weighting factor across the image to eliminate either rib or spine respectively. A constant weighting factor to cancel the ribs presents a positive spine contrast (**Figure 2.7b**). Increasing the weighting factor to cancel the spine causes a negative contrast on the ribs while increasing the noise level across the image (**Figure 2.7c**). These effects are similar to the step phantom results in **Figure 2.5**. **Figure 2.7d** demonstrates the novel PP-DE image, which uses the weighting factor image in **Figure 2.6d** for each individual pixel. It is evident from the new DE image that both rib and spine cancellation occur simultaneously. The tumor visualization has been improved with the conventional DE image in **Figure 2.7b** in comparison to the single energy in **Figure 2.7a**. However, the tumor contrast appears to be improved further in **Figure 2.7d** indicating better tumor visualization. The new DE image (**Figure 2.7d**) appears less noisy than both conventional DE images (**Figures 2.7b, 2.7c**).

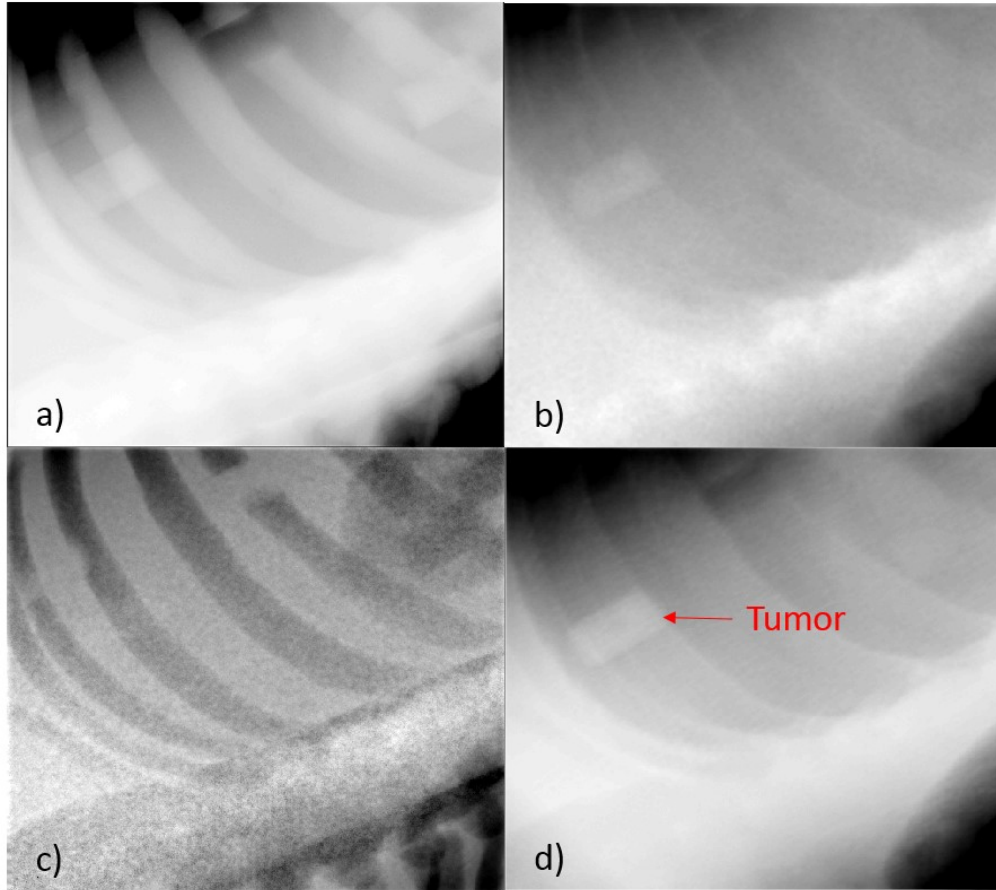


**Figure 2.7:** Clinical single energy x-ray image (a). Conventional DE image with a constant weighting factor across the image to cancel either the ribs (b) or spine (c). The PP-DE image (d) provides both rib and spine cancellation. Note the higher tumor contrast in the DE images compared to the single energy (red arrow). The pixel passed DE image provides both better tumor contrast and lower noise compared to the conventional DE images.



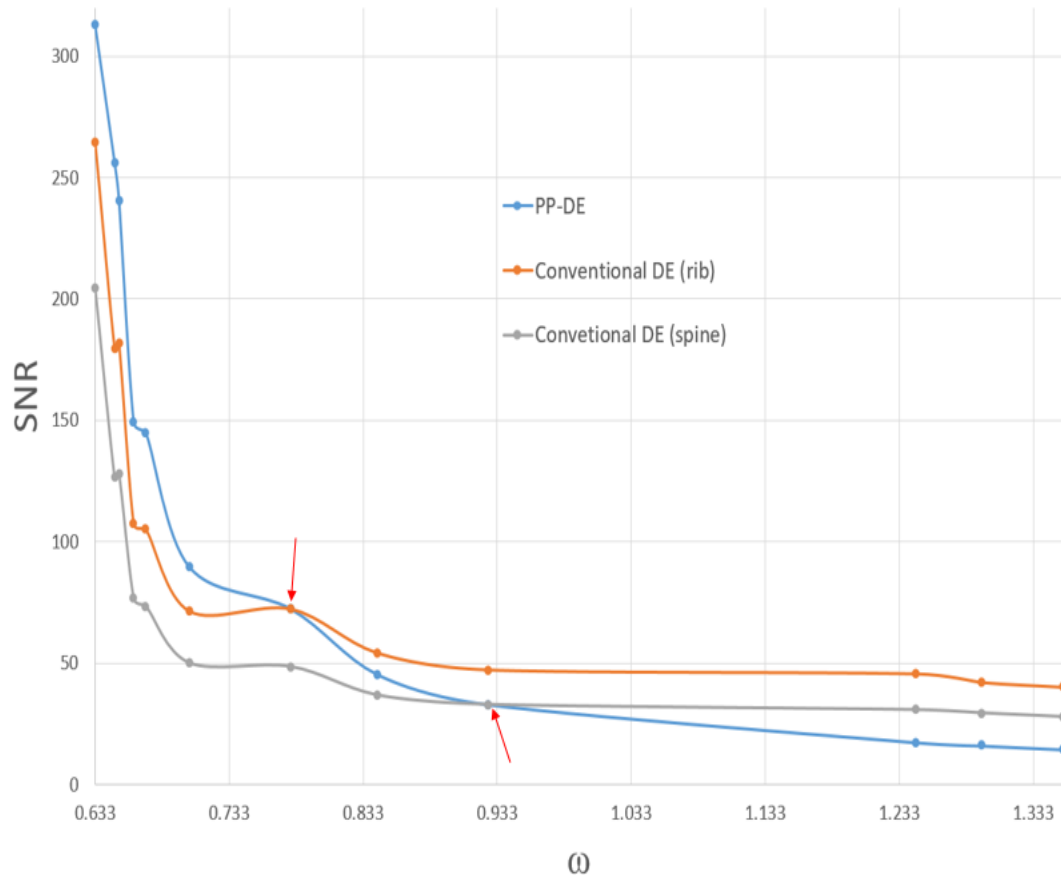


**Figure 2.8:** Signal-to-noise (SNR) comparison between the PP-DE algorithm and conventional DE techniques demonstrating improved SNR at lower weighting factors.

**Figure 2.8** demonstrates the relationship between the SNR and weighting factor for conventional DE and the PP-DE algorithms obtained from the step phantom. The SNRs for the conventional DE rib and spine (orange and grey curves) correspond to different bone overlapped regions in **Figure 2.5b** and **2.5c** respectively. For both conventional and PP-DE algorithms, SNRs monotonically decrease with increasing weighting factor. At lower weighting factors, the SNR in the PP-DE image is greater than both conventional DE techniques. However, at larger weighting factors (when  $\omega > 0.927$ ), the opposite is true. These results are obtained using the step phantom, however, note that the  $\omega$  range in the Rando phantom does not exceed 1.0 (**Figure 2.6d**). The two

red arrows indicate points when the PP-DE curve (blue) crosses the conventional DE curves (orange and grey) at weighting factors of 0.780 and 0.927 as indicated by the red arrows. This is because the PP-DE image also used weighting factors of 0.780 and 0.927 in the formation of the new DE image for those specific ROIs, therefore they will have the same SNRs.

#### **2.4.B. Parameters Affecting Weighting Factor**

**Figure 2.9** illustrates the results of the scatter removal experiment using the step phantom for LE (60 kVp). Similar results were obtained for HE (140 kVp) (data not presented). **Figure 2.9a** is the acquired LE x-ray image (has both primary and scatter) where the steel beam stopper points are visible in each ROI. **Figure 2.9b** is the scatter image obtained by interpolating the scatter signals under each steel pin. The scatter fraction image in **Figure 2.9c** indicates how much scatter contributes to total signal in each ROI. As expected, regions with thicker bone or soft-tissue have larger scatter fraction due to greater scatter contribution. The opposite trend is observed for the scatter image (**Figure 2.9b**) as the absolute signal values are affected by the attenuation. The ROIs with 30 cm soft-tissue contribute extremely large amounts of scatter, where the scatter fractions are up to 0.85 for LE (and 0.70 for HE), indicating the majority of signal in this region is from the scatter radiation. Once the scatter image in **Figure 2.9b** was subtracted from the LE image (**Figure 2.9a**), a scatter corrected x-ray image was generated as per **Figure 2.9d**.

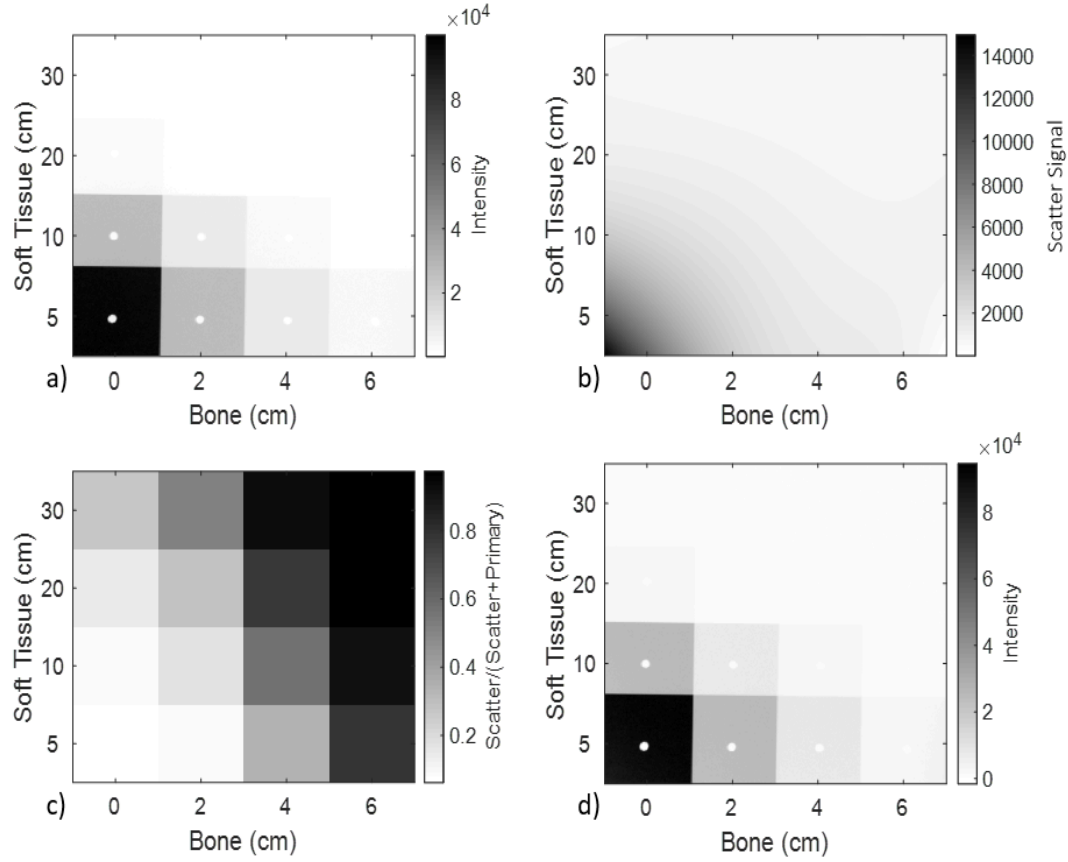


**Figure 2.9:** The LE x-ray image with the steel pins (a). The LE scatter interpolated image (b) where most of the absolute scatter signal appears at thinner areas. The scatter fraction image (c) demonstrates that the majority of signal in thicker regions is from scatter. The scatter corrected LE image (d).

**Table 2.1** summarizes the measured and theoretical weighting factors at different bone and soft-tissue thickness pairs. **Tables 2.1a** and **2.1b** outlines the results of the measured weighting factors using the step phantom before and after scatter removal respectively. Similarly, the theoretical weighting factors using the Spektr simulation are summarized. The theoretical weighting factors for an ideal detector with monoenergetic and polyenergetic beams are presented in **Table 2.1c** and **2.1d** respectively. **Table 2.1e** are the theoretical weighting factors for polyenergetic beams when non-ideal detector effects are included.

**Figure 2.10** demonstrates the plots of the ratios of mean measured to theoretical weighting factors for corresponding thickness pairs and illustrates the effects of various parameter. These parameters include scatter, beam hardening (using polyenergetic beams), and detector effects (quantum efficiency and energy absorption). When all parameters are included, the theoretical weighting factors match those of the measured weighting factors within 3% for all thickness pairs. The only discrepancy was for the region with 30 cm soft-tissue and 6 cm bone which is caused by the loss of measured signal due to excess attenuation leaving only noise after scatter removal.

**Table 2.1:** Measured ((a) and (b)) and theoretical ((c) to (e)) weighting factors demonstrating the effects of different imaging parameters. In (a) and (b) values are mean  $\pm$  standard deviation.

| Soft-tissue (cm) | (a) Measured         |                      |                      |
|------------------|----------------------|----------------------|----------------------|
| 30               | 1.285<br>$\pm 0.002$ | 1.311<br>$\pm 0.013$ | 1.372<br>$\pm 0.013$ |
| 20               | 0.784<br>$\pm 0.002$ | 0.852<br>$\pm 0.002$ | 0.937<br>$\pm 0.004$ |
| 10               | 0.651<br>$\pm 0.000$ | 0.673<br>$\pm 0.001$ | 0.708<br>$\pm 0.001$ |
| 5                | 0.633<br>$\pm 0.000$ | 0.648<br>$\pm 0.001$ | 0.664<br>$\pm 0.000$ |
| Bone (cm)        | 2                    | 4                    | 6                    |

| Soft-tissue (cm) | (b) Measured (scatter corrected) |                      |                      |
|------------------|----------------------------------|----------------------|----------------------|
| 30               | 0.656<br>$\pm 0.022$             | 0.654<br>$\pm 0.034$ | 0.843<br>$\pm 0.056$ |
| 20               | 0.643<br>$\pm 0.006$             | 0.637<br>$\pm 0.006$ | 0.638<br>$\pm 0.016$ |
| 10               | 0.646<br>$\pm 0.005$             | 0.650<br>$\pm 0.003$ | 0.654<br>$\pm 0.007$ |
| 5                | 0.636<br>$\pm 0.002$             | 0.646<br>$\pm 0.001$ | 0.654<br>$\pm 0.002$ |
| Bone (cm)        | 2                                | 4                    | 6                    |

| Soft-tissue (cm) | (c) Theoretical (monoenergetic & ideal detector) |       |       |       |
|------------------|--|-------|-------|-------|
| 30               | 0.371  | 0.371 | 0.371 | 0.371 |
| 20               | 0.371  | 0.371 | 0.371 | 0.371 |
| 10               | 0.371  | 0.371 | 0.371 | 0.371 |
| 5                | 0.371  | 0.371 | 0.371 | 0.371 |
| 0                | 0.371  | 0.371 | 0.371 | 0.371 |
| Bone (cm)        | 0  | 2     | 4     | 6     |

| Soft-tissue (cm) | (d) Theoretical (polyenergetic & ideal detector) |       |       |       |
|------------------|--|-------|-------|-------|
| 30               | 0.582  | 0.588 | 0.593 | 0.597 |
| 20               | 0.582  | 0.590 | 0.596 | 0.600 |
| 10               | 0.579  | 0.591 | 0.598 | 0.602 |
| 5                | 0.571  | 0.592 | 0.599 | 0.604 |
| 0                | 0.549  | 0.591 | 0.600 | 0.605 |
| Bone (cm)        | 0  | 2     | 4     | 6     |

| Soft-tissue (cm) | (e) Theoretical (polyenergetic & detector effects) |       |       |       |
|------------------|--|-------|-------|-------|
| 30               | 0.582  | 0.645 | 0.640 | 0.645 |
| 20               | 0.582  | 0.644 | 0.650 | 0.655 |
| 10               | 0.579  | 0.637 | 0.642 | 0.675 |
| 5                | 0.571  | 0.622 | 0.638 | 0.649 |
| 0                | 0.549  | 0.625 | 0.644 | 0.648 |
| Bone (cm)        | 0  | 2     | 4     | 6     |

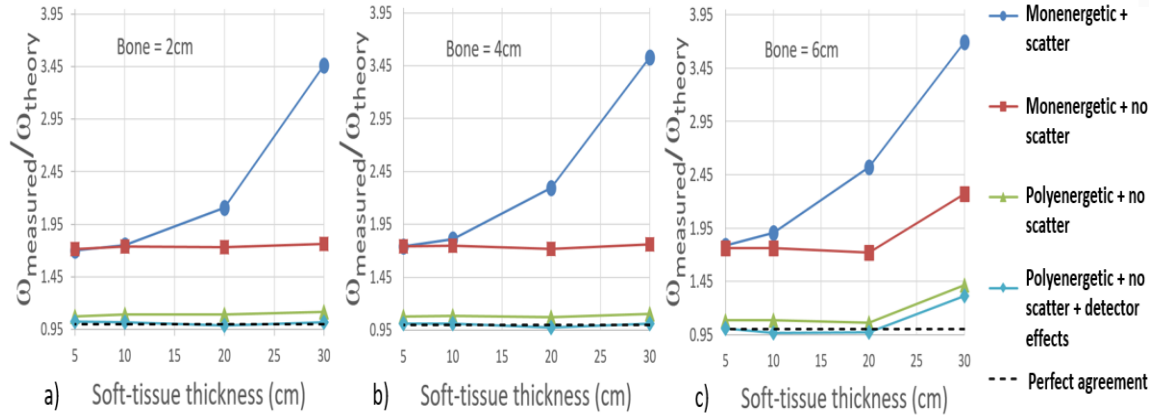


**Figure 2.10:** Ratios of weighting factors (measured/ simulated) for various soft-tissue and bone thicknesses.

## 2.5. Discussion

In this study, a novel PP-DE algorithm was developed and implemented in a clinical x-ray imaging system. This algorithm overcomes the limitation of the conventional DE algorithm in removing given tissue type throughout the image with improved noise and contrast. Although this technique was demonstrated on one imaging system, the algorithm is general and can be applied to other imaging systems provided that step phantom calibration is performed to acquire pre-calculated weighting factors. Since calibration uses clinical LE and HE beams, beam hardening effects are inherently included. In order to assign the weighting factors, the algorithm takes the advantage of *a-priori* CT images which is typically already available for radiotherapy (RT) patients. In principle, it could also be applied to non-RT patients if a pre-CT is available. However, this requirement may not always be met, or the pre-CT may not be in the same patient position.

The novel DE algorithm in this study produced soft-tissue-only images by removing bone overlap using Eq.(2.1) which could be used in clinical applications such as daily IGRT of lung SBRT patients. Similar results would be expected if PP-DE algorithm was developed to produce bone-only images which could be useful for different clinical applications such as spine SBRT. In this case, Eq.(A.37) from the Appendix should be used and the step phantom should be modified to include a slab with zero soft-tissue thickness.

The calibration step phantom (**Figure 2.1a**) had only two tissue types: solid water (representing soft-tissue) and an average bone mimicking material. Other tissue types may exist in the patient such as lung or different kinds of bones (cortical or trabecular). Fortunately, the *a-priori* CT images contain information on all these different tissue types since each type has a distinct HU value. The linear attenuation coefficients for Compton interactions depend on density, while the photoelectric interactions depend on both density and atomic number. Therefore, density scaling is valid for tissues that are different only in density while their effective atomic numbers are similar (e.g. lung and soft-tissue). Density scaling may also be applied to different types of bones with similar effective atomic numbers but different densities. However, if the variation in atomic number is high a modification of the step phantom may be required.

In general, the new DE algorithm had better noise properties than the conventional DE algorithm. This is confirmed for the Rando phantom (**Figure 2.7**), the step phantom (**Figure 2.5**), and the SNR plot (**Figure 2.9**). The noise level in **Figure 2.7d** visually appears to be lower than both **Figure 2.7b** and **2.7c** due to lower weighing factors for most pixels. Similarly, the visually lower noise content in **Figure 2.5b** of the

step phantom compared to the corresponding regions in **Figure 2.5c** is due to lower weighting factor. **Figure 2.9** demonstrates that SNR of DE image monotonically decreases with increasing weighing factor  $\omega$ . This can be explained by two different causes. The first is the noise propagation in the log-subtraction technique, in which the DE noise  $\sigma_{DE}$  can be obtained using <sup>63,64,71,72</sup>:

$$\sigma_{DE}^2 = \sigma_{HE}^2 + \omega^2 \sigma_{LE}^2 \quad (2.4)$$

where  $\sigma_{LE}$  and  $\sigma_{HE}$  are the signal noise of the LE and HE images respectively. Note that this equation is strictly correct for simple log subtraction while in this study noise is suppressed using the ACNR technique.<sup>26,29,30</sup> However, since ACNR was applied to both PP-DE and the conventional DE algorithms, the improved noise in the PP-DE algorithm is expected.

The second reason of reduced SNR for higher  $\omega$  pertains to the fact that thicker regions (with larger  $\omega$ ) attenuate more x-rays reducing the relative signal in these regions and thus will have more relative quantum noise due to less number of photons. This is observed in the step phantom images in **Figure 2.5b** (or **2.5c**), where thicker regions within each image appear noisier.

This study also established theoretical basis of various parameters that affect weighting factors in log-subtraction DE algorithm. Analytic expressions for weighting factors are derived in the Appendix, simulated in Spektr, and validated by matching to experimental results. The parameters that affect weighing factors are beam hardening (for polyenergetic beams), scatter, and detector response as summarized in **Table 2.1**. Note that although the range of weighting factors in this table is small, they have large effects on the final DE image since the effect of  $\omega$  is logarithmic as per Eq.(2.1). In the simple



monoenergetic case, all weighting factors are constant at different regions (Eq.(A.7), **Table 2.1c**). **Figure 2.10** suggests that scatter and beam hardening are two major parameters affecting  $\omega$ . As expected, the effect of scatter depends on the patient thickness; i.e. larger effects on  $\omega$  for thicker regions. This is due to larger scatter fraction in thicker regions (**Figure 2.9c**). The pre-calculated  $\omega$  values using the step-phantom (**Table 2.1a**) includes scatter effects which may be different than patient scatter due to different geometry. Although the scatter fraction image (**Figure 2.9c**) suggests that most scatters are small angle scattering, it is best to minimize the scatter using established methods such as anti-scatter grids.

**Table 2.1d** indicates that when beam hardening effects are taken into account for polyenergetic beams, weighting factors are no longer constant but increase in thicker regions. This can be explained by Eq.(A.9) as beam hardening increases the effective beam energy for both LE and HE hence reducing  $\bar{\mu}^b$ . However,  $\bar{\mu}_L^b$  decreases more than  $\bar{\mu}_H^b$  thus increasing  $\omega$  for thicker regions. Note also that beam hardening effects on  $\omega$  is more pronounced when only a few cm of (soft-tissue or bone) material is added to zero thickness. At large thicknesses when the beams are hardened enough, this effect quickly diminishes.

**Figure 2.10** and **Table 2.1e** indicates that the effects of detector response on  $\omega$  is relatively small (compared to scatter and beam hardening effects) while not negligible. The weighting factors in the bone overlapping regions increased from values in **Table 2.1d** except for the ROIs with no bone. This is explained by Eq.(A.22), where the effect of no bone reduces the equation for weighting factor into Eq.(A.9). Once all the parameters affecting  $\omega$  are incorporated, the measured and theoretical weighting factors

are in close agreement as observed in **Figure 2.10**. A 3% agreement between measurement and simulation  $\omega$  was obtained for all regions except for the thickest region (30 cm soft-tissue overlapped with 6 cm bone). At this region, the majority of signal was attenuated, leaving only noise signal.

The novel PP-DE algorithm relies on correct alignment between DRRs and projection LE and HE images to assign a suitable weighting factor for each pixel. In practice, patients may be mis-aligned especially at first initial setup. The mis-alignment problem may be overcome or reduced by first using one of the acquired (LE or HE) images to register to the DRR before determining the weighting factors. Alternatively, bone-only conventional DE images may be first produced and then registered to the bone-only DRR to obtain registration parameters. Since the registration is performed on 2D projection images, this extra step should not require excessive computational time.

## 2.6. Conclusion

A novel patient specific pixel-based DE algorithm was developed which uses *a-priori* CT information to assign pre-calibrated weighting factors for different pixels depending on bone and soft-tissue thickness. In comparison to the conventional DE algorithm, it provides complete selective tissue suppression throughout the image at various patient thicknesses with improved noise properties. Additionally, analytic expressions were derived to describe the dependence of DE weighting factors on various parameters such as beam hardening, scatter, and detector response. The expressions were simulated, and the results were validated with experiment.

### Chapter 3: Conclusion

Diagnostic and RT applications of DE could serve as a beneficial technique for improving patient care. Generating soft-tissue-only images are particularly useful in enhancing the tumor visualizations valuable for IGRT in lung SBRT patients.<sup>73,74</sup> In terms of lung SBRT, soft-tissue only DE images are useful in cases where the tumor is overlapped with bony structures such as rib or spine. This thesis described the development of the novel PP-DE algorithm and its implementation on a clinical kV IGRT system. The PP-DE algorithm offers several advantages for lung SBRT. The PP-DE algorithm incorporates patient specific information to overcome the drawback of incomplete bone suppression in conventional DE. Using a step phantom of known tissue thicknesses allows for the inherent correction of beam hardening effects when acquiring the pre-calculated weighting factors. By exploiting the pre-existing CT information, DRRs in the BEV of the kV imaging system can be developed, where each pixel has a unique bone and soft-tissue thickness. The PP-DE technique provides complete bone cancellation, reduces noise, and enhances tumor visualization.

In addition to developing and implementing the novel PP-DE algorithm, this thesis also investigated theoretical effects of various imaging parameters on the weighting factor used in DE imaging. Using Spektr simulation tool, realistic imaging effects such as polyenergetic spectra and flat panel detector response were modeled. Since Spektr only simulates primary spectra, effects of scatter was corrected by measurements. Theoretical expressions describing the effects of these parameters were derived analytically, simulated in Spektr, and validated by measurements. There was a

3% agreement between measured weighting factor and Spektr simulated weighting factor.

This thesis provided a promising direction for the use of the PP-DE technique. However, there are some other areas in this work that can be further improved or investigated to expand the effectiveness of this technique. This chapter focuses on future work directions related to improving the PP-DE algorithm and DE in general.

### 3.1. Modification of Step Phantom

As noted in chapter 2, the range of pre-calculated weighting factors extend from 0.6 to 1.4. The thicker tissue regions have most distinctive attenuation and scatter effects and thus experience the most noise in the image. As per **Table 2.1a**, there is a large jump in weighting factors as the soft-tissue increases in thickness. The addition of 10 cm of soft-tissue causes large jumps in weighting factors when increasing from 10 cm to 20 cm and especially from 20 cm to 30 cm. The PP-DE algorithm calculates the optimal patient specific weighting factor via interpolation from pre-calculated weighting factors. Since there is a large difference in weighting factor values with the addition of 10 cm of soft-tissue, the interpolation may not necessarily be completely accurate.

To obtain a finer resolution in pre-calculated weighting factors, the step phantom would have to be modified to include additional thicknesses of soft-tissue and bone. As per **Table 2.1a**, it appears the effects of adding 5 cm of soft-tissue on weighting factor are less dramatic compared to adding 10 cm. Therefore, the addition of 15 and 25 cm of soft-

tissue could be useful to improve the resolution of pre-calculated weighting factors. In addition, 1, 3, and 5 cm of bone can be added to acquire finer pre-calculated weighting factors. This modification would allow for the collection of 36 pre-calculated weighting factors as in **Figure 3.1**, which is an improvement from the current version with 12 weighting factors. Note that a slab of zero thickness soft-tissue is also included to also allow bone-only PP-DE algorithm implementation (see section 3.6).

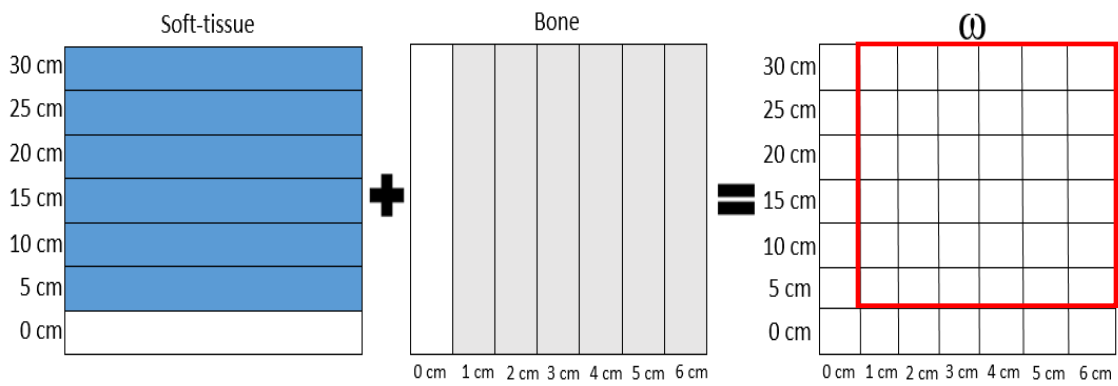


**Figure 3.1:** The proposed modification of the step phantom of soft-tissue and bone slabs to allow storing 36 pre-calculated weighting factors outlined in the red square.

The addition of these regions would allow for a more accurate interpolation of weighting factor during the generation of the PP-DE image. In addition, this could also allow more investigation into the effects of scatter with an increase in region thickness, to improve scatter correction. Creating more overlap regions in the step phantom can also be used to determine the thicknesses at which the noise starts to dominate the signal. This can be useful in determining the limiting thickness such that the measured weighting factors becomes invalid.

### 3.2. Scatter Correction on ExacTrac

As demonstrated in this thesis, the effects of scatter played a significant role in the determination of optimal weighting factor. To allow comparison between measured and simulated weighting factor, scatter was removed from the measured data using a tray of steel pins. The scatter under the steel pins was interpolated to determine the scatter across both the LE and HE image, as well as the scatter to primary ratio and scatter fraction. As illustrated by the LE scatter fraction image in **Figure 2.9c**, for the thinner regions scatter plays a minimal role in the overall signal. However, the thicker regions (30 cm soft-tissue) are heavily influenced by scatter, such that it dominates the useful primary signal. This indicates a major problem which requires a pressing need for scatter removal on the ExacTrac system.

One technique for scatter removal is to include a large air gap between the patient and the detector. An air gap degrades spatial resolution due to focal spot finite size, while additional magnification causing improvements in spatial resolution. Common distances for effective air gaps in chest radiography are between 20 and 30 cm.<sup>75</sup> The air gap between the ExacTrac isocentre and flat panel detector is approximately 123 cm. However, even with such a large gap, our results indicate that there is substantially large scatter signal. To verify the efficiency of scatter reduction via air gap, the step phantom was moved away from the detector in steps of 10 cm from an initial distance of 113 cm away from the detector. The intensity in each of the 16 ROIs was calculated when varying the gap distance to investigate whether scatter reduces with increasing air gap

and diminishes to negligible amounts at large air gaps, as described in literature.<sup>10</sup> The results of the air gap experiment for both LE and HE are illustrated in **Figure 3.2**.

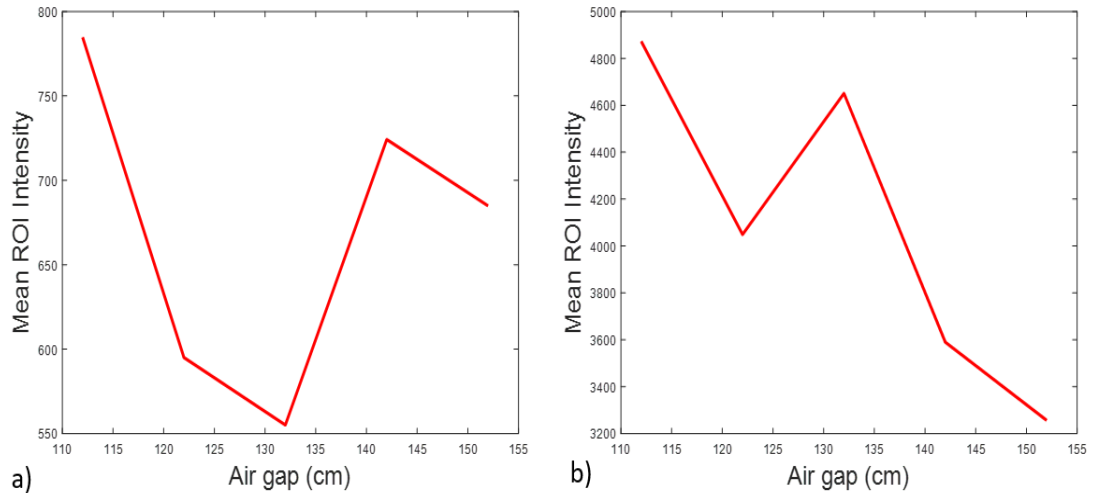


**Figure 3.2:** Mean ROI intensity in a region with 30 cm soft-tissue and 6 cm bone overlap as a function of air gap for both LE (a) and HE (b).

For the LE results, the mean intensity in the ROI decreases with gap size until the 143 cm distance where it increases. The HE results are similar for the first two distances, however the mean ROI intensity increases at a gap size of 133 cm, and then dramatically decreases. Although the underlying reason is not exactly clear, both these plots indicate inconsistent support of the expected scatter trends with increasing air gap. Due to these discrepancies, a different method using the steel pin tray was implemented for a complete and successful scatter removal.

As described in the introduction chapter, one of the most effective tools for scatter removal is the use of anti-scatter grids. Anti-scatter grids reduce scatter thus improve the contrast at the expense of increasing patient dose. While limited technical specs on

ExacTrac detector are available, the results of the scatter fraction above indicates the absence of such device. Therefore, designing and implementing a focused anti-scatter grid would be a direct method and useful in reducing overall scattered radiation.

An alternative method for scatter removal is to simulate scatter using MC with the same patient and x-ray geometries. For IGRT applications, this method exploits pre-existing planning CT images and was studied for other imaging systems such as linac mounted CBCT imaging. A study by Watson *et al* developed a scatter artifact correction strategy using raw CBCT projections.<sup>76</sup> Their method involved converting reconstructed voxel attenuation coefficients to densities and importing them into the MC simulation to create primary and scatter distributions for each projection angle. A scatter correction formula was applied to the data and then 3D reconstructed. A similar scatter correction method could be applied to the ExacTrac planar imaging system, where a MC simulation can be performed with latch bits to create a scatter-only image to subtract from the raw image.

Another method for scatter removal is to make use of *a priori* CT which has been studied to suppress scatter in CBCT.<sup>77</sup> In this method the raw projection image is subtracted from forward projected CT data to estimate the scatter image. The scatter image is then subtracted from the raw image to obtain scatter corrected image. Scatter removal is expected to improve the tumor contrast which is in addition to the contrast improvement of the PP-DE technique discussed in the next section.



### 3.3. PP-DE Contrast Improvement

When comparing the PP-DE image to the conventional DE images, it was evident that there were improvements in bone cancellation, noise reduction, and tumor contrast. Below, analytic expressions are derived to investigate theoretical contrast improvement. In the case where there is a tumor, **Figure A.1** from the Appendix can be modified to include interactions with a tumor of thickness  $t_2$  as per **Figure 3.3**.

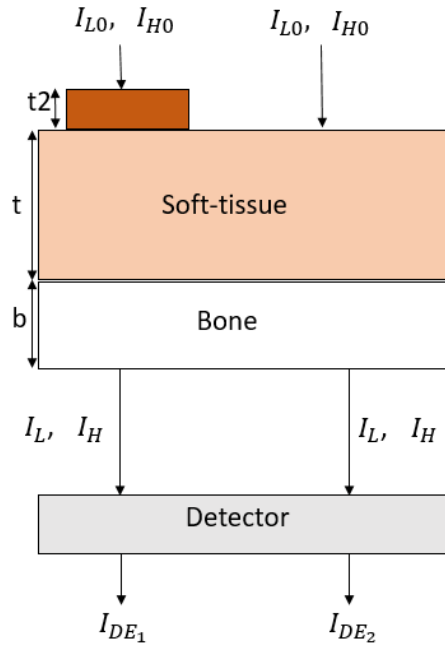


**Figure 3.3:** X-rays interacting with soft-tissue and bone with the addition of a tumor with thickness  $t_2$ .

The conventional DE image contrast between the ray that passes through tumor, soft-tissue, and bone compared to the background of soft-tissue and bone is expressed as:

$$C = I_{DE1} - I_{DE2} \quad (3.1)$$

where,  $I_{DE_1}$  is the intensity of the DE image passing through tumor, soft-tissue and bone, and  $I_{DE_2}$  is the intensity of the DE image passing through soft-tissue and bone only. The intensity of the LE and HE beam passing through soft-tissue and bone is given by Eq.(A.1) and Eq.(A.2) in the Appendix. The intensity of the LE and HE beams with the addition of a tumor is given as:

$$I_H = I_{H0} e^{-\mu_H^t t - \mu_H^b b - \mu_H^{tu} t_2} \quad (3.2)$$

$$I_L = I_{L0} e^{-\mu_L^t t - \mu_L^b b - \mu_L^{tu} t_2} \quad (3.3)$$

where  $\mu_L^{tu}$  and  $\mu_H^{tu}$  are the linear attenuations of the tumor for LE and HE beams respectively. Applying Eq.(2.1) for a soft-tissue only image for Eq.(3.2) and Eq.(3.3) gives:

$$I_{DE_1} = -\mu_H^t t - \mu_H^b b - \mu_H^{tum} t_2 - \omega(-\mu_L^t t - \mu_L^b b - \mu_L^{tum} t_2) \quad (3.4)$$

Likewise, for  $I_{DE_2}$ :

$$I_{DE_2} = -\mu_H^t t - \mu_H^b b - \omega(-\mu_L^t t - \mu_L^b b) \quad (3.5)$$

By applying Eq.(3.1), the contrast between the tumor and the background is calculated as:

$$C = t_2(-\mu_H^{tum} + \omega\mu_L^{tum}) \quad (3.6)$$

Unlike the conventional DE method which uses a single weighting factor across the image, the PP-DE algorithm uses patient specific pixel-based weighting factors which depend on the thickness of tissue. This means that the weighting factor  $\omega_1$  for the ray passing through the tumor, soft-tissue, and bone will be different than the weighting

factor  $\omega_2$  for the ray passing through only soft-tissue and bone. Therefore, Eq.(3.4) and Eq.(3.5) can be modified as:

$$I_{DE_1} = -\mu_H^t t - \mu_H^b b - \mu_H^{tum} t_2 - \omega_1(-\mu_L^t t - \mu_L^b b - \mu_L^{tum} t_2) \quad (3.7)$$

$$I_{DE_2} = -\mu_H^t t - \mu_H^b b - \omega_2(-\mu_L^t t - \mu_L^b b) \quad (3.8)$$

where  $\omega_1$  is the weighting factor to cancel bone in the presence of tumor and soft-tissue and  $\omega_2$  is the weighting factor to cancel bone in the presence of soft-tissue only. When applying Eq.(3.1), the contrast for the PP-DE algorithm is:

$$C = t_2(-\mu_H^{tum} + \omega_1 \mu_L^{tum}) + (\omega_2 - \omega_1)(-\mu_L^t t - \mu_L^b b) \quad (3.9)$$

In the case where  $\omega_2$  and  $\omega_1$  are the same, Eq.(3.9) reduces back to the conventional version in Eq.(3.6). What Eq.(3.9) suggests is that when the  $(\omega_2 - \omega_1)(-\mu_L^t t - \mu_L^b b)$  term is positive, the contrast in the PP-DE image is better than the conventional case given that the  $t_2(-\mu_H^{tum} + \omega_1 \mu_L^{tum})$  term is also positive. In this case, the  $(\omega_2 - \omega_1)(-\mu_L^t t - \mu_L^b b)$  term is always positive since  $\omega_1$  is larger than  $\omega_2$ . This is because the tumor adds more soft-tissue thickness, thus more weight as per chapter 2. Therefore,  $(\omega_2 - \omega_1)$  and  $(-\mu_L^t t - \mu_L^b b)$  will both be negative, resulting in a positive product. However, there may be certain cases where the contrast in the PP-DE image may be worse than the conventional DE image. This is due to the term  $t_2(-\mu_H^{tum} + \omega_1 \mu_L^{tum})$ , where depending on the value of  $\omega_1$ , it could give a negative result. To determine when this is the case, LE and HE spectrum weighted linear attenuation coefficients for soft-tissue for the 20 cm soft-tissue and 2 cm bone region was calculated and the  $(-\mu_H^{tum} + \omega_1 \mu_L^{tum})$  contrast term was plotted as a function of  $\omega_1$ . The results are illustrated in

**Figure 3.4**, which indicates at which  $\omega_1$  values the contrast term is positive. The additional contrast term takes on a positive value for  $\omega_1$  values larger than 0.56. The weighting factors in **Table 2.1b** are all larger than 0.56 suggesting the expected tumor contrast improvement. Note that the contrast terms above are based on the primary signal without the effect of scatter.

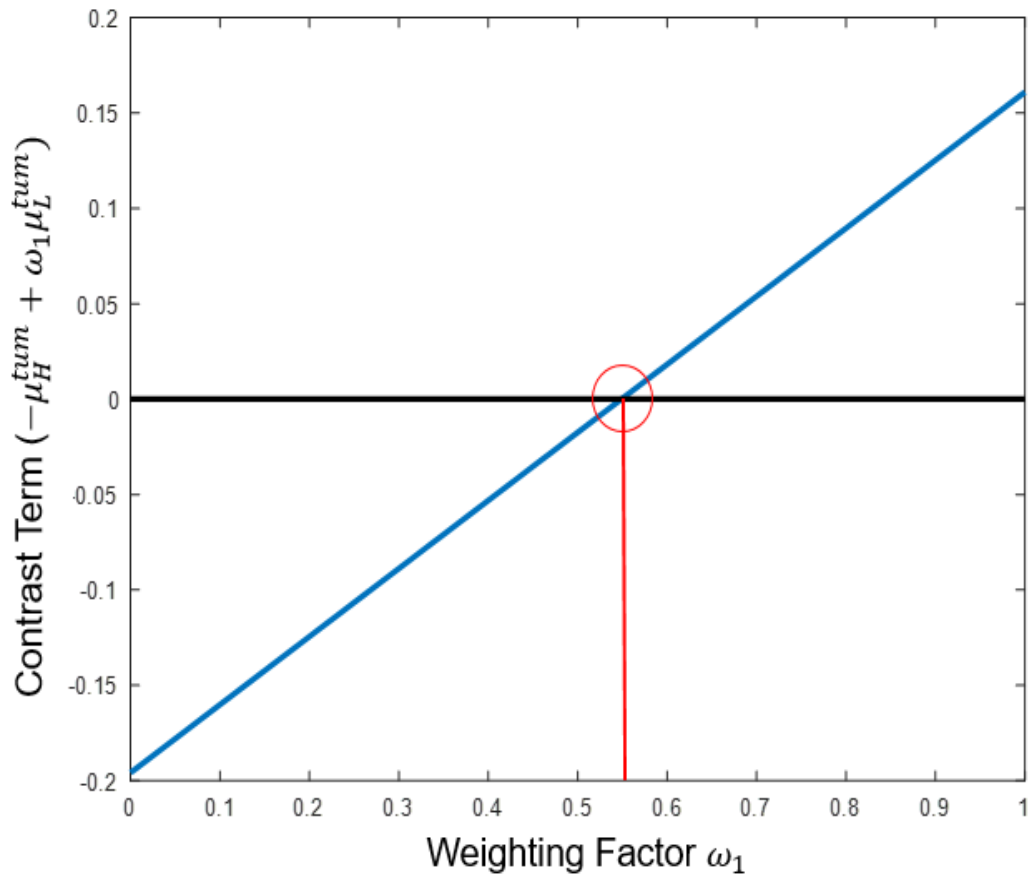


**Figure 3.4:** The additional contrast term as a function of weighting factor. The range at which the additional contrast term is negative is from 0 to 0.56.

In order to verify the contrast improvement via measurement, a tumor plate was constructed (**Figure 3.5a**) with 12 cylindrical tumors (1 cm diameter, 3 cm height) and mounted on the step phantom to overlap with the 12 regions of soft-tissue with bone as per **Figure 3.5b**. Conventional DE and PP-DE images were created and the contrast between the tumor overlapped regions and the background was calculated and the results are presented in **Figure 3.6**. In this experiment, all  $\omega_1$  values are larger than 0.56, meaning that the additional term is always positive for these results.



**Figure 3.5:** The tumor plate with 12 cylindrical tumors (a) and after mounting it to the step phantom (b).

Referring to **Figure 3.4**, the PP-DE contrast should theoretically always be improved for  $\omega > 0.56$ . The weighting factors ( $\omega_2$ ) in **Figure 3.6** to cancel the rib region

(red rectangle) and the spine region (blue rectangle) for this experiment was 0.74 and 0.82 respectively. However, when there is the addition of a tumor, the weighting factors within the tumor regions ( $\omega_1$ ) increased to 0.79 and 0.88 respectively, while the previous background weighing factors remained the same.

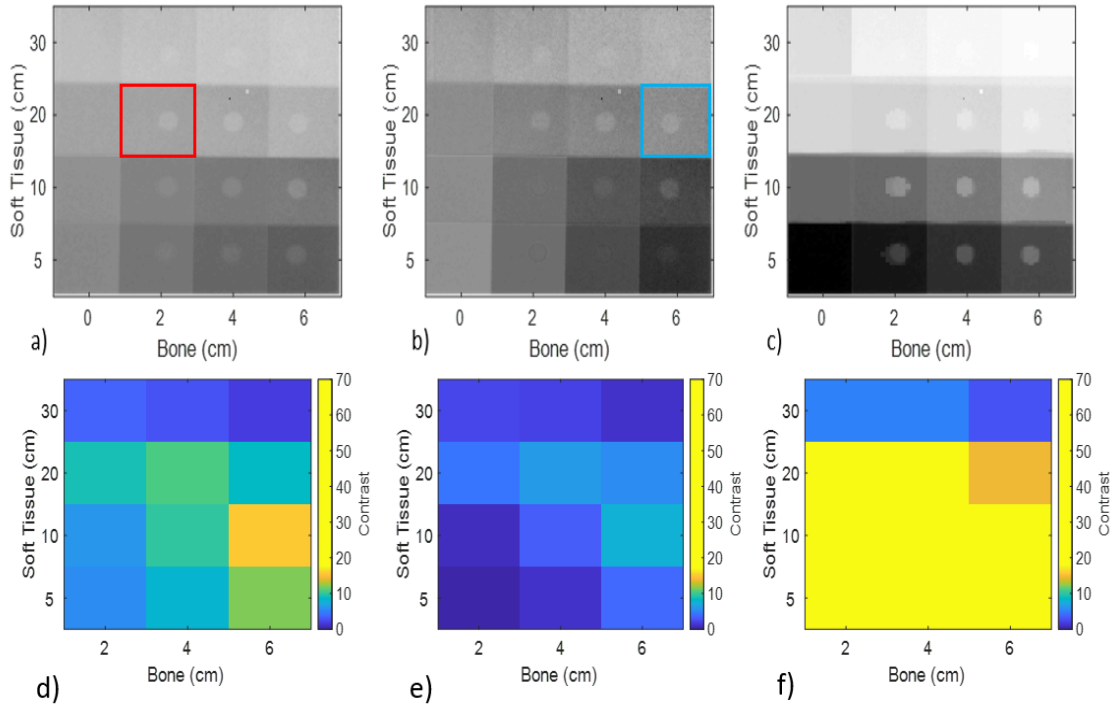


**Figure 3.6:** Conventional DE images with constant weighting factors to cancel either 2 cm rib (a) or 6 cm spine (b) both on 20 cm soft-tissue. The PP-DE image (c) uses optimal weighting factors unique for each pixel. The contrast between the tumor and the background are displayed for bone overlap regions where (d) to (f) correspond to (a) to (c) respectively.

The contrast in the PP-DE image **Figure 3.6c** for the tumors is more enhanced than the contrast in the conventional images **Figure 3.6a** and **Figure 3.6b**. This is also supported by **Figure 3.6f**, where the range of contrast values are significantly higher. For more in

depth analysis of contrast, it is best to scatter correct since the theoretical equations above were derived without the effect of scatter.

### 3.4. Weighting Factor Image Alignment

The success of DE imaging depends greatly on the selection of weighting factor for the removal of specific tissue. Using an incorrect weighting factor leads to an incomplete cancellation of the tissue of interest. The PP-DE algorithm creates its image based on soft-tissue and bone DRRs as well as planar x-ray images. It is important that the BEV from the DRRs is matched with the x-rays to assure accurate alignment for tissue suppression. If the DRRs and x-ray images are not in the same geometry or misaligned, then there will also be a misalignment between the weighting factor image and the x-ray image. This means that improper weighting factors will be applied to every pixel in the x-ray image. Therefore, it is crucial that there is a pre-registered alignment between the DRRs and the x-ray images before the generation of the PP-DE image. The ExacTrac imaging system registers planar images to DRRs for patient alignment. The system pre-calculates a set of DRRs for a range of different patient shifts and rotations. The system then finds the DRR that is the most similar to the planar images and reports the shift and rotation values. To test how misalignment affects the PP-DE image, the weighting factor image (which are made from the DRRs) was shifted 0, 5, and 10 mm in the y-direction and the resulting PP-DE images are presented in **Figure 3.7**. These images clearly indicate misalignment between the BB in the x-ray and weighting factor

image. It appears that shifting the weighting factor image also shifts the overall PP-DE image. This could be because the weighting factor image plays such a pivotal role in Eq.(2.1) as it is logarithmic.

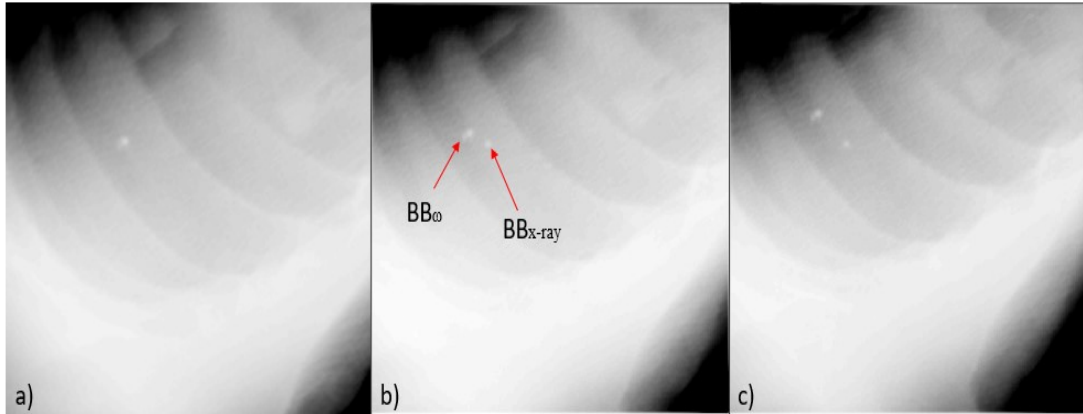


**Figure 3.7:** PP-DE images formed by a misaligned weighting factor image and x-ray image where (a) is a 0 mm, (b) is a 5 mm shift, and (c) is a 10 mm.

While it is not investigated in this thesis, the misalignment problem can be solved or mitigated if one of the LE or HE x-ray images is registered to the DRRs before creating the weighting factor image to ensure alignment with important structures. Another strategy could be to generate a conventional bone-only DE image and register it with the bone DRR to determine the shifting parameters which can then be applied to the soft-tissue DRR to create the soft-tissue-only PP-DE image. Alternatively, a new algorithm may be developed such that the  $\omega$  image may not be obtained from the *a priori* CT images but rather directly from the LE and HE images. In this approach, decomposition DE algorithm may be first applied to created equivalent bone and soft-



tissue thickness images (see section 1.4.2). The decomposed images may then be used to create the  $\omega$  image using pre-calculated weighing factors.

### 3.5 Density Scaling of Different Tissues

In order to make an accurate usage of the pre-calculated weighting factors for the soft-tissue and bone, it was necessary that all tissues within the Rando phantom were converted to their equivalent thicknesses. Tissue materials included within the torso of the Rando phantom were soft-tissue, average bone, and lung mimicking material. Because the step-phantom did not include slabs of lung tissue, a conversion of lung thickness to soft-tissue thickness was calculated via density scaling. The density scaling between lung and soft-tissue was valid since both tissue types are very similar in atomic number and mass attenuation coefficient but only different in density. However, in a realistic clinical setting, a patient would be composed of several tissue types with different physical parameters as per **Table 1.2**. In particular, density scaling between different types of bone needs further investigation.

Tissue types in the human body may include cortical bone (dense compact bone) and trabecular bone (spongy bone). The densities of these bones are different as expected, however there is also a difference in atomic number between these two bones, which suggests a dissimilarity in mass attenuation coefficients. To verify the effectiveness of density scaling using different kinds of bone, small inserts of cortical and trabecular bone were placed inside the Rando phantom. Both bone types were density

scaled to convert to equivalent thicknesses of average bone which was used in the step phantom and then a PP-DE image of the Rando phantom was created. DRRs for cortical and trabecular bone were created and density scaled into average bone as per **Figure 3.8**

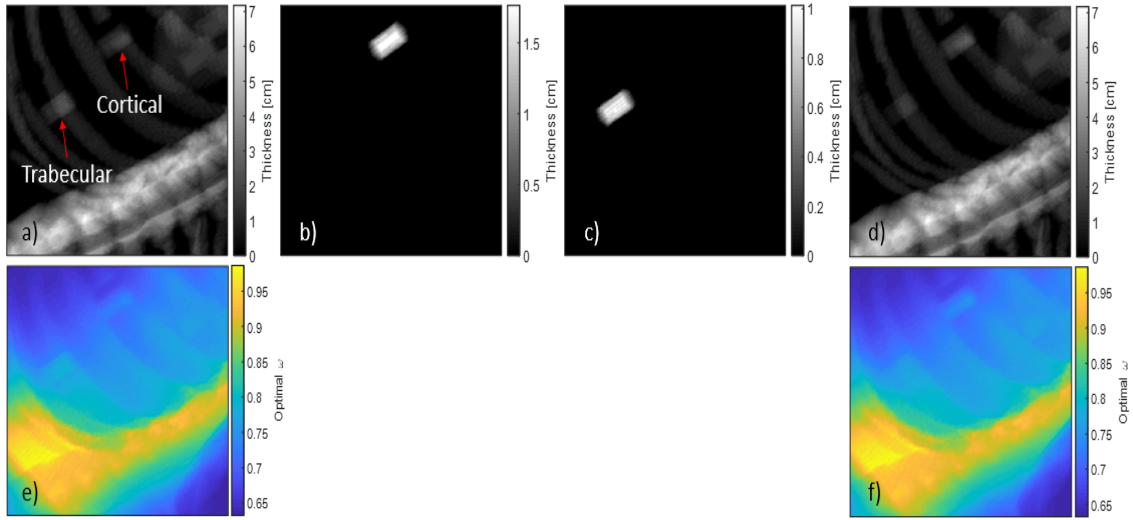


**Figure 3.8:** Non-density scaled bone DRR (a). Density scaled cortical bone (b) and density scaled trabecular bone (c) DRRs. Density corrected bone DRR (d). Weighting factor images corresponding to the non-density scaled bone DRR (e) and the density corrected bone DRR (f).

**Figure 3.8a** is the bone DRR without the density scale corrections for the bone inserts. Density scale corrections for both the cortical and trabecular bone DRRs are demonstrated in **Figure 3.8b** and **Figure 3.8c**. A complete density scaled bone DRR is illustrated in **Figure 3.8d**, where the density scaled cortical bone is brighter indicating an increased average bone thickness and the opposite for trabecular. The weighting factor images for the non-scaled and scaled bone DRRs are displayed in **Figure 3.8e** and **Figure 3.8f** respectively. The scaled weighting factor image in **Figure 3.8f** is different

from the non-scaled image in terms of less weight to the trabecular bone insert, and more weight to the cortical bone insert.

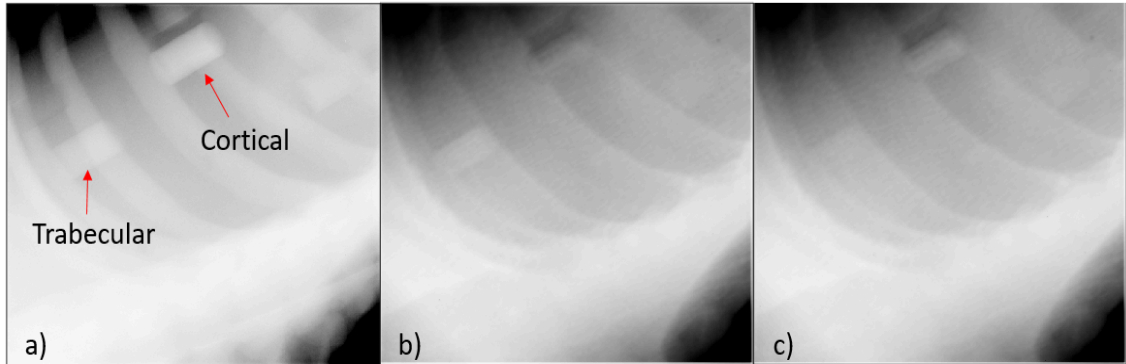


**Figure 3.9:** An HE image of the Rando phantom with the trabecular and cortical bone inserts (a). The PP-DE images created using the non-density scaled bone DRR (b) and the density scaled bone DRR (c).

In **Figure 3.9a**, the presence of the trabecular and cortical bone inserts are present, where the cortical bone appears brighter due to its higher density and atomic number. The PP-DE image in **Figure 3.9b** appears to be successful in cancelling some of the cortical insert, however the trabecular bone insert appears to still be visible. However, the opposite is seen in **Figure 3.9c**, where density scaling caused cancellation of the trabecular bone but not the cortical bone. This suggests that density scaling may not be valid for all bone types. The average bone used in this study is comprised of a mixture between the trabecular and cortical bone. Therefore, a possible reason for successfully suppressing the trabecular bone in **Figure 3.9c** could be that the majority of the average bone is composed of trabecular bone. To improve the PP-DE algorithm's capability of tissue suppression for different bone types, modifications should be made to the step phantom to also include slabs of those specific tissues of interest (i.e. add slabs of cortical

bone to the step phantom and calculate weighting factor). Another simpler approach without modifying the step phantom is to multiply an atomic number correction factor to the density scaling factor, such that it scales different bone types correctly. This would be an empirical correction factor which depends on the energy and could be determined by try and error.

### **3.6. Bone-only PP-DE Algorithm**

The work in this thesis focused on developing the PP-DE algorithm and testing its efficacy for soft-tissue-only images. However, the PP-DE algorithm can also work for generating bone-only DE images. A bone-only PP-DE image can be used for patients with spinal metastases that have been obscured by the overlap of soft-tissue in the stereoscopic projection images. Thus it could have clinical applications for image guidance for spine SBRT patients. Creating a bone-only PP-DE image would be carried out in a similar manner as a soft-tissue-only PP-DE image. The major difference in terms of image formation is the modification of a step phantom. For soft-tissue-only, the step phantom was constructed such that there were overlaps with both bone and soft-tissue, but also regions of soft-tissue thickness alone. This was created such that when empirically finding pre-calculated weighting factors, the CNR in a bone overlapped regions could be directly compared to a soft-tissue only region. To determine the bone-only pre-calculated weighting factors the same method can be used, however the step phantom needs to be modified such that there are regions of bone alone (i.e. having a slab

of zero thickness soft-tissue). The proposed step phantom design in section 3.1 (**Figure 3.1**) includes this update.

With the updated step phantom design, the pre-calculated weighting factors can be calculated empirically similar to those of the soft-tissue. However, rather than applying Eq.(A.3) by means of finding CNR close to zero, the following equation needs to be applied:

$$\ln(I_{DE}(t, b)) = \ln(I_{DE}(0, b + t_0)) \quad (3.10)$$

Note that in this case  $t_0$  is always zero. This is because the soft-tissue thickness range is always larger than bone thickness range (see bone and soft-tissue DRRs in **Figures 2.6a** and **2.6b**), thus adding large thicknesses of bone is not practical. To find the bone-only pre-calculated weighting factors, a CNR of region with bone and soft-tissue overlap now has to be compared to a region of bone alone. Generation of the DRRs will remain the same since this was based on CT information on soft-tissue and bone. The bone-only weighting factor image will be created similar to the soft-tissue-only, except it will use the bone-only pre-calculated weighting factors. Once the bone-only weighting factor image is generated, it will create the bone-only PP-DE image using Eq.(A.37) from the Appendix. It is important to note that when generating a bone-only PP-DE image, the weighting factor parameters in the ACNR algorithm should be modified accordingly for optimal noise suppression.

Much like the soft-tissue-only weighting factor, there will be effects of scatter, beam hardening, and detector response which will all influence the bone-only weighting factor. The weighting factor for soft-tissue suppression is reported as  $\mu_H^t / \mu_L^t$  where  $\mu_L^t$  is

the LE linear attenuation for soft-tissue and  $\mu_H^t$  is the HE.<sup>10,26</sup> The derivations of theoretical weighting factor expressions for bone-only weighting factor can be carried out the same way as the soft-tissue-only, but using LE and HE soft-tissue linear attenuations in place of bone. After considering all of the imaging effects, the modified formula for soft-tissue suppressing weighting factor is given by Eq.(A.39) in the Appendix.

### 3.7. PP-DE with Bone Replaced by Soft-tissue

In this study, pre-calculated weighting factors for the step phantom were found by using Eq(A.3) with  $b_0 = 0$ , where a CNR close to zero indicated the optimal bone suppressing weighting factor. However, for this case the bone is not replaced by soft-tissue, but rather by air. This explains why the PP-DE image in **Figure 2.7d** has dark streaks where rib was replaced by air. If soft-tissue PP-DE images were to be generated by replacing the bone with soft-tissue rather than air, Eq.(A.3) would be written such that  $b_0 = b$  rather than  $b_0 = 0$ . Theoretically this should make the darker streaks in **Figure 2.7d** appear more uniform since soft-tissue has been filled in those empty regions.

In order to create a PP-DE image where bone is replaced by soft-tissue, one can simply add the bone DRR to the soft-tissue DRR such that all of the pixels with bone overlap typically replaced by air is now substituted for soft-tissue. The soft-tissue and bone DRRs are displayed in **Figure 3.10a** and **Figure 3.10b**, however the new soft-tissue DRR with the bone thickness added is given in **Figure 3.10c**. The weighting factor image (**Figure 3.10d**) for the old soft-tissue and bone DRR is exactly the same as the one in

**Figure 2.6d.** When using the new soft-tissue DRR, the new weighting factor image (**Figure 3.10e**) has higher weighting factor values than the previous image since the thickness of soft-tissue has increased.

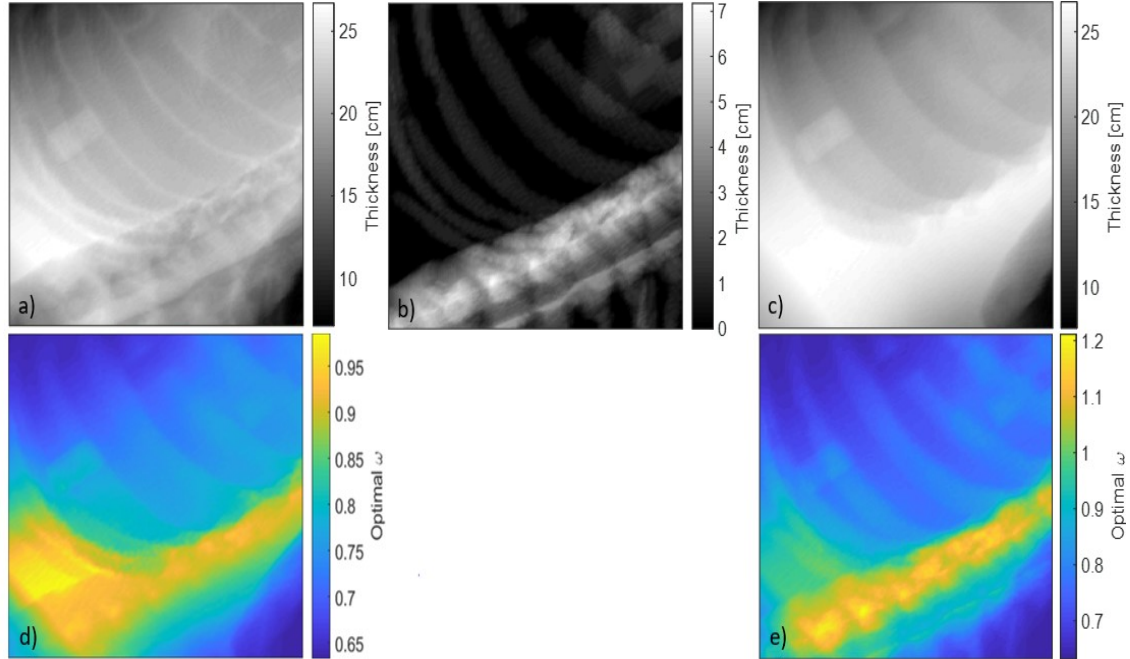


**Figure 3.10:** Soft-tissue (a) and bone (b) DRRs. The new soft-tissue DRR (c) has added bone thickness to replace regions that had air. Weighting factor images for the old-soft tissue and bone DRR (d) and the new soft-tissue DRR (e).

Using the weighting factor images in **Figure 3.10d** and **Figure 3.10e**, PP-DE images were generated. Again, the single energy image in **Figure 3.11a** demonstrates the presence of bone and poor tumor visualization. The PP-DE image displayed in **Figure 3.11b** demonstrates bone cancellation, where the bone has been replaced with air. However, the PP-DE image in **Figure 3.11c** appears to be enhancing the bone rather than suppressing it. It was theorized that the darker regions where rib was cancelled in **Figure**

**3.11b** would become more uniform with the replacement of air by soft-tissue, however that is not what is visualized in **Figure 3.11c**. A possible reason for this is that the weighting factors interpolated between 20 and 30 cm of soft-tissue are very high (due to scatter), therefore the overlap regions are more highlighted. With an efficient scatter reduction technique, a PP-DE image may be formed where bones are replaced by soft tissue correctly. The proposed updated step phantom in section 3.1 with finer step sizes could also help to prevent overestimating the weighting factors.

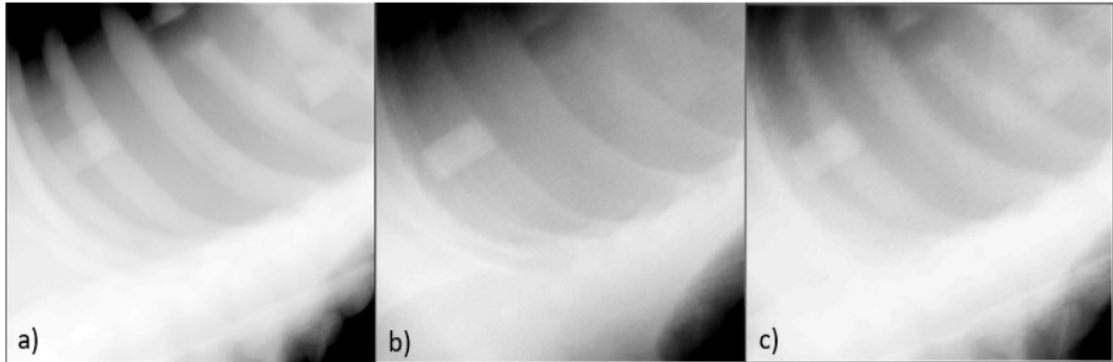


**Figure 3.11:** Clinical single energy x-ray image (a). PP-DE image made from the old soft-tissue and bone DRR (b) and the PP-DE image made from the new soft-tissue DRR (c).

### 3.8. Final Remarks

This thesis had two main objectives. The first objective was successfully accomplished by developing a novel patient specific pixel-based weighting factor DE x-ray imaging system that is able to suppress all thicknesses of bone in an x-ray image. Compared to the conventional method which uses a uniform weighting factor across the



image, this new algorithm uses a unique weighting factor for every pixel based on the thickness of soft-tissue and bone in the given pixel location. In addition to bone cancellation, the novel DE algorithm demonstrated improved noise characteristics as well as enhanced tumor visualization. The images generated by the PP-DE algorithm can be used for both diagnostic and RT applications, especially in cases where there may be lung tumors obscured by different thicknesses of bone.

The second objective of this thesis was also achieved by deriving and validating theoretical expressions for weighting factor incorporating realistic imaging parameters such as polyenergetic spectra, scatter, and detector response. Most these effects were simulated using Spektr, however the scatter was removed from measurement. Once the measured data was scatter corrected, it was compared to the theoretical simulated weighting factors to validate the accuracy of the modified equations with measurement. A 3% accuracy was achieved which effectively validates the derived theoretical expressions.

This thesis covered the PP-DE generation of soft-tissue only images which have applications in lung SBRT. However, future steps in this work would be to modify the step phantom to generate bone-only PP-DE images which may have applications for spine SBRT. Other important future research avenues were also highlighted. These include modifying the step phantom to achieve finer resolution of the weighting factors, implementing more efficient scatter removal strategies on the ExacTrac system, further investigations on the theory behind contrast improvement in the PP-DE algorithm, implementation of image registration algorithms to avoid misalignment issues, and updating the PP-DE algorithm to cancel different types of bones.

## Bibliography

1. Bushberg JT, Boone JM. *The essential physics of medical imaging*. 3rd ed. Lippincott Williams & Wilkins; 2011.
2. Punnoose J, Xu J, Sisniega A, Zbijewski W, Siewerdsen JH. Technical note: Spektr 3.0-A computational tool for x-ray spectrum modeling and analysis. *Med Phys*. 2016;43(8):4711. doi: 10.1118/1.4955438 [doi].
3. Boone JM, Seibert JA. An accurate method for computer-generating tungsten anode x-ray spectra from 30 to 140 kV. *Med Phys*. 1997;24(11):1661-1670. doi: 10.1118/1.597953 [doi].
4. Fewell TR, Shuping RE. *Handbook of mammographic X-ray spectra*. HEW Publication (FDA); 1978.
5. Fewell TR, Shuping RE, Healy KE. *Handbook of computed tomography X-ray spectra*. HHS Publication (FDA); 1981.
6. NIST. X-ray mass attenuation coefficients.  
<https://physics.nist.gov/PhysRefData/XrayMassCoef/tab4.html>2017.
7. Kawrakow I, Mainegra-Hing E, Rogers DWO, Tessier F, Walters BRB. The EGSnrc code system: Monte carlo simulation of electron and photon transport. . 2018;PIRS-701.
8. Johns HE, Cunningham JR. *The physics of radiology*. 4th ed. Springfield, IL: Thomas; 1974.
9. Huda W. *Review of radiologic physics*. 3rd ed. Lippincott Williams & Wilkins; 2010.
10. Burton CS, Mayo JR, Cunningham IA. Energy subtraction angiography is comparable to digital subtraction angiography in terms of iodine rose SNR. *Med Phys*. 2016;43(11):5925. doi: 10.1118/1.4962651 [doi].

11. Beutel J, Kundel HL, Van Metter RL. *Handbook of medical imaging*. Bellingham, Washington: SPIE- The International Society for Optical Engineering; 2000.
12. Kuhlman JE, Collins J, Brooks GN, Yandow DR, Broderick LS. Dual-energy subtraction chest radiography: What to look for beyond calcified nodules. *Radiographics*. 2006;26(1):79-92. doi: 26/1/79 [pii].
13. Vock P, Szucs-Farkas Z. Dual energy subtraction: Principles and clinical applications. *Eur J Radiol*. 2009;72(2):231-237. doi: 10.1016/j.ejrad.2009.03.046 [doi].
14. Alvarez RE, Macovski A. Energy-selective reconstructions in X-ray computerized tomography. *Phys Med Biol*. 1976;21(5):733-744.
15. Li H, Giles W, Ren L, Bowsher J, Yin FF. Implementation of dual-energy technique for virtual monochromatic and linearly mixed CBCTs. *Med Phys*. 2012;39(10):6056-6064. doi: 10.1118/1.4752212 [doi].
16. Cardinal HN, Fenster A. An accurate method for direct dual-energy calibration and decomposition. *Med Phys*. 1990;17(3):327-341. doi: 10.1118/1.596512 [doi].
17. Lehmann L.A., Alvarez R.E., Macovski A., Brody W.R. Generalized image combinations in dual KVP digital radiography. *Med Phys*. 1981;8:659-667.
18. Kamimura R, Takashima T. Clinical application of single dual-energy subtraction technique with digital storage-phosphor radiography. *J Digit Imaging*. 1995;8:21-24.
19. MacMahon H, Li F, Engelmann R, Roberts R, Armato S. Dual energy subtraction and temporal subtraction chest radiography. *J Thorac Imaging*. 2008;23(2):77-85. doi: 10.1097/RTI.0b013e318173dd38 [doi].
20. Johnson TR. Dual-energy CT: General principles. *AJR Am J Roentgenol*. 2012;199(5 Suppl):S3-8. doi: 10.2214/AJR.12.9116 [doi].

21. Fischbach F, Freund T, Rottgen R, Engert U, Felix R, Ricke J. Dual-energy chest radiography with a flat-panel digital detector: Revealing calcified chest abnormalities. *AJR, AM J Roentgenol.* 2003;181:1519-1524.
22. Kaza RK, Platt JF, Cohan RH, Caoili EM, Al-Hawary MM, Wasnik A. Dual-energy CT with single- and dual-source scanners: Current applications in evaluating the genitourinary tract. *Radiographics.* 2012;32(2):353-369. doi: 10.1148/rg.322115065 [doi].
23. Euler A, Parakh A, Falkowski AL, et al. Initial results of a single-source dual-energy computed tomography technique using a split-filter: Assessment of image quality, radiation dose, and accuracy of dual-energy applications in an in vitro and in vivo study. *Invest Radiol.* 2016;51(8):491-498. doi: 10.1097/RLI.0000000000000257 [doi].
24. Yu L, Christner JA, Leng S, Wang J, Fletcher JG. Virtual monochromatic imaging in dual-source dual-energy CT: Radiation dose and image quality. *Med Phys.* 2011;38:6371-6379.
25. Engel KJ, Herrmann C, Zeitler G. X-ray scattering in single- and dual-source CT. *Med Phys.* 2008;35(1):318-332. doi: 10.1118/1.2820901 [doi].
26. Richard S, Siewerdsen JH. Cascaded systems analysis of noise reduction algorithms in dual-energy imaging. *Med Phys.* 2008;35(2):586-601. doi: 10.1118/1.2826556 [doi].
27. Richard S, Siewerdsen JH. Optimization of dual-energy imaging systems using generalized NEQ and imaging task. *Med Phys.* 2007;34(1):127-139. doi: 10.1118/1.2400620 [doi].
28. Kalender WA, Klotz E, Kostaridou L. An algorithm for noise suppression in dual energy CT material density images. *IEEE Trans Med Imaging.* 1988;7(3):218-224. doi: 10.1109/42.7785 [doi].

29. Ergun DL, Mistretta CA, Brown DE, et al. Single-exposure dual-energy computed radiography: Improved detection and processing. *Radiology*. 1990;174(1):243-249. doi: 10.1148/radiology.174.1.2294555 [doi].
30. McCollough CH, Van Lysel MS, Pepler WW, Mistretta CA. A correlated noise reduction algorithm for dual-energy digital subtraction angiography. *Med Phys*. 1989;16(6):873-880. doi: 10.1118/1.596436 [doi].
31. Okunieff P, Petersen AL, Philip A, et al. Stereotactic body radiation therapy (SBRT) for lung metastases. *Acta Oncol*. 2006;45(7):808-817.
32. Ahmed KA, Stauder MC, Miller RC, et al. Stereotactic body radiation therapy in spinal metastases. *Int J Radiat Oncol Biol Phys*. 2012;82(5):803-809.
33. Bowman WA, Robar JL, Sattarivand M. Optimizing dual-energy x-ray parameters for the ExacTrac clinical stereoscopic imaging system to enhance soft-tissue imaging. *Med Phys*. 2017;44(3):823-831. doi: 10.1002/mp.12093 [doi].
34. Bissonnette JP, Balter PA, Dong L, et al. Quality assurance for image-guided radiation therapy utilizing CT-based technologies: A report of the AAPM TG-179. *Med Phys*. 2012;39(4):1946-1963.
35. Podgorsak EB. *Radiation physics for medical physicists*. 3rd ed. Springer; 2016.
36. Siddon RL. Fast calculation of the exact radiological path for a three-dimensional CT array. *Med Phys*. 1985;12(2):252-255. doi: 10.1118/1.595715 [doi].
37. Jacobs F, Sundermann E, De Sutter B, Christiaens M, Lemahiew I. A fast algorithm to calculate the exact radiological pathlength through a pixel or voxel space. *Journal of Computing and Information Technology*. 1998;6(1):89-94.
38. International commission on radiation units and measurements. ICRU. report 46: Photon, electron, proton, and neutron interaction data for body tissues. . 1992.

39. Saito M, Sagara S. A simple formulation for deriving effective atomic numbers via electron density calibration from dual-energy CT data in the human body. *Medical physics*. 2017(44):2293-2303.
40. van Elmpt W, Landry G, Das M, Verhaegen F. Dual energy CT in radiotherapy: Current applications and future outlook. *Radiother Oncol*. 2016;119(1):137-144. doi: 10.1016/j.radonc.2016.02.026 [doi].
41. Srinivasan A, Parker RA, Manjunathan A, Ibrahim M, Shah GV, Mukherji SK. Differentiation of benign and malignant neck pathologies: Preliminary experience using spectral computed tomography. *J Comput Assist Tomogr*. 2013;37(5):666-672. doi: 10.1097/RCT.0b013e3182976365 [doi].
42. Forghani R, Levental M, Gupta R, Lam S, Dadfar N, Curtin HD. Different spectral hounsfield unit curve and high-energy virtual monochromatic image characteristics of squamous cell carcinoma compared with nonossified thyroid cartilage. *AJNR Am J Neuroradiol*. 2015;36(6):1194-1200. doi: 10.3174/ajnr.A4253 [doi].
43. Chae EJ, Seo JB, Goo HW, Kim N, Song KS, Lee SD. Xenon ventilation CT with a dual-energy technique of dual-source CT: Initial experience. *Radiology*. 2008;248:615-624.
44. Hachulla AL, Pontana F, Wemeau-Stervinou L, et al. Krypton ventilation imaging using dual-energy CT in chronic obstructive pulmonary disease patients: Initial experience. *Radiology*. 2012;263(1):253-259. doi: 10.1148/radiol.12111211 [doi].
45. Yanagita H, Honda N, Nakayama M, Watanabe W, Shimizu Y, Osada H. Prediction of postoperative pulmonary function: Preliminary comparison of single-breath dual-energy xenon CT with three conventional methods. *Jpn J Radiol*. 2013;31:377-385.
46. Dhont J, Verellen D, Poels K, et al. Feasibility of markerless tumor tracking by sequential dual-energy fluoroscopy on a clinical tumor tracking system. *Radiother Oncol*. 2015;117(3):487-490. doi: 10.1016/j.radonc.2015.08.021 [doi].

47. Xu T, Ducote JL, Wong JT, Molloy S. Dynamic dual-energy chest radiography: A potential tool for lung tissue motion monitoring and kinetic study. *Phys Med Biol*. 2011;56(4):1191-1205. doi: 10.1088/0031-9155/56/4/019 [doi].
48. Devic S, Monroe JI, Mutic S, Whiting B, Williamson JF. Dual energy CT tissue quantitation for monte-carlo based treatment planning for brachytherapy. . 2000.
49. Landry G, Reniers B, Granton PV, van Rooijen B, Beaulieu L, Wildberger JE. Extracting atomic numbers and electron densities from a dual source dual energy CT scanner: Experiments and a simulation model. *Radiother Oncol*. 2011;100:375-379.
50. Malusek A, Karlsson M, Magnusson M, Carlsson GA. The potential of dual-energy computed tomography for quantitative decomposition of soft tissues to water, protein and lipid in brachytherapy. *Phys Med Biol*. 2013;58:771-785.
51. Tsukihara M, Noto Y, Sasamoto R, Hayakawa T, Saito M. Initial implementation of the conversion from the energy-subtracted CT number to electron density in tissue inhomogeneity corrections: An anthropomorphic phantom study of radiotherapy treatment planning. *Med Phys*. 2015;42(3):1378-1388. doi: 10.1118/1.4908207 [doi].
52. American Association of Physicists in Medicine. The role of in-room kV x-ray imaging for patient setup and target localization. report of task group 104 of the therapy imaging committee. . 2009.
53. Wen N, Walls N, Kim J, et al. Clinical use of dual image-guided localization system for spine radiosurgery. *Technol Cancer Res Treat*. 2012;11:123-131.
54. Linthout N, Verellen D, Tournel K, Reynders T, Duchateau M, Storme G. Assessment of secondary patient motion induced by automated couch movement during on-line 6 dimensional repositioning in prostate cancer treatment. *Radiother Oncol*. 2007;83(2):168-174. doi: S0167-8140(07)00163-6 [pii].
55. Chang Z, Wang Z, Ma J, O'Daniel JC, Kirkpatrick J, Yin FF. 6D image guidance for spinal non-invasive stereotactic body radiation therapy: Comparison between ExacTrac

- X-ray 6D with kilo-voltage cone-beam CT. *Radiother Oncol.* 2010;95(1):116-121. doi: 10.1016/j.radonc.2009.12.036 [doi].
56. Stevens MT, Parsons DD, Robar JL. Continuous monitoring of prostate position using stereoscopic and monoscopic kV image guidance. *Med Phys.* 2016;43(5):2558. doi: 10.1118/1.4947295 [doi].
57. Cheng CS, Jong WL, Ung NM, Wong JHD. Evaluation of imaging dose from different image guided systems during head and neck radiotherapy: A phantom study. *Radiat Prot Dosimetry.* 2017;175(3):357-362. doi: 10.1093/rpd/ncw357 [doi].
58. Williams DB, Siewerdsen JH, Tward DJ, et al. Optimal kvp selection for dual-energy imaging of the chest: Evaluation by task-specific observer preference tests. *Med Phys.* 2007;34(10):3916-3925. doi: 10.1118/1.2776239 [doi].
59. Szucs-Farkas Z, Patak MA, Yuksel-Hatz S, Ruder T, Vock P. Single-exposure dual-energy subtraction chest radiography: Detection of pulmonary nodules and masses in clinical practice. *Eur Radiol.* 2008;18(1):24-31. doi: 10.1007/s00330-007-0758-z [doi].
60. Hoggarth MA, Luce J, Syeda F, et al. Dual energy imaging using a clinical on-board imaging system. *Phys Med Biol.* 2013;58(12):4331-4340. doi: 10.1088/0031-9155/58/12/4331 [doi].
61. Menten MJ, Fast MF, Nill S, Oelfke U. Using dual-energy x-ray imaging to enhance automated lung tumor tracking during real-time adaptive radiotherapy. *Med Phys.* 2015;42(12):6987-6998. doi: 10.1118/1.4935431 [doi].
62. Shkumat NA, Siewerdsen JH, Dhanantwari AC, et al. Optimization of image acquisition techniques for dual-energy imaging of the chest. *Med Phys.* 2007;34(10):3904-3915. doi: 10.1118/1.2777278 [doi].
63. Ducote JL, Xu T, Molloy S. Optimization of a flat-panel based real time dual-energy system for cardiac imaging. *Med Phys.* 2006;33(6):1562-1568. doi: 10.1118/1.2174131 [doi].



64. Karunamuni R, Maidment AD. Search for novel contrast materials in dual-energy x-ray breast imaging using theoretical modeling of contrast-to-noise ratio. *Phys Med Biol*. 2014;59(15):4311-4324. doi: 10.1088/0031-9155/59/15/4311 [doi].
65. Ho JT, Kruger RA, Sorenson JA. Comparison of dual and single exposure techniques in dual-energy chest radiography. *Med Phys*. 1989;16(2):202-208. doi: 10.1118/1.596372 [doi].
66. Ay M.R., Sarkar S., Shahriari M., Sardari D., Zaidi H. Assessment of different computational models for generation of x-ray spectra in diagnostic radiology and mammography. *Med Phys*. 2006;32:1660-1675.
67. BrainLAB. User guide imaging couch top. . 2010.
68. Leong DL, Rainford L, Zhao W, Brennan PC. IEC 61267: Feasibility of type 1100 aluminium and a copper/aluminium combination for RQA beam qualities. *Phys Med*. 2016;32(1):141-149. doi: 10.1016/j.ejmp.2015.10.092 [doi].
69. IEC. Medical electrical equipment - characteristics of digital X-ray imaging devices - part 1: Determination of the detective quantum efficiency. . 2003.
70. Hubbell JS, Seltzer SM. Tables of x-ray mass attenuation coefficients and mass energy-absorption coefficients from 1 keV to 20 MeV for elements  $Z = 1$  to 92 and 48 additional substances of dosimetric interest. *Radiat Res*. 1993;136:147-170.
71. Molloy SY, Mistretta CA. Quantification techniques for dual-energy cardiac imaging. *Med Phys*. 1989;16(2):209-217. doi: 10.1118/1.596418 [doi].
72. Sabol J, Wheeldon S, Thompson SK. Simulated and experimental technique optimization of dual-energy radiography: Abdominal imaging applications. *Medical Imaging*. 2006;6142:545-556.

73. Hoggarth M, Luce J, Bray T, Block A, Roeske J. SU-E-J-44: Dual energy subtraction imaging to improve tumor visibility at oblique angles. *Med Phys*. 2012;39(6Part6):3662. doi: 10.1118/1.4734879 [doi].
74. Block AM, Patel R, Surucu M, Harkenrider MM, Roeske JC. Evaluation of a template-based algorithm for markerless lung tumour localization on single- and dual-energy kilovoltage images. *Br J Radiol*. 2016;89(1068):20160648. doi: 10.1259/bjr.20160648 [doi].
75. Newhouse VL. *Progress in medical imaging*. Springer-Verlag; 1988.
76. Watson PG, Mainegra-Hing E, Tomic N, Seuntjens J. Implementation of an efficient monte carlo calculation for CBCT scatter correction: Phantom study. *J Appl Clin Med Phys*. 2015;16(4):216-227. doi: 10.1120/jacmp.v16i4.5393 [doi].
77. Park YK, Sharp GC, Phillips J, Winey BA. Proton dose calculation on scatter-corrected CBCT image: Feasibility study for adaptive proton therapy. *Med Phys*. 2015;42(8):4449-4459. doi: 10.1118/1.4923179 [doi].
78. Gang GJ, Zbijewski W, Webster Stayman J, Siewerdsen JH. Cascaded systems analysis of noise and detectability in dual-energy cone-beam CT. *Med Phys*. 2012;39(8):5145-5156. doi: 10.1118/1.4736420 [doi].
79. Schmidt TG. Optimal "image-based" weighting for energy-resolved CT. *Med Phys*. 2009;36(7):3018-3027. doi: 10.1118/1.3148535 [doi].
80. Roos PG. Multiple gain ranging readout method to extend the dynamic range of amorphous silicon flat panel imagers. *SPIE Proc Phys Med Imaging*. 2004;5368:139-149.

## Appendix A

In this section, we derive analytical expressions to theoretically demonstrate the effect of various parameters on DE weighting factors. These parameters include beam hardening, scatter, detector response, tube mAs, and detector gain. We will refer to **Figure A.1** depicting LE and HE beams incident on the patient and the detector.

### A.1. Monoenergetic Case

First, we assume monoenergetic HE and LE beams with no patient scatter and an ideal detector. Using Lambert-Beer law, for beam intensities  $I_{L0}$  and  $I_{H0}$  incident on the patient, the detector signals  $I_L$  and  $I_H$  after passing through the patient are:

$$I_H = I_{H0} e^{-\mu_H^t t - \mu_H^b b} \quad (\text{A.1})$$

$$I_L = I_{L0} e^{-\mu_L^t t - \mu_L^b b} \quad (\text{A.2})$$

where  $\mu_H^t$  and  $\mu_L^t$  are the linear attenuation coefficients for soft-tissue for high and low energies,  $\mu_H^b$  and  $\mu_L^b$  are the corresponding values for bone, and  $t$  and  $b$  are the soft-tissue and bone thicknesses respectively. A linear log subtraction is applied as per Eq.(2.1) to calculate the soft-tissue-only DE image.

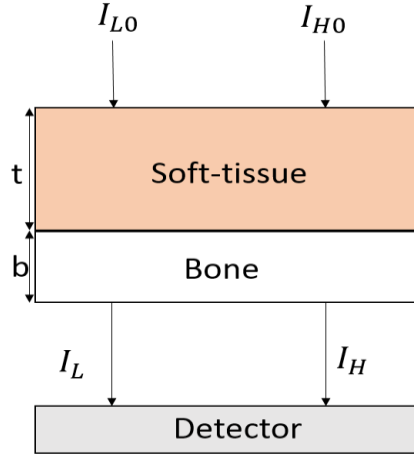


**Figure A.1:** LE and HE beams are detected after passing through soft-tissue and bone with thicknesses  $t$  and  $b$  respectively.

To find a weighting factor in the soft-tissue-only DE image that replaces the bone with soft-tissue with thickness  $b_0$ , the detected signal with and without bone thickness should be the same. Thus,

$$\ln(I_{DE}(t, b)) = \ln(I_{DE}(t + b_0, 0)) \quad (\text{A.3})$$

$$-\mu_H^t t - \mu_H^b b + \ln(I_{H0}) + \omega \mu_L^t t + \omega \mu_L^b b - \omega \ln(I_{L0}) = -\mu_H^t (t + b_0) + \ln(I_{H0}) + \omega \mu_L^t (t + b_0) - \omega \ln(I_{L0}) \quad (\text{A.4})$$

$$-\mu_H^b b + \mu_H^t b_0 = -\omega \mu_L^b b + \omega \mu_L^t b_0 \quad (\text{A.5})$$

$$\omega = \frac{\mu_H^b b - \mu_H^t b_0}{\mu_L^b b - \mu_L^t b_0} \quad (\text{A.6})$$

In the case where  $b_0=0$ , i.e. when bone is replaced with air, the  $\omega$  is reduced to:

$$\omega = \frac{\mu_H^b}{\mu_L^b} \quad (\text{A.7})$$

This is the weighting factor expression commonly referred to in the literature.<sup>10,26</sup> In the case where  $b_0 = b$ , i.e. when bone is replaced with soft-tissue with the same thickness, the  $\omega$  is:

$$\omega = \frac{\mu_H^b - \mu_H^t}{\mu_L^b - \mu_L^t} \quad (\text{A.8})$$

which has been reported in other literature.<sup>64,78</sup> Seeking a weighting factor by means of finding CNR close to zero as per **Figure 2.5a**, effectively applies Eq.(A.3) when  $b_0=0$ .<sup>33,60</sup>

## A.2. Beam Hardening Effects

Next, we include the effect of polyenergetic beams where beam hardening occurs in the patient. We still assume no scatter and an ideal detector. When the incident spectra pass through various soft-tissue and bone thicknesses, the harden spectra will contribute to the detected signal. Thus, Eq.(A.7) and (A.8) have to be modified to represent the effective attenuations:

$$\omega = \frac{\bar{\mu}_H^b}{\bar{\mu}_L^b} \quad (\text{for } b_0 = 0) \quad (\text{A.9})$$

$$\omega = \frac{\bar{\mu}_H^b - \bar{\mu}_H^t}{\bar{\mu}_L^b - \bar{\mu}_L^t} \quad (\text{for } b_0 = b) \quad (\text{A.10})$$

where  $\bar{\mu}$  is the spectrum weighted linear attenuation coefficients for either LE or HE detected beams, i.e.<sup>33,79</sup>

$$\bar{\mu} = \frac{\int \Phi(E)\mu(E)dE}{\int \Phi(E)dE} \quad (\text{A.11})$$

where  $\Phi(E)$  is the fluence spectrum after passing through soft-tissue and bone, and  $\mu(E)$  is the bone linear attenuation coefficient at a given energy.

### A.3. Scatter Effects

Patient scatter effects can be included by noting that both primary and scatter photons will be detected. In the presence of scatter, Eq.(A.1) and Eq.(A.2) can be modified as

$$I_H = I_{H0}[1 + s_H(t, b)]e^{-\bar{\mu}_H^t t - \bar{\mu}_H^b b} \quad (\text{A.12})$$

$$I_L = I_{L0}[1 + s_L(t, b)]e^{-\bar{\mu}_L^t t - \bar{\mu}_L^b b} \quad (\text{A.13})$$

where  $s_H(t, b)$  and  $s_L(t, b)$  are the scatter to primary ratios for high and low energies for a given patient geometry at a fixed location in the image with  $(t, b)$  thicknesses of soft-tissue and bone. By re-applying Eq.(A.3) one can simplify and solve for  $\omega$  to account for scatter:

$$\begin{aligned} & -\bar{\mu}_H^b b + \omega \bar{\mu}_L^b b + \ln(1 + s_H(t, b)) - \omega \ln(1 + s_L(t, b)) \\ & = \ln(1 + s_H(t + b_0, 0)) - \omega \ln(1 + s_L(t + b_0, 0)) - \bar{\mu}_H^t b_0 + \omega \bar{\mu}_L^t b_0 \end{aligned} \quad (\text{A.14})$$

$$\begin{aligned} & -\bar{\mu}_H^b b + \bar{\mu}_H^t b_0 + \ln(1 + s_H(t, b)) - \ln(1 + s_H(t + b_0, 0)) \\ & = -\omega \bar{\mu}_L^b b - \omega \ln(1 + s_L(t + b_0, 0)) + \omega \ln(1 + s_L(t, b)) + \omega \bar{\mu}_L^t b_0 \end{aligned} \quad (\text{A.15})$$

$$\omega = \frac{\bar{\mu}_H^b b + \ln\left(\frac{1 + s_H(t, 0)}{1 + s_H(t, b)}\right)}{\bar{\mu}_L^b b + \ln\left(\frac{1 + s_L(t, 0)}{1 + s_L(t, b)}\right)} \quad (\text{for } b_0 = 0) \quad (\text{A.16})$$

$$\omega = \frac{\bar{\mu}_H^b b - \bar{\mu}_H^t b + \ln\left(\frac{1+s_H(t+b,0)}{1+s_H(t,b)}\right)}{\bar{\mu}_L^b b - \bar{\mu}_L^t b + \ln\left(\frac{1+s_L(t+b,0)}{1+s_L(t,b)}\right)} \text{ (for } b_0 = b \text{)} \quad (\text{A.17})$$

In the absence of scatter the scatter to primary ratios are zero, thus this equation simplifies to Eq.(A.9) and Eq.(A.10) above. Note that scatter to primary ratio terms are in general patient specific and can potentially be obtained for a given patient geometry using e.g. Monte Carlo simulation.



#### A.4. Detector Effects

The effect of detector response on  $\omega$  can be modeled by noting that both detective quantum efficiency ( $\alpha$ ) and average absorbed energy per interaction ( $E(t, b)$ ) depend on energy.<sup>10,70</sup> Due to beam hardening in the patient at various soft-tissue and bone thicknesses ( $t, b$ ), both  $\alpha$  and  $E(t, b)$  will vary. Therefore, beam hardening in the patient has an indirect effect on  $\omega$  due to detector response. Rather than expressing  $\alpha$  and  $E(t, b)$  as a function of energy, they can be expressed as a function of  $(t, b)$  and thus the detected signals can be expressed as:

$$I_H \cong I_{H0} \alpha_H(t, b) E_H(t, b) e^{-\bar{\mu}_H^t t - \bar{\mu}_H^b b} \quad (\text{A.18})$$

$$I_L \cong I_{L0} \alpha_L(t, b) E_L(t, b) e^{-\bar{\mu}_L^t t - \bar{\mu}_L^b b} \quad (\text{A.19})$$

where  $\alpha_L(t, b)$  and  $E_L(t, b)$  are energy averaged detective quantum efficiency and absorbed energy per interaction at a fixed location in the image with  $(t, b)$  thicknesses of soft-tissue and bone for a low energy. Likewise,  $\alpha_H(t, b)$  and  $E_H(t, b)$  are detective quantum efficiency and absorbed energy per interaction at a fixed location in the image with  $(t, b)$  thicknesses of soft-tissue and bone for a high energy. These equations may then be simplified to solve for  $\omega$  in a similar manner as per Eq.(A.3)

$$-\bar{\mu}_H^b b + \omega \bar{\mu}_L^b b + \ln(\alpha_H(t, b) E_H(t, b)) - \omega \ln(\alpha_L(t, b) E_L(t, b)) = \ln(\alpha_H(t + b_0, 0) E_H(t + b_0, 0)) - \omega \ln(\alpha_L(t + b_0, 0) E_L(t + b_0, 0)) - \bar{\mu}_H^t b_0 + \omega \bar{\mu}_L^t b_0 \quad (\text{A.20})$$

$$-\bar{\mu}_H^b b + \bar{\mu}_H^t b_0 + \ln(\alpha_H(t, b) E_H(t, b)) - \ln(\alpha_H(t + b_0, 0) E_H(t + b_0, 0)) = -\omega \bar{\mu}_L^b b - \omega \ln(\alpha_L(t + b_0, 0) E_L(t + b_0, 0)) + \omega \ln(\alpha_L(t, b) E_L(t, b)) + \omega \bar{\mu}_L^t b_0 \quad (\text{A.21})$$

$$\omega = \frac{\bar{\mu}_H^b b + \ln\left(\frac{\alpha_H(t,0)E_H(t,0)}{\alpha_H(t,b)E_H(t,b)}\right)}{\bar{\mu}_L^b b + \ln\left(\frac{\alpha_L(t,0)E_L(t,0)}{\alpha_L(t,b)E_L(t,b)}\right)} \quad (\text{for } b_0 = 0) \quad (\text{A.22})$$

$$\omega = \frac{\bar{\mu}_H^b b - \bar{\mu}_H^t b + \ln\left(\frac{\alpha_H(t+b,0)E_H(t+b,0)}{\alpha_H(t,b)E_H(t,b)}\right)}{\bar{\mu}_L^b b - \bar{\mu}_L^t b + \ln\left(\frac{\alpha_L(t+b,0)E_L(t+b,0)}{\alpha_L(t,b)E_L(t,b)}\right)} \quad (\text{for } b_0 = b) \quad (\text{A.23})$$

In the case where the detector's response is the same for all bone and soft-tissue thicknesses, i.e.  $\alpha(t + b_0, 0) = \alpha(t, b)$  and  $E(t + b_0, 0) = E(t, b)$ , then these expressions reduce to Eq.(A.9) and Eq.(A.10).

## A.5. Tube mAs Effects

The effects of mAs can be realized by noting that a change in mAs will not change the spectra. Nonetheless, varying mAs will linearly scale  $I_{H0}$  and  $I_{L0}$  in Eq.(A.1) and Eq.(A.2) above. Both these terms cancel out when calculating  $\omega$  in Eq.(A.4).

However, the final DE image is then calculated as:

$$\ln(I_{DE}) = \ln(I_H) - \omega \ln(I_L) \quad (\text{A.24})$$

$$\ln(I_{DE}) = -(\mu_H^t - \omega \mu_L^t)t + \ln(I_{H0}) - \omega \ln(I_{L0}) \quad (\text{A.25})$$

By defining

$$\ln(I_{DE_0}) = \ln(I_{H0}) - \omega \ln(I_{L0}) \quad (\text{A.26})$$

the final DE image is

$$I_{DE} = I_{DE_0} e^{-(\mu_H^t - \omega \mu_L^t)t} \quad (\text{A.27})$$

which is only a function of soft-tissue thickness,  $t$ , as bone,  $b$ , has canceled. This equation implies that the final DE image pixel values will depend on mAs while  $\omega$  itself is independent of mAs.

## A.6. Effect of Detector Gain

To incorporate the effects of gain, Eq.(A.1) and Eq.(A.2) can be written as

$$I_H = I_{H0}g_H e^{-\mu_H^t t - \mu_H^b b} \quad (\text{A.28})$$

$$I_L = I_{L0}g_L e^{-\mu_L^t t - \mu_L^b b} \quad (\text{A.29})$$

where  $g_H$  and  $g_L$  are detector gain values for high and low energies respectively. When solving for  $\omega$  using Eq.(A.3) the result is

$$-\mu_H^t t - \mu_H^b b + \ln(I_{H0}) + \ln(g_H) + \omega\mu_L^t t + \omega\mu_L^b b - \omega \ln(I_{L0}) - \omega \ln(g_L) = -\mu_H^t(t + b_0) + \ln(I_{H0}) + \ln(g_H) + \omega\mu_L^t(t + b_0) - \omega \ln(I_{L0}) - \omega \ln(g_L) \quad (\text{A.30})$$

We assume gain values are constant across the image, i.e.  $g_H$  and  $g_L$  are not functions of  $(t, b)$  at a given location in the images. Thus, this simplifies to Eq.(A.4), making  $\omega$  independent of the detector gain. The final DE image will be:

$$I_{DE} = I_{DE_0}g_{DE} e^{-(\mu_H^t - \omega\mu_L^t)t} \quad (\text{A.31})$$

where

$$g_{DE} = \ln\left(\frac{g_H}{(g_L)\omega}\right) \quad (\text{A.32})$$

Similar to mAs case above, the final DE image pixel values depend on detector gain while  $\omega$  itself does not. Note that this applies only when detector gain does not vary across the image for a given acquisition technique. However, this may not be valid for some detectors, in which case  $\omega$  could depend on both detector gain and mAs value.<sup>60,80</sup>

## A.7. Combination of Effects

Finally, one can combine all above parameters affecting the weighting factor. The intensities of the high and low energy images are:

$$I_H \cong I_{H0} g_H \alpha_H(t, b) E_H(t, b) [1 + s_H(t, b)] e^{-\bar{\mu}_H^t t - \bar{\mu}_H^b b} \quad (\text{A.33})$$

$$I_L \cong I_{L0} g_L \alpha_L(t, b) E_L(t, b) [1 + s_L(t, b)] e^{-\bar{\mu}_L^t t - \bar{\mu}_L^b b} \quad (\text{A.34})$$

By applying Eq.(A.3), the final derivation for  $\omega$  can be obtained as:

$$\omega = \frac{\bar{\mu}_H^b b + \ln\left(\frac{\alpha_H(t,0) E_H(t,0) (1+s_H(t,0))}{\alpha_H(t,b) E_H(t,b) (1+s_H(t,b))}\right)}{\bar{\mu}_L^b b + \ln\left(\frac{\alpha_L(t,0) E_L(t,0) (1+s_L(t,0))}{\alpha_L(t,b) E_L(t,b) (1+s_L(t,b))}\right)} \quad (\text{for } b_0 = 0) \quad (\text{A.35})$$

$$\omega = \frac{\bar{\mu}_H^b b - \bar{\mu}_H^t b + \ln\left(\frac{\alpha_H(t+b,0) E_H(t+b,0) (1+s_H(t+b,0))}{\alpha_H(t,b) E_H(t,b) (1+s_H(t,b))}\right)}{\bar{\mu}_L^b b - \bar{\mu}_L^t b + \ln\left(\frac{\alpha_L(t+b,0) E_L(t+b,0) (1+s_L(t+b,0))}{\alpha_L(t,b) E_L(t,b) (1+s_L(t,b))}\right)} \quad (\text{for } b_0 = b) \quad (\text{A.36})$$

where all parameters are defined above and  $\bar{\mu}_H^b$  and  $\bar{\mu}_L^b$  are calculated as per Eq.(A.11).

The above derivations were for the weighting factor  $\omega$  that cancels the bone to obtain soft-tissue-only DE image. Similarly, the weighting factor  $\omega_b$  that cancels the soft-tissue to obtain bone-only DE image,

$$\ln(I_{DE_B}) = -\ln(I_{HE}) + \omega_b \ln(I_{LE}), \quad (\text{A.37})$$

can be derived using:

$$\ln(I_{DE}(t, b)) = \ln(I_{DE}(0, b)) \quad (\text{A.38})$$

This effectively removes the soft-tissue (by replacing it with air) in the final DE image.

This yields the final derivation for  $\omega_b$  as:

$$\omega_b = \frac{\bar{\mu}_H^t t + \ln\left(\frac{\alpha_H(0, b) E_H(0, b) (1 + s_H(0, b))}{\alpha_H(t, b) E_H(t, b) (1 + s_H(t, b))}\right)}{\bar{\mu}_L^t t + \ln\left(\frac{\alpha_L(0, b) E_L(0, b) (1 + s_L(0, b))}{\alpha_L(t, b) E_L(t, b) (1 + s_L(t, b))}\right)} \quad (\text{A.39})$$

$$\omega_b = \frac{\bar{\mu}_H^t}{\bar{\mu}_L^t} \quad (\text{for } t = 0) \quad (\text{A.40})$$